Characterization and Fundamental Investigation of Laser Doping for Silicon Solar Cells

Lujia Xu

October 2014

A thesis submitted for the degree of
Doctor of Philosophy of the Australian National University

Australian
National
University

To my beloved family —

Especially to my departed old brother who used his life to save other's life and to my departed grandfather who is always the best man in my heart.

献给我深爱的家人

Declaration

I certify that this thesis does not incorporate without acknowledgement any material previously submitted for a degree or diploma in any university, and that, to the best of my knowledge, it does not contain any material previously published or written by another person except where due reference is made in the text. The work in this thesis is my own, except for the contributions made by others as described in the Acknowledgements.

Lujia Xu

Acknowledgement

First and foremost, I would like to express my deepest gratitude to my supervisor, Assoc. Prof. Klaus Weber. Without his encouragement, guidance and support, it is impossible for me to finish this thesis. Not only the knowledge and experience have I learned from him but also the rigorous and accurate attitude of doping research. He has always been generous with his time in discussing problems with me that I meet in experiments. He allows me a large freedom to study the topics I am interested in and provides valuable suggestions for me to avoid unnecessary detour. He has also given me a lot of patience and help on my English speaking and writing. I must say I could not wish for a better supervisor and mentor than Assoc. Prof. Klaus Weber.

I would also like to thanks Dr Andreas Fell and Dr Evan Franklin for sharing their knowledge and experience on laser doping and solar cell. Without their guidance and help, I would not even be able to run the laser system properly let alone finishing any further experiment.

In addition, it is so lucky for me to have a versatile expert — Dr Andreas Fell — in both laser doping and solar cell simulation in our laser group. He always patiently answers my endless questions and friendly help me in experiment set-up and data analysis. Without his help and support, it is impossible for me to have current understanding about laser doping.

I would also like to thanks Prof. Andres Cuevas. From his courses, I have a much deeper comprehension of solar cell both macroscopically and microscopically. I am also grateful for Prof. Andrew Blakers for his support during my PhD study in my supervisor panel as well.

Furthermore, during my PhD study, I have been helped by many kind people. They are Mr. Di Yan, Dr. Pheng Phang, Dr. Ziv Hameiri, Mr. Wensheng Liang, Dr. Xinbo Yang, Dr. Daniel Walter, Mr. Teng Kho, Dr. Sachin Surve, Ms. Jun Yu, Mr. Da Wang, Dr.

Andrew Thomson, Dr. Hua Chen, Dr. Frank Brink, Ms. Erin Crisp, Assoc. Prof. Daniel Macdonald, Ms. Nina de Caritat, Mr. James Bullock, Mr. Peiting Zheng, Mr. Kelvin Sio, Mr. Chris Samundsett, Mr. Mark Saunders, Mr. Bruce Condon, Dr. Jason Chen, Ms. Anyao Liu, Dr. Siew Lim, Dr. Dongchul Suh, Mr. Tomas Ratcliff, Dr. Tom White, Dr. Fiacre Rougieux, Dr. Nicholas Grant, Dr. Ngwe-Soe Zin, Mr Xinyu Zhang, Mr. Chang Sun, Mr. Teck Kong Chong, Dr. Qunyu Bi, Mr. Chog Barugkin, Mr. Tom Allen, Mr. Wuyi Liang, Dr. Marco Ernst, Ms. Rowena Mankelow, Dr. Simeon Baker-Finch, Dr. Yimao Wan, Mr. Phillip Tweedie, Dr. Beatriz Velasco, Ms. Maureen Brauers, Dr. Alexander Laskin, Dr. Christoph Fleischmann, Ms. Lachlan Black, Mr. Young Han, Ms Jinjin Cong, Mr. Wie Joe, Ms. Kat Fischer. Thanks very much for their support in lab process, experimental plan discussion and data analysis.

Last but not least, I want to thanks my forever-beloved family — my great parents and grandparents for their endless and unconditional love, support and understanding; my young twin sister for always being my best listener and for looking after our family when I am studying oversea; my lovely wife for being by my side and bringing me so many new views about values, myself and life.

Abstract

Advanced structures with localized contacts can enable high efficiency crystalline silicon solar cells, but they are complex and costly to fabricate using conventional techniques. Hence, the development of new, cheaper processes to produce localized contact regions is of great interest. One of the most promising processes is laser doping. This thesis explores three main areas related to the challenges of laser doping, in particular the characterization of the laser-doped regions, the degradation of the silicon/dielectric interface in the vicinity of the laser-doped regions, and the degradation of the laser processed silicon.

A technique named secondary electron microscopy dopant contrast imaging (SEMDCI) is firstly introduced for the characterisation of the cross-section/top-surface of laser-doped samples. This technique can be used for a large range of different dopant sources and different laser doping methods. The technique can be employed to obtain quantitative dopant density images for p-type laser-doped regions, albeit currently over a limited range of dopant densities and with relatively large error. Using this technique, the risk of metallization shunts near the edges of dielectric film windows opened by the laser can be evaluated. Furthermore, this technique is useful for understanding the interaction between different materials during the laser doping process.

The impact of the SiN_x layer thickness in SiO_2/SiN_x stacks on the properties of laser-doped lines is investigated through measurement of the doping profile near the edge of the dielectric window which is an important factor in determining the likelihood of high recombination or even shunting from the subsequent metallization process. Fundamentally, a problem of exposed and undoped silicon near the dielectric window is identified for most of the investigated parameter range. However, optimization of the laser parameters and dielectric film conditions is shown to be capable of preventing or at least minimizing this problem. Beside this problem, the residual dielectrics close to the

edge might be degraded after laser process. Therefore, experimental methods are proposed to detect this possible degradation.

In the last part of the thesis, boron diffused samples capped with different dielectric films (including bare surfaces) are processed using laser pulses and characterized by photoluminescence imaging (PL) to study the degradation of the electronic properties of the processed regions. In this way, without the interference of a dopant precursor, the thermal and dielectric effects are separately investigated. It is found that the thermal effects do not lead to significant damage and additional recombination, provided no severe silicon evaporation occurs. However, when a dielectric film is present, a considerable increase in recombination is observed irrespective of laser parameters. The magnitude of the increase in recombination varies substantially depending on the dielectric used. It is demonstrated that both sufficient silicon melting and low recombination can in principle be achieved, particularly using long pulse durations and small pulse distances. In addition, N_2 annealing after laser process was proved to be an effective way to reduce the defects induced by both the thermal effects and dielectrics.

Contents

1 Introduction

1.1 Motivation

Global warming [1-3], the exhaustion of energy resources [4] and energy poverty [5] are three significant energy-related threats that human beings are facing today. These three problems are all mainly caused by the use of fossil fuels (coal, oil, and gas) as the primary energy resource.

To enable the sustainable development of human civilization, one of the biggest tasks for mankind is to strongly reduce and finally completely replace the use of fossil fuels by other clean energy resources. There are several alternatives to fossil fuels. Nuclear energy is often suggested as a non-greenhouse-gases-emitting large-scale source of electric power. However, nuclear energy has issues of waste disposal, security, the limited supply of uranium and the health concerns related to nuclear energy. Recently, it was shown that nuclear power generation is not as economical as other alternative solutions such as solar energy [6]. Renewable energy sources are the most promising candidates to provide clean energy and are able to replace fossil fuels in many applications. However, the application of most renewable energy techniques has its limitation. Wind and hydroelectric generation can only be used in suitable locations and cannot meet all the world's energy demand. Biomass that is generated by the burning of organic material is limited by the availability of water and arable land. Geothermal is limited by the high cost of drilling. Harnessing of the oceans' energy is also possible but the technologies required are immature [7]. Although it is more likely to solve the global energy problems by a combination of all the mentioned renewable energy alternatives instead of relying on only one, solar energy is the most effective one within all candidates.

The energy per hour received by the Earth's surface from the sun is much more than

humans use in a year and the potential of usable solar radiation on earth is much greater than world energy consumption [4]. As can be seen in Fig. 1, photovoltaic (PV) module/cell production has shown rapid growth rates since 2005. In 2012, PV production increased again but more modestly than previous years, increasing by around 10 % and reaching a worldwide production volume of about 38.5 GWp of photovoltaic modules. The compound annual growth rate (CAGR) over the last decade was about 55 %, which makes photovoltaics one of the fastest growing industries at present [8]. As long as the sunlight can reach, there is hardly any limitation on the location where solar energy can be used. PV modules, when properly designed and manufactured, are durable, easy to transport and nearly maintenance-free. Hence, PV is an ideal solution for rural and inaccessible regions. After the production of PV modules, the power generation process is totally pollutant-free. As the PV module can be installed at the point of use, it potentially prevents any associated environmental damage and can save the cost of developing a transmission network.

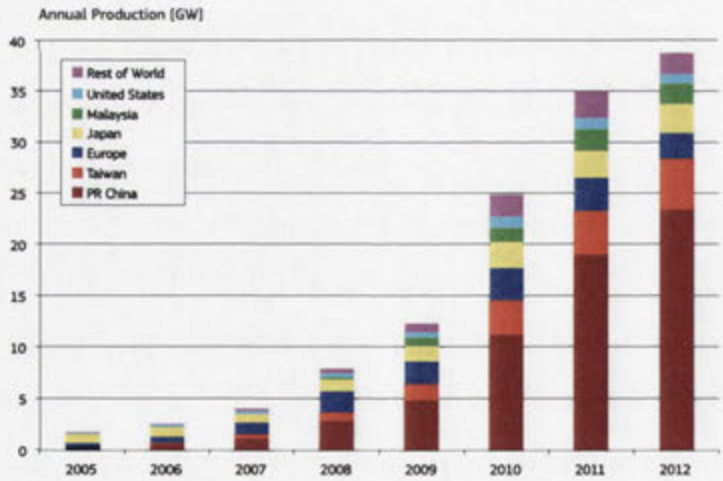

Fig. 1 World PV Cell/Module Production from 2005 to 2012. Adapted from reference [8].

One of the main factors limiting PV application is the solar cell cost. Cost reduction can be partially achieved by large scale manufacturing and temporally by political support, but the fundamental solution is to develop cost-saving manufacturing techniques and to improve the solar cell efficiency.

This thesis focuses on the field of crystalline silicon solar cells, which is currently the dominant PV technology. A large part of the cost for manufacturing crystalline silicon solar cells with advanced structures, for example PERC cells [9] and back-contact cells [10], comes from complex fabrication processes, including patterning processes. Hence, there is a need to develop cheaper patterning and local doping processes to allow the formation of localized contacts and emitter regions. One of the most promising processes is laser doping.

Laser doping offers an effective method to define heavily doped localized metal contact regions for solar cells [11-17]. Several variants of the technique exist. One attractive approach is to deposit a dopant precursor on top of a dielectric film (the surface passivation film or stack on the front or rear of the solar cell) and then use a laser to selectively melt the silicon surface, in the process removing the overlying dielectric and incorporating dopant from the precursor into the silicon. The precursor is subsequently removed. In this way, doping and contact opening occur in the same step. Despite its attractiveness, this process is challenging due in part to the listed reasons below:

- The shortcomings of current characterisation methods for laser-doped regions because of the small feature size of laser-processed regions;
- The degradation in the silicon/dielectric interface in the vicinity of laser-doped regions;
- The degradation in the electronic quality of the laser-processed silicon due to the thermal effects or the interaction between silicon and dielectric films.

This thesis explores these three problems in more detail.

1.2 Thesis outline

Chapter 2 will briefly introduce the history and status of laser doping research,

followed by the review of the mechanism of laser doping.

Chapter 3 reviews the most important characterization methods used in this thesis.

Chapter 4 is all about SEMDCI, including the introduction of its mechanism, parameters and applications.

Chapter 5 focuses on the edge of the laser-opened dielectrics window.

Chapter 6 will have a fundamental look at the laser-processed region to see how the thermal effect and the dielectrics influence the electronic quality of the silicon.

Chapter 7 summarises the most important results discussed in this thesis and propose suggestions for possible future works.

2 Laser doping Review

2.1 Why laser doping?

The first question that needs to be asked is why laser doping is of great interest for solar cell fabrication. A simple answer to this question is that laser doping enables the creation of highly-doped localized contacts for solar cells with low cost and simple fabrication steps. More specifically, laser doping can address the following:

The requirement of achieving a highly doped region for contacting

A low contact resistance (ohmic contact) is a basic requirement for high efficiency solar cells [18]. In an ideal case, by choosing a metal with a suitable work function, an ohmic contact can be formed even if the silicon is lowly doped due to the band bending near the surface [19]. However, in practice, because of Fermi level pinning [20], this is difficult to achieve. In practice, good contacts are often produced by forming a highly doped region at the silicon surface [19]. The heavy doping ensures that carriers can usually tunnel through any energy barrier since this barrier will be very narrow, resulting in an ohmic contact [18].

Thermal budget considerations

The highly doped regions can be fabricated traditionally through furnace diffusions. However, furnace diffusions have two limitations. Firstly, furnace diffusions result in high temperatures over the whole wafer including the bulk where no diffusion is required. This can decrease the bulk lifetime especially when commercial wafers such as Czochralski (Cz) or multi-crystalline (mc) silicon are used. Second, if a highly-doped and deep junction is the aim, for example the contact regions of selective emitters, long time furnace diffusions at high temperature will be required. This will result a high fabrication cost. In contrast, the localized nature of laser processes and the

short pulse times mean that the overall thermal budget on the wafer is lower and the application of high temperature is confined only to the required regions.

The cost of fabricating localized features

The greatest strength of the laser doping technique over the diffusion technique is the fact that it produces localized features.

Localized contacts are indispensable if front contacts are applied, so that light can enter the cell, but they can also be used at the back for achieving high efficiency. Localized contacts taking up a small fraction of the device area permit the passivation of most of the surface, improving both open circuit voltage (V_{oc}) and short circuit current (I_{sc}). Carrier crowding effects near the localized contacts can help to further reduce recombination due to the decrease of the mobility of *minority* carriers at both V_{oc} and at the maximum power point. The drawback of localized contacts is the increase of series resistance because of the current crowding of *majority* carriers near the contacts. By optimizing the pitch distance and controlling the recombination at bulk and surface, the gain of using localized contacts will surpass its loss [21-23]. This is the reason why most high efficiency silicon solar cell structures use localized contacts instead of full area contacts.

Traditionally in semiconductor fabrication, localized features can be very accurately fabricated by photolithography. However, the high cost of photolithographic processes is a limitation for its commercial application to solar cells. Laser doping is one of the most promising methods for defining localized contacts with lower cost and high throughput.

Other possibilities exist to produce high V_{oc} and efficiency without the need for localized contacts, for example heterojunction [24] or passivated contact [25,26] solar cells. In these two types of cells, an ultra-thin passivation layer is grown underneath and on top of the *carrier selective collector* [27] respectively to significantly reduce the contact recombination so that the passivated non-contact region is no longer necessary

and a full area contact can be simply used. Although these two structures have a theoretically higher efficiency and simpler production steps compared to localized contact silicon solar cell, in practice it is still difficult to produce these structures reliably with good passivation. Only a few institutions and companies, for example Panasonic [28] and Sanyo [29], have so far demonstrated the production of such cells with good results.

Besides the localized feature, another main advantage of laser doping for commercial application is the fact that no (expensive) cleaning process is needed in order to form the selective emitter. This is different from other selective emitter methods that usually require two furnace diffusions.

2.2 Laser doping history

The formation of a p-n junction using laser techniques dates back to 1968 in IBM, when Fairfield and Schwuttke scanned a polished phosphorus-coated surface with a pulsed laser [30]. Bell Labs followed this work in 1970, by using a Nd:YAG laser to alloy aluminium into n-type silicon to form a p-n junction [31]. Since these two early works, especially in the first 4 years of the 1980s, researchers over the world, including Deutsch *et al* [12,32] , Stuck *et al* [13], Turner *et al* [14], Ibbs *et al* [15,16], Fogarassy *et al* [33] and Young *et al* [34], reported different techniques to form laser-doped junctions. Different dopant sources in gas [12,32], liquid [13] or solid [34] forms were successfully employed to produce doping using a laser. Laser-doped solar cells have been fabricated and have been sold by commercial companies, such as BP solar [35], SUNTECH [36], and RENA [37].

2.3 Laser doping classification

From these early and later studies, according to the phase of silicon (melted or solid), Abbott [38] classified laser doping process as solid-phase diffusion or liquid-phase

diffusion processes. The solid-phase diffusion process, which is similar to the process used in furnace diffusions [39], is designed to form extremely shallow junctions (<0.1 μm) hence is not of interest to solar cell fabrication. In contrast, the liquid-phase diffusion process shows great potential for application in solar cell. In this process, the silicon surface is firstly melted by the laser so that the dopant atoms enter the silicon in the liquid phase. The silicon melt then cools and recrystallises through a process of epitaxial growth, resulting in a heavily doped region throughout some or the entire melt area. The creation of relatively deep, heavily doped regions, despite melt duration in the order of microseconds, is possible because of the fact that the diffusion coefficient of dopant atoms in the liquid phase is orders of magnitude higher than in the solid phase [12-14,32,34].

2.4 Laser doping mechanism

The basis of the laser doping of silicon is the melting, recrystallization and solidification of silicon caused by laser irradiation, and the incorporation of dopant impurities during the period that the silicon is in the liquid phase.

2.4.1 Laser induced silicon material changes

Studies in the late 1970s and 1980s established the theoretical and experimental understanding of the melting and recrystallization of materials by laser radiation. A brief summary will be given below. More details can be found in references [40-48].

Melting and evaporation

Laser radiation can be regarded as a beam of photons. Photons with energy higher than the silicon band gap can be absorbed by silicon and excites electrons within the crystalline lattice. Because of the interaction between excited electrons and the lattice, the temperature of the irradiated region rises rapidly. When the laser pulse energy is sufficient, the temperature reaches the silicon melting point (1414 ^{o}C [49]). The

enthalpy increases with heating until the melting point is reached and the silicon phase changes from solid to liquid. Following the phase change, the temperature continues to rise. However, because of the larger surface reflectance (70 % [50] to 37 % [51] at 532 nm laser wavelength), larger absorption coefficient (1.19×10^{6} cm^{-1} [49] to 6550 cm^{-1} [49] at 532 nm, therefore only ~0.01 μm absorption depth), and higher thermal conductivity (1.56 $W\cdot cm^{-1}\cdot K^{-1}$ [49] to 1.10 $W\cdot cm^{-1}\cdot K^{-1}$ [52]) of liquid silicon than solid silicon, the rate of temperature increase rate is slower. Also, because the absorption depth is only ~0.01 μm (532 nm wavelength) [49] in liquid silicon, the deeper regions of the silicon in this case are heated by thermal conduction from the surface to the bulk rather than by absorbing radiation directly. The temperature remains constant once it reaches the boiling point (3267 °C [49]) and silicon starts to evaporate. Figure 2 summaries the states change of silicon.

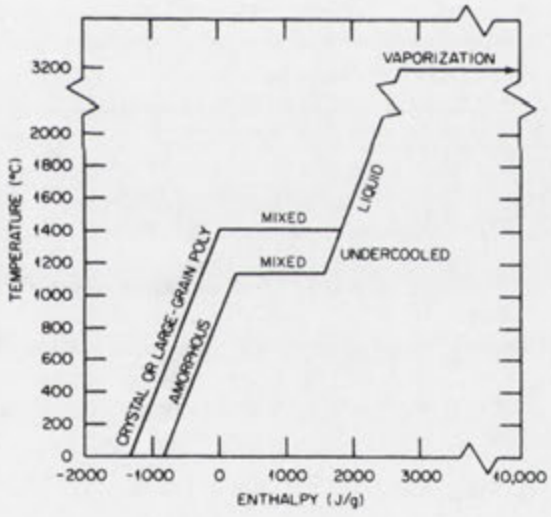

Fig. 2 State changes of silicon during laser irradiation. The zero of enthalpy is taken at the melting point of crystalline silicon. Adapted from [42].

Solidification and recrystallization

The thermal energy generated during laser radiation can be lost through the thermal conduction either to the bulk or to the environment. Once the laser pulse intensity decreases sufficiently, the energy loss exceeds the gain. The temperature starts to

decrease until the freezing point is reached. The melted silicon solidifies as the latent heat diminishes. The liquid-solid interface of silicon (termed the melt front) sweeps back and the silicon epitaxially recrystallises [40].

Melt duration and melt depth

For pulsed laser irradiation (which will be considered in this thesis), the melt duration can be defined as the time for which any silicon is molten following a laser pulse. The melt depth is the maximum depth of the molten silicon at any time. If no evaporation takes place, a higher laser pulse energy increases the melt duration and melt depth. Because the lowest pulse energy at which the silicon starts to evaporate increases with pulse duration, a longer pulse duration enables a higher pulse energy without causing evaporation, therefore allowing larger melt depth to be attained [53,54]. The melt depth is also strongly influenced by the laser wavelength, as the wavelength determines the absorption depth of laser energy. Longer wavelengths penetrate further into the silicon enabling deeper melts than short wavelengths.

Laser induced crystalline defects

The quality of the epitaxially recrystallised silicon layer is of great interest. Defects in this layer may cause degradation of electrical properties of the material and limit the application of laser doping for solar cells. Previous researchers have widely investigated this topic, but reached somewhat contradictory conclusions:

Narayan *et al.* [55] and Young *et al.* [56,57] concluded that a defect-free epitaxial layer can grow on a (100) silicon substrate as a result of laser induced melting, with the same crystalline orientation as the bulk. Defects, in the form of clusters, dislocations or stacking faults, were not observed in transmission electron microscopy (TEM) images. Different types of lasers were reported to be able to achieve the defect-free recrystallised zones [58,59].

On the other hand, using deep level transient spectroscopy (DLTS), Mooney *et al.* [60]

reported defects with a high concentration near the surface and extending up to 10μm into the bulk caused by three laser pulses irradiation using a 694 nm laser with ~40 ns pulse duration. Young *et al.*, despite reaching a conclusion of defect-free epitaxial growth on a (100) substrate, found a high density of stacking faults on a (111) substrate [61]. Using TEM, Hopman *et al.* [62] observed dislocations near the laser processed surface that was initially coated with a 105 nm thermal oxide, but only when a high laser power was used. Hameiri *et al.* [63,64] found no evidence of crystalline defects from electron beam induced current (EBIC) and electron backscattering diffraction (EBSD) observations, but did observe near-surface defects in TEM images and after Yang etching, especially for samples coated with dielectric films. The thermal expansion coefficient mismatch between silicon and dielectric films was recognized as the main mechanism of the formation of near-surface defects [63].

Degradation of electrical properties

Although laser-induced crystalline defects were not observed by all the researchers using TEM as discussed above, most noticed a degradation of the electrical properties of laser-melted regions, including recombination current pre-factor (J_{0e}), open circuit voltage (V_{oc}), internal quantum efficiency (IQE) (at short wavelengths), and implied V_{oc} [34,62,63,65]. The dominant mechanism for the observed electrical degradation can be different depending on whether a dielectric film was present during laser irradiation or not. For the case that dielectric films are used, the formation of near-surface defects is probably due to the thermal expansion coefficient mismatch between the dielectric(s) and silicon [63], whereas in the case of bare silicon surfaces, electrically-active point defects mainly related to a high recrystallization velocity [63,66,67] and contamination induced during laser processing (from the environment or the dopant source) [63,68,69] are more likely to dominate the degradation.

Parker *et al.* [70,71] reported that the observable electrical degradation occurs when using laser powers below the power at which a surface change becomes visible. They

assumed the power threshold for silicon melting and visible surface changes are the same for green laser. As discussed in Chapter 6, it was found that the silicon is degraded when there is visible surface changes, but the damage threshold is close to (slightly over) the evaporation threshold of silicon rather than the melting threshold.

2.4.2 Laser induced doping

When laser induced silicon melting happens in the presence of dopant sources, doping can occur via diffusion in the liquid phase of silicon. The doped silicon is created during the silicon epitaxial growth through the rearrangement of dopant and silicon atoms in the lattice. During recrystallization, dopant atoms that move from interstitial to substitutional lattice sites become electrically activated [34,72]. When proper laser parameters and dopant sources are used, complete electrical activation of the dopants atoms is achievable [13]. Compared to conventional furnace diffusion, laser induced diffusion has three main characteristics:

High diffusion coefficient

In the liquid phase, the diffusion coefficient is in the order of 1×10^{-4} cm^2/s , orders of magnitude higher than in the solid phase ($\sim1\times10^{-10}$ cm^2/s) and it is independent of the melt temperature [73]. In theory, both liquid and solid diffusion happen simultaneously, but because of the significant difference in diffusion coefficient, solid diffusion can be neglected [40].

High solubility

The maximum dopant concentration in solid silicon is limited by the solid solubility of the dopant atoms [74]. It was found that the concentration of dopant atoms in silicon following laser melting and recrystallization can show values much higher than the solid solubility limit [34,75]. This enhancement is explained by the fast solidification process. Because the melt front moves rapidly towards the surface, the excess dopants have no time to diffuse into the liquid to build up the equilibrium concentration in the

solid, resulting a higher concentration in the solid [75].

High segregation coefficient

Similar to the solubility limit, due to the fast solidification rate, the segregation coefficient of dopant atoms in the laser doping process is higher (approaching unity) than the value observed at near equilibrium conditions [46,76]. The direct influence of a higher segregation coefficient is a smoother dopant profile over depth. In contrast, a low segregation coefficient will result in an accumulation of dopant atoms at the surface due to the fact that dopants prefer to segregate from the resolidified regions towards the melt but are eventually confined within the material [74].

The values of the above three parameters for the mostly used boron and phosphorus dopants are listed in the Table 1.

Table 1 Diffusion coefficient in liquid, the maximum solubility, and segregation coefficient of phosphorous and boron in silicon under equilibrium conditions [64].

	Diffusion coefficient (in liquid) [cm^2/s]	**Ref.**	**Maximum solubility* [cm^{-3}]**	**Ref.**	**Segregation coefficient***	**Ref.**
Phosphorus	$(2.3\pm1.3)\times10^{-4}$	[77]	1.3×10^{21}	[49]	0.35	[78]
Boron	$(1.2\pm0.4)\times10^{-4}$	[77]	6×10^{20}	[49]	0.8	[78]

*Equilibrium conditions

Doping depth vs melt depth

The doping depth can be either shallower than or approximately same as the maximum melt depth, depending on the laser energy and the number of melting cycles. For a single pulse, in most cases, the melt front velocity is higher than the dopant diffusion velocity, so the maximum melt depth is greater than the doping depth. Only at low pulse energies, when the melt front slows down, are the two depths roughly same [79]. In the case of multiple laser pulses in the same location, the increasing number of melt cycles enable the dopant to diffuse deeper while the melt depth remains roughly

constant, as the silicon typically recrystallises and returns to near room temperature between one pulse and the next (for a pulse frequency in the kHz range and a pulse duration in the order to 10s of ns). Therefore, multiple melting cycles allow a smaller difference between the two depths [80].

2.5 Main laser doping techniques

There are several different laser doping techniques. These briefly reviewed as below.

2.5.1 Self-aligning method

This method has been developed at UNSW for creating selective emitter structures [81] and is also the main laser doping technique used in this thesis. In this method, the dopant precursor, for example a spin-on-dopant, is applied onto the dielectric film. The laser energy is used to selectively remove the dielectric film, and simultaneously melt the silicon underneath it while incorporating dopants into the melted region, creating a heavily doped layer. In this process, the dielectric film can be employed not only as an anti-reflection coating (ARC) and surface passivation layer, but also as a mask for the subsequent metallization. This technique enables the creation of a selective emitter and the opening of the dielectric for contacting within one step.

2.5.2 Laser chemical processing (LCP)

Willeke and Kray proposed this method in 2001 [82], which was initially referred to as laser chemical etching (LCE) [83]. Based on the laser light-guiding water jet theory [84], the laser beam is focused in a hair-thin dopant-rich chemical solution jet, which can be generated by emitting pressurised chemical solution through a small nozzle. This chemical jet directs the laser beam to the sample through total reflection at the water-air interface. While the laser beam melts the sample, the dopant in the chemical jet can be incorporated simultaneously. Figure 3 is a schematic of a LCP system.

Compared to dry laser doping techniques, there is no extra step required to apply dopant sources onto the sample surface in this wet laser doping technique. However, due to the complex laser beam reflection path within the chemical solution jet, the laser beam reaching the sample normally consists of multiple freckles rather than a single focused spot like in dry laser doping techniques, which may result in discontinuous laser doped regions.

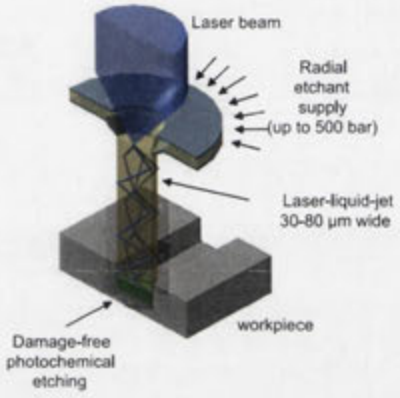

Fig. 3 The schematic of an LCP system. Adapted from [85].

2.5.3 Line-beam system

The line-beam system was developed and patented by the University of Stuttgart [86]. The laser beam shape used in this technique is highly elliptical with one short axis (<10 μm) and a long axis (~200 μm) [87]. The intensity distribution along both axes is Gaussian [59]. Because of the long focal line, this technique is more efficient at producing not only localized emitters but also large-area emitters.

2.5.4 Laser transfer doping

Laser transfer doping (LTD) is based on the method invented by Mei *et al.* [88,89] and was further developed and applied to solar cells by Ferré [90]. Figure 4 is the schematic of the LTD process. In this technique, the dopant precursor, instead of being applied on top of the wafer, is deposited on a glass substrate. The laser pulse is used to

ablate this dopant precursor from the glass, transfer the dopant to the wafer, and open the dielectric film simultaneously. In this way, the step of removing the dopant precursor after laser processing can be avoided, potentially simplifying the production process and widening the choice of dielectric films.

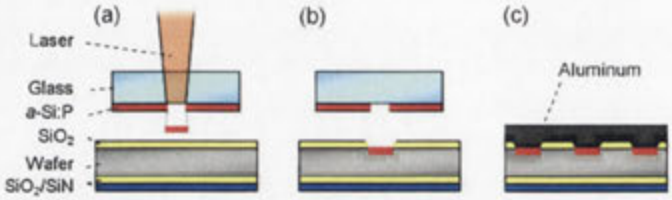

Fig. 4 Schematic illustration of the LTD process. Adapted from [90].

2.5.5 PassDop

The PassDop technique is firstly proposed by Suwito *et al.* from Fraunhoer ISE [91]. A dopant-rich passivation layer/stack is utilized in this technique, which services as both the dopant source and passivation film. The laser doping process opens the local contact and achieves highly doped regions simultaneously, followed by metallization without any further photolithography assistance or a step to remove residual dopant precursor. Both boron (Al_2O_3/a-SiC_x:B) and phosphorous (a-SiC:P and a-SiN_x:P) PassDop layer/stack have been developed to produce the local back side field (BSF) of the passivated emitter with rear locally diffused (PERL) solar cells. Interestingly, a-SiN_x:P was found to be compatible with firing therefore suitable for industrial screen print process [91-94]. A diagram of the PassDop process is shown in Fig. 5.

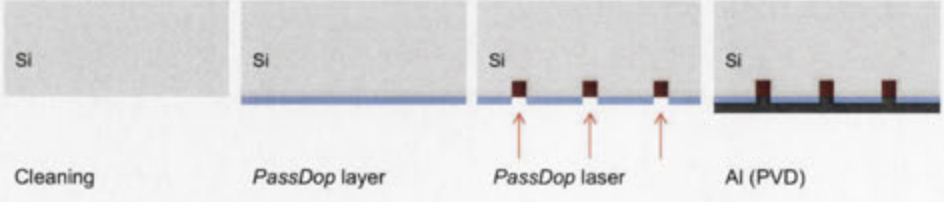

Fig. 5 Sequence of PassDop process. Adapt from [93]

2.6 Metallization for laser doping

The front side metal contacts in conventional silicon solar cells are fabricated by Ag screen printing, due to its high reliability and high throughput ability. Although, this technique is compatible with contacts generated by laser doping [95], it is limited by a few facts, including the requirement of alignment, the relatively large printing width, high contact resistance on lowly doped surfaces, and the increasing cost of Ag [96]. Therefore, new metallization methods, such as electroless plating [38,64,97] or photo-plating [98-100], have been proposed and investigated to overcome the limitations of screen printing.

Compared to screen printed contacts, electroless plated or photo-plated Ni-Ag or Ni-Cu contacts have less shading because of narrower metal fingers. They also offer better contact resistance on lightly doped surfaces due to the existence of a Ni seed layer [101]. These features enable a smaller finger pitch on lightly doped emitters to balance the trade-off between series resistance, recombination and optical losses [101]. In addition, electroless plating or photo-plating can make use of the self-aligned feature of contacts generated by laser doping techniques, given the passivation layers are formed before the laser process [64]. One of the biggest challenges in both the electroless and photo-plating techniques is the adhesion between the metal fingers and the silicon [64,101]. A Ni sintering step, which forms a Ni silicide, was found to be able to significantly improve the metal contact adhesion [102-104], although the sintering process may introduce the risk of silicide or metal spiking [105]. In order to reduce this risk, a deep laser doping profile was suggested [101] and the sintering temperature needs to be properly chosen [106,107]. Beside the function of increasing the metal contact adhesion, the Ni silicide also plays the role of reducing the contact resistance at the silicon-metal interface and preventing the diffusion of Ag or Cu into the junction region [64].

2.7 Laser doped solar cell results

Several research groups have reported good solar cell results by utilizing laser doping in the fabrication process. Some illustrative results are listed below.

- Kray *et al.* [108] reported 20.4 % efficient oxide-passivated local-fired contact (LFC) solar cells using LCP to fabricate the highly doped front selective emitter. The LCP step was after diffusion but before oxide passivation, so photolithography was still required for contact opening. (250 μm thick, 0.5 Ω·cm p-type float-zone (FZ) wafer, unknown area, 664.9 mV V_{oc}, 38.7 mA/cm^2 short current density (J_{sc}), and 79.2 % fill factor (FF));
- Dahlinger *et al.* [109] achieved 22 % efficient IBC cells using a line-beam system to produce large-area emitters, and BSFs at the rear side of the wafer. The passivation and contact opening followed the laser doping process, hence the photolithography was used. (275 μm thick, 2 Ω·cm n-type FZ wafer, 2×2 cm^2, 669 mV V_{oc}, 41.3 mA/cm^2 J_{sc}, and 79.8 % FF);
- Suwito *et al.* [91] reported a PERL cell using a-$Si_{1-x}C_x$:P as the PassDop layer to produce laser-doped BSF achieves an efficiency of 22.4 % (230 μm thick, 1 Ω·cm n-type FZ wafer, 4 cm^2, 701 mV V_{oc}, 39.8 mA/cm^2 J_{sc}, and 80.1 % FF). A recent result from Benick *et al.* refreshed this PassDop cell efficiency to 23.2 % using a Cz wafer (unknown thickness, 1.7 Ω·cm n-type Cz wafer, 4 cm^2, 669 mV V_{oc}, 41.3 mA/cm^2 J_{sc}, and 80.5 % FF) [92];
- Franklin *et al.* [110] recently explored all-laser doped IBC cells using a UV laser achieving a preliminary result of 19.1 % efficiency. Instead of using large-area laser-doped emitters and BSFs as Dahlinger *et al.* [109] did, localized laser-doped emitters and BSFs were produced. Following laser doping and passivation, contacts were opened by accurately aligned laser ablation rather than photolithography. (250 μm thick, 100 Ω·cm p-type FZ wafer, 4 cm^2, 671 mV V_{oc}, 41.7 mA/cm^2 J_{sc}, and 68 % FF).

- Hallam *et al.* [111] reported a record efficiency of 19.3 % for a large-area p-type Cz solar cell using standard full rear side aluminium contact. The front selective emitters of this cell were produced by a laser with 532 nm wavelength and 2 μm pulse duration using the self-aligning method. (~200 μm thick, 156.9 cm^2, 2 Ω·cm p-type commercial grade Cz wafer, 638 mV V_{oc}, 38.4 mA/cm^2 J_{sc}, and 78.82 % FF). Extending the self-aligning method to produce both front selective emitters and rear heavily doped local contacts, Wang *et al.* [36] achieved 20.3 % efficiency for a large-area p-type Cz solar cell using mass-manufacturing processes and equipment. (~180 μm thick, 155 cm^2, 1-3 Ω·cm p-type commercial grade Cz wafer, 665 mV V_{oc}, 40.9 mA/cm^2 J_{sc}, and 74.4 % FF).

The above cell results are summarized in Table 2.

Table 2 Summary of laser-doped solar cell results using different techniques.

Technique	Resistivity [Ω·cm]	Bulk	Thickness [μm]	Area [cm^2]	J_{sc} [mA/cm^2]	V_{oc} [mV]	FF [%]	Efficiency [%]	Contact opening	Ref.
LCP	0.5	p FZ	250	NA	38.7	664.9	79.2	20.4	Photolithography	[108]
Line-beam	2	n FZ	275	2×2	41.3	669	79.8	22	Photolithography	[109]
PassDop	1	n FZ	230	4	39.8	701	80.1	22.4	Simultaneously	[91]
PassDop	1.7	n Cz	NA	4	41.3	669	80.5	23.2	Simultaneously	[92]
General	100	p FZ	250	NA	41.7	671	68	19.1	Laser ablation	[110]
Self-aligning	2	p Cz	200	156.9	38.4	638	78.82	19.3	Simultaneously	[111]
Self-aligning	1-3	p Cz	180	155	40.9	665	74.4	20.3	Simultaneously	[36]

2.8 Challenges

As can be seen from the laser-doped cell results listed in Section 2.6, the laser doping procedure employed in practice can be classified into two strategies — *one-step* strategy and *two-step* strategy. In one-step strategy, the laser doping and contact opening are carried out simultaneously, while two-step strategy necessitates the alignment of the contact opening with the laser-doped region increasing the process complexity. Despite the attractiveness of one-step strategy, it is challenging due in part to the listed reasons below:

- The shortcomings of current characterisation methods for laser-doped regions because of the small feature size of laser-processed regions;
- The degradation in the silicon/dielectric interface in the vicinity of laser-doped regions;
- The degradation in the electronic quality of the laser-processed silicon due to the thermal effects or the interaction between silicon and dielectric films.

This thesis explores these three problems in more detail.

2.9 Laser doping system in ANU

2.9.1 Laser system

Currently there are four laser systems available in ANU.

(1) **Diode-Pumped Solid State (DPSS)** laser from Coherent Inc.: This is a frequency doubled Q-switched Nd:YVO_4 laser with 532 nm wavelength, Gaussian beam profile, 20-40 ns pulse duration, adjustable working frequency up to100 kHz.

(2) **Excimer** gas laser from Coherent Inc.: This is a 248 nm UV laser with ~30 ns pulse duration. This laser can provide a homogenous rectangular spatial beam

profile.

(3) **Laser chemical processing (LCP)** system from Synoval Inc. (product name Laser MicroJet®): This system use a 532 nm Q-switched fibre laser with pulse duration ~70 ns.

(4) **PyroFlex™** 25 laser system from Electro Scientific Industries Inc.: This is a 1064 nm wavelength pulsed fibre laser utilizing fibre-coupled laser diode pumping technology, providing programmable pulse durations from 2 to 600 ns. Most importantly, this laser system enables arbitrary pulse shapes with resolution of one ns. In ANU, this laser is externally frequency doubled to 532 nm.

2.9.2 Laser processing system setup

The diagram of a commonly used laser processing system setup is shown in Fig. 6. In this system, the laser beam emits from a laser head and reaches a scanning mirror that is controlled by a computer. If necessary, other optical components can be employed along the beam path. The scanning mirror directs the laser beam to the intended position on the sample surface through a f-theta lens. The f-theta lens focus the laser beam and allows the scanning mirrors to run at a constant angular velocity, since the angular velocities of input beam and output beam of the f-theta lens are directly proportional. The laser stage can be accurately controlled to move along both x and y axis with wanted velocity.

In this system, 1) either through controlling the scanning mirror while remaining the stage position; 2) or moving the stage while staying the scanning mirror; 3) or the combination of 1) and 2), most designed patterns can be applied onto samples.

For some laser systems, like LCP and Excimer, there is no scanning mirror or f-theta lens, so designed patterns can only be realized thorough the movement of the stage.

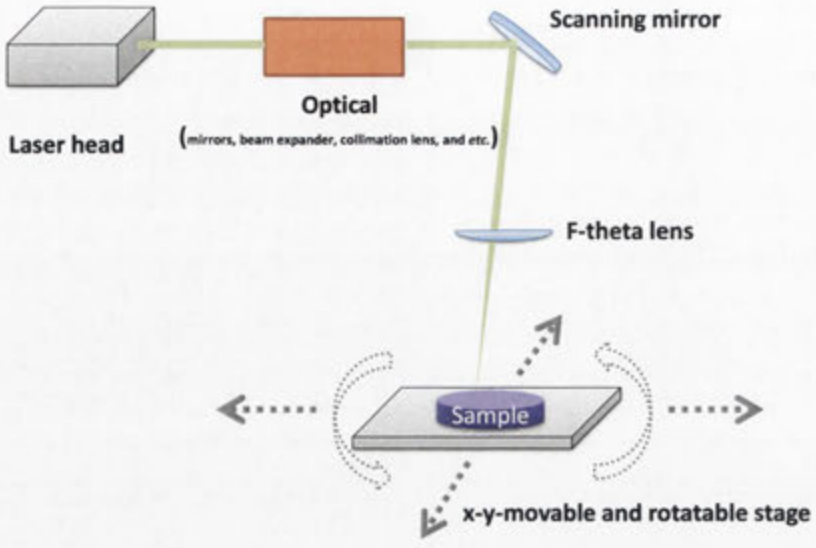

Fig. 6 Diagram of a general laser processing system setup.

2.9.3 Laser process parameters

A set of process related parameters — laser frequency, pulse energy (laser power), pulse distance (scan speed), and overlap time (scan time) — are used to describe a laser process for a given laser system.

Laser frequency (f) in units of Hz describes the laser pulse emission rate or the time interval between one pulse and the next ($1/f$ in units of s). The frequency in most laser systems is adjustable. Moderately frequency (tens of kHz) is normally used in this thesis to ensure the processing efficiency, while to avoid the instability of laser system at high frequency. In this case, the time interval between one pulse and the next is in the order of hundreds of ns.

Pulse duration (τ_p) in units of s is the duration of the optical pulses (also called pulse width or pulse length). The most frequently used method to define the pulse duration is the full width at half-maximum (FWHM) of the optical power versus time [112]. The pulse durations used in this thesis vary from tens to hundreds of ns.

Pulse energy (E_p) in units of J is the energy delivered by one laser pulse. **Laser power**

(P) in units of W is the total energy delivered by a number of laser pulses within one second at a given frequency. Laser power can be measured by power meter and is equivalent to pulse energy at a given frequency:

$$E_p = \frac{P}{f} . \tag{2-1}$$

Pulse distance (d_p) in units of m is the distance between the centres of one pulse and the next when scanning the laser across the sample surface at a constant speed. **Scan speed** (S_s) in units of m/s is equivalent to pulse distance at a given frequency:

$$d_p = S_s \times f . \tag{2-2}$$

Overlap time or scan time is used to describe how many pulses reach the same place of a sample, determining the number of melting cycles. Overlap time is mostly used for describing dot process, while scan time is used for line process.

3 Review of characterization methods

3.1 Secondary electron microscopy (SEM)

Secondary electron microscopy dopant contrast imaging (SEMDCI) based on secondary electron microscopy (SEM) is one of the main topics of this thesis. Before the detailed investigation of SEMDCI in Chapter 4, a brief background-review of SEM itself is given here.

3.1.1 What is SEM?

The scanning electron microscope (SEM) is a tool using a focused beam of electrons to characterise levels of detail and complexity inaccessible by light microscopy. SEM permits the observation and characterization of materials on a nanometer (nm) to micrometer (μm) scale [113].

In the SEM, a finely focused electron beam irradiates the area to be examined or the micro-volume to be analysed. The focused beam may sweep across the surface of the specimen to form images or may statically obtain an analysis at only one position. After the interaction of electron beam with the specimen, various forms of radiation are detected. The detected signals can be converted into images or can be used to analyse specimen's composition [113].

3.1.2 Electron-specimen interaction

The interaction of a focused electron beam with the specimen is the basis of SEM. There are many types of signals produced from the interaction of the electron beam with the specimen, including secondary electrons (SE), backscattered electrons (BSE), characteristic x-rays, and *etc*.. As the different types of signals are obtained from different emission volumes within the specimen, they carry information about different

characteristics of the specimen, for example surface topography, crystallography, and composition [113].

A simple physical level description will be helpful for the understanding the generation of those signal. When the beam electrons reach the specimen, as negatively charged particles, they interact with both the positively charged protons (atom centre) and the negatively charged atom orbital electrons (atom shell) of the specimen atoms. The incoming beam electrons are therefore scattered rather than penetrating the specimen. There are two types of scattering happened simultaneously— elastic and inelastic. In the elastic scattering, the beam electrons interact with protons and change their trajectory, their kinetic energy and velocity remaining essentially constant. After a number of elastic scattering events, the incident beam electrons will actually leave the specimen. Thus, elastic scattering results in backscattered electrons (BSE). Alternatively, in inelastic scattering, the incident beam electrons propagate through many atom layers with only a slight perturbation of the trajectory but with large energy loss via the interaction with the atom orbital electrons. This generates secondary electrons (useful for imaging), Auger electrons and X-rays [113].

The volume where the beam electrons interact with the specimen atoms can be observed by electron bombardment of polymethylmethacrylate (PMMA) [114] or through the technique of Monte Carlo electron trajectory simulation [115]. Figure 7 provides a summary of the electron-specimen interactions, illustrating the pear-shaped cross-section interaction volume.

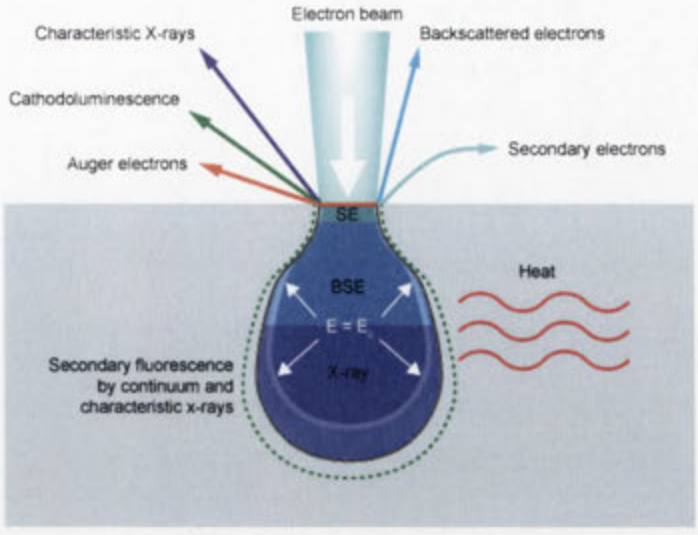

Fig. 7 Illustration of the electron-specimen interaction. Adapt from http://www.ammrf.org.au.

3.1.3 Secondary Electrons (SE)

Secondary electrons (SEs) play the dominant role in SEMDCI. SEs originate from electrons that are loosely bound in the outer shell of the specimen's atoms. After receiving sufficient kinetic energy from inelastic scattering of incident beam electrons, these electrons are freed from the host atom and will propagate through the solid. Some of these electrons will escape through the sample surface. Secondary electrons are defined as the electrons emitted from the specimen with an energy less than 50 eV [113].

Secondary electrons can be classified into two classes according to their generation processes [113]:

- SE1: The SEs generated by the incident beam electrons within 5λ of the surface, where λ is the mean free path for secondary electrons. λ is about 1 nm for metals and up to 10 nm for insulators [116]. SE1 electrons offer a high-resolution signal.
- SE2: During the process that BSEs exit from materials, they have a chance to cause inelastic scattering to generate SEs. The SEs generated by the exiting

BSEs within 5λ of the surface is defined as SE2. The SE2 signal changes with the BSE signal, therefore inherently a low resolution signal.

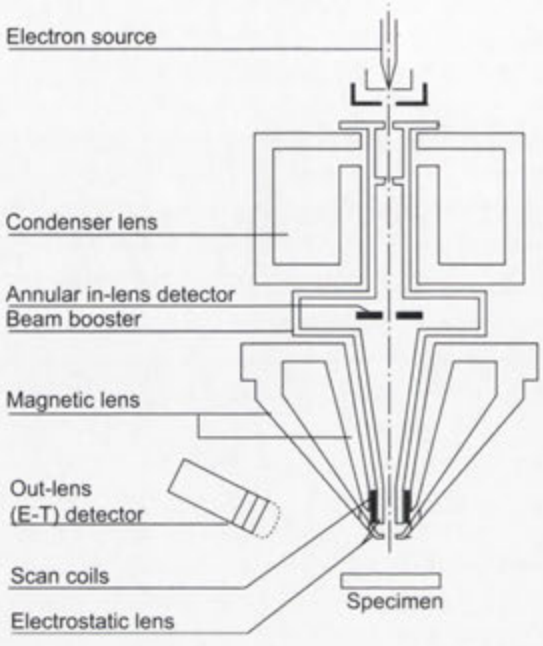

Fig. 8 Diagram of a SEM system with both ET detector and in-lens detector. Adapted from [117]

3.1.4 SE detector system

The diagram of an SEM system with both traditional SE detector (Everhart-Thornley (ET)) and in-lens detector is shown in Fig. 8. The retarding field applied by the electrostatic lens serves the functions not only to decelerate the incident primary electron beam but also to accelerate the SEs emitted from specimen into the lens system on a helical path. The positively biased ET detector positioned outside the lens system can detect both SE1s and SE2s, while in-lens detector placed on top of magnetic lens mainly favours the detection of SE1s [117,118].

3.2 Measurement of contact resistivity and sheet resistance

3.2.1 Four-point probe (4PP)

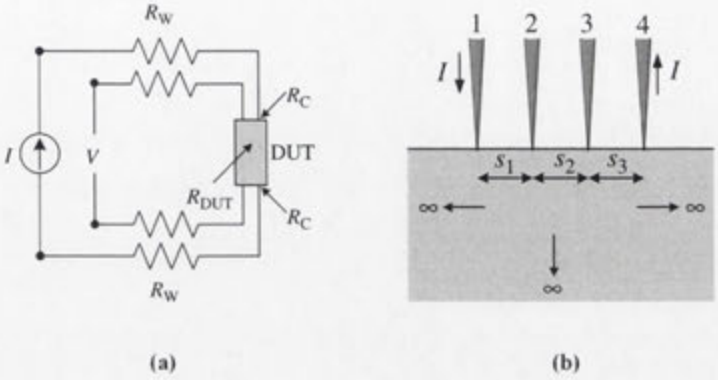

Fig. 9 (a) Measurement arrangement of 4PP (b) the current flow and voltage measurement of collinear 4PP. Adapted from [119].

The four-point probe (4PP) is one of the most widely used methods to measure the semiconductor resistivity, due to its simple operation and the ability to provide absolute measurement without using any calibration sample. The principle of 4PP measurement is shown in Fig. 9. Referring to the measurement arrangement in Fig. 9(a), the relationship between the total measured resistance R_T and the resistance of the device under test (DUT) R_{DUT} is given by [119]

$$R_T = \frac{V}{I} = 2R_W + 2R_C + R_{DUT} \ , \tag{3-1}$$

where R_c is the contact resistance and R_w the wire or probe resistance. Because the input impedance of the voltmeter is very high (around 10^{20} ohms or higher), the current flow through the voltage path is low; therefore, the voltage drops across the R_w and R_c are negligible, which means the measured V is essentially the voltage drop across R_T [119]. Equation (3-1), hence, can be simplified as below:

$$R_T = \frac{V}{I} = R_{DUT} \ . \tag{3-2}$$

In solar cell and other applications, rather than the resistance, the resistivity (ρ) and sheet resistance (R_{sh}) are of interest. Figure 9(b) shows the structure to deduce ρ as below [119]:

$$\rho = \frac{2\pi}{\left(\frac{1}{S1} - \frac{1}{S2+S3} - \frac{1}{S1+S2} + \frac{1}{S3}\right)} \frac{V}{I}, \tag{3-3}$$

where *S1*, *S2*, and *S3* are the probe spacing. In most practical applications, *S1*=*S2*=*S3*=*S*. Therefore, Eq. (3-3) can be simplified as [119]:

$$\rho = 2\pi S \frac{V}{I}. \tag{3-4}$$

This equation is based on the assumption that the DUT is semi-infinite, which is not true for the most samples in either the lateral or the vertical dimension. Hence Eqs. (3-4), need to be corrected for finite geometries with a calibration factor *F* as below [119]:

$$\rho = 2\pi SF \frac{V}{I}. \tag{3-5}$$

Detailed calculation of *F* can be found in references [119,120]. In most practical applications, the wafer area is much larger than *S* and the ratio of effective sample thickness (*t*) to probe distance is much smaller than 1, i.e. $t/S \ll 1$. Equation (3-5) reduces to [119]

$$\rho = 4.532t \frac{V}{I}. \tag{3-6}$$

The sheet resistance (R_{sh}) deduced from Eq. (3-6) is given by

$$R_{sh} = \frac{\rho}{t} = 4.532 \frac{V}{I}. \tag{3-7}$$

Besides the geometrical correction in the vertical direction for most wafer-based measurement, for laser applications, a lateral correction is also necessary since it is not practical to produce a large contiguous doped region by laser. In this thesis, the structure shown in Fig. 10 was used for 4PP measurement of laser-doped areas. In order to isolate the background current path, a high resistivity and opposite doping type wafer is used as the substrate. The laser-doped region is a 5.5 mm×1 mm box forming by overlapping multiple laser-doped lines. The sheet resistance of the laser-doped box is given by

$$R_{sh} = \alpha \frac{W}{S} \frac{V}{I}, \tag{3-8}$$

where α is the geometrical calibration factor to correct for the finite lateral dimension, and W the width of the laser-doped box. The α can be obtained experimentally by measuring the ratio of the V/I value of a localized diffusion region with a 5.5 mm×1 mm box structure to a full-wafer diffusion. It is found that when $W/S < 1$, which is satisfied for most 4PP set-ups, $\alpha \approx 1$ and R_{sh} is given by

$$R_{sh} \approx \frac{W}{S} \frac{V}{I}, when \ \frac{W}{S} < 1 \ . \tag{3-9}$$

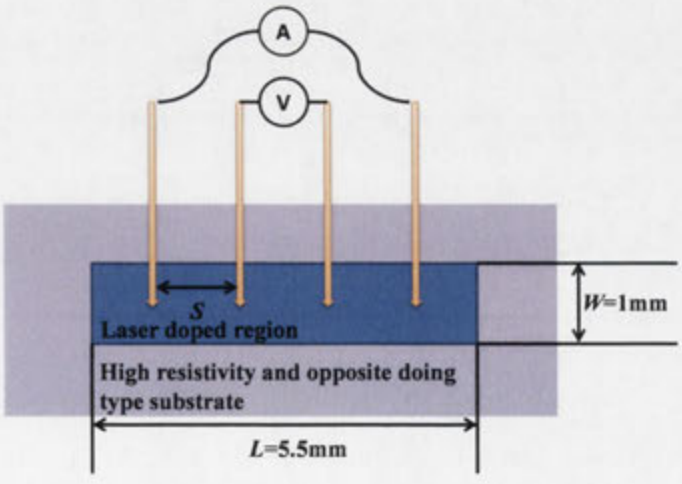

Fig. 10 Laser-doped box structure for 4PP measurement. L is the length of the laser-doped box.

The 4PP laser box method mentioned above is an easy and fast way to evaluate the doping, more generally the melting of silicon, achievable through laser doping process. Therefore, it is very useful for screening laser parameters. However, the 4PP measurement cannot offer information of contact resistance and the measurement itself might be influenced by the sample size, inhomogeneity of the doping profile, surface roughness or coatings [121].

3.2.2 Transmission line method (TLM)

To accurately assess the quality of laser-doped contacts, the contact resistance needs to be determined. The transmission line method (TLM), which was firstly proposed by Shockley [122], provides this information and can be applied to measure sheet resistance and contact resistance of laser doped lines [123,124]. The layout and data analysis of TLM used in this thesis is briefly reviewed below. More detail on the TLM method can be found in [119].

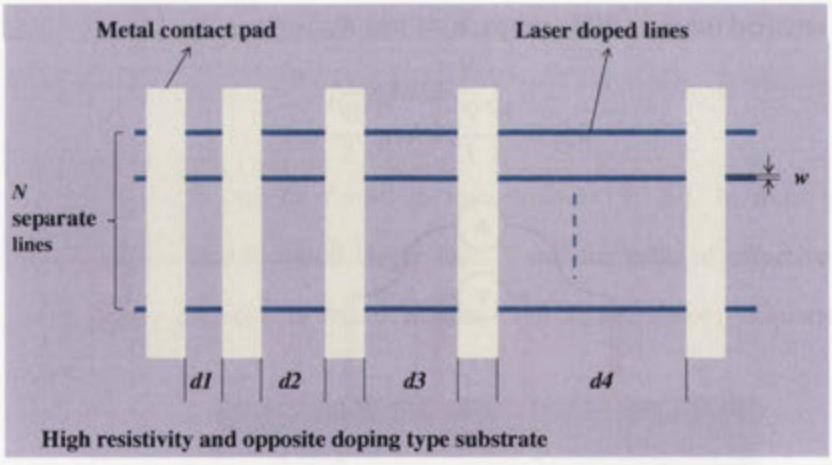

Fig. 11 The used layout of TLM for laser-doped lines.

In Fig. 11, five metal contact pads are used for measuring the resistances of several parallel laser-doped lines over four different pad distances. The parallel laser-doped lines in one TLM structure are produced by the same set of laser parameters under the same conditions. *N* is the number of laser-doped lines, *d1* to *d4* are the pad distances,

and w is the width of the laser-doped line. A high resistivity, opposite doping type substrate is normally used for current isolation. By plotting the measured resistances between any two adjacent pads against the corresponding pad distance, a linear relationship can be obtained as shown in Fig. 12. By defining the pad distance vector $\vec{d}$, and measured resistance vector $\vec{R}$, the linear regression of the TLM data is given by

$$\vec{R} = R_c + m\vec{d} \ , \tag{3-10}$$

where m is the slope of the linear regression, and R_c the intercept with y axis. The sheet resistance is given by

$$R_{sh} = mw \ . \tag{3-11}$$

w can be roughly measured using light microscope. However, because a laser-doped line normally has a rough edge and a non-uniform doping profile, accurate determination of w is difficult. Instead, line resistance R_L given below has more practical meaning.

$$R_L = \frac{R_{sh}}{w} = m \ . \tag{3-12}$$

The specific contact resistivity r_c is given by

$$r_c = \left(\frac{R_c}{2}w\right)^2 / R_{sh} \ . \tag{3-13}$$

By linear regression analysis of the standard deviation of m and R_c, symbolized as σ_m and σ_{R_c} respectively, the standard deviation of the sheet resistance ($\sigma_{R_{sh}}$), line resistance (σ_{R_L}), and specific contact resistivity (σ_{r_c}) can be deduced as:

$$\sigma_{R_{sh}} = \sigma_m w \ , \tag{3-14}$$

$$\sigma_{R_L} = \sigma_m \ , \tag{3-15}$$

$$\sigma_{r_c} = \frac{w^2 R_c}{2R_{sh}} \sqrt{{\sigma_{R_c}}^2 + \left(\frac{R_c}{2R_{sh}}\right)^2 {\sigma_{R_{sh}}}^2} \ . \tag{3-16}$$

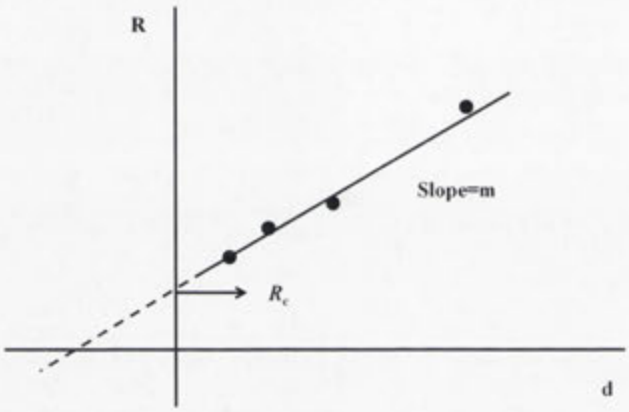

Fig. 12 Linear regression analysis of TLM data.

3.3 Measurement of recombination properties

3.3.1 General review of recombination

The number of minority carriers in silicon will increase following external excitations, for example the incidence of light. Those excess minority carriers will decay through the process of recombination to allow the system back to its equilibrium condition. In steady state, this process can be summarised as

$$J_{output} = J_{gen} - J_{rec} = \int_0^W qGdx - \int_0^W qRdx \ , \tag{3-17}$$

where J_{output} is the solar cell output current density per unit area (A/cm^{-2}), J_{gen} is the generation current density per unit area, J_{rec} is the recombination current density per unit area, G is the generation rate per unit volume (cm^{-3}·s^{-1}), R is the recombination rate per unit volume (cm^{-3}·s^{-1}), q is the elementary charge of an electron,

and W is the thickness of the sample. In open circuit condition, $G = R$, therefore, $J_{output} = 0$. In the extreme case, if R can be fully supressed, J_{output} will reach its upper limit $J_{output\_max} = \int_0^W qGdx$. From Eq. (3-17), it can be seen that the recombination rate determines whether and how many excited carriers can travel through silicon and finally be extracted out at contacts as electrical energy.

Beside recombination rate R, there are other two languages to describe the recombination — recombination lifetime (τ) and recombination current pre-factor (J_0):

Recombination Lifetime (τ) is the average time for an electron-hole pair to recombine following generation and is defined as

$$\tau \equiv \frac{\Delta n}{R}, \tag{3-18}$$

where Δn (cm^{-3}) is the excess density of electrons and $\Delta n = \Delta p$ (Δp is the excess density of holes) in the absence of trapping [125], which is assumed to be the case here.

Any experimentally measured τ is an effective value of the entire sample. As indicated in the reference [119], the effective lifetime is a property of the carriers within the semiconductor, which considers all influences on carriers including the silicon material properties and all types of possible recombination. The effective lifetime τ_{eff}, therefore, has a parallel relationship with each effect:

$$\frac{1}{\tau_{eff}} = \sum_i \frac{1}{\tau_i}, \tag{3-19}$$

where τ_i is the lifetime associated with each recombination mechanism within the sample.

Recombination current pre-factor (J_0) (in units of A/cm^2) is a mathematically defined parameter. The recombination current density per unit area (A/cm^2) through a

boundary surface of a region can be given by multiplying this parameter with the normalized excess *pn* product at the boundary, provided this parameter is injection level independent:

$$J_{rec} = J_0 \frac{pn - n_i^2}{n_i^2}\ , \tag{3-20}$$

where J_{rec} is the recombination current density per unit area (A/cm^2), n_i is the intrinsic carrier density, and p and n are the electron and hole concentrations evaluated at the boundary. Although at any boundary, based on Eq. (3-20), an "J_0" can always be calculated at a certain injection level, the concept of J_0 is attractive and useful only when it is injection level independent as indicated by its subindex zero. J_0, therefore, can only be applied for certain regions under certain conditions that enable an injection-level independent J_0. A highly doped region in low-level injection, for example, satisfies this requirement. Compared to R and τ, J_0 is a more convenient parameter for modelling of heavily doped regions since recombination in the region is defined by a single, lumped parameter [126,127].

Ideally, R, τ, and J_0 can be converted to each other in a strongly simplified case, for example under low injection level for a certain region within which τ and material parameters (like mobility) are constant and Δn is uniform, then:

$$J_{rec} = qRW_{region} = q\frac{\Delta n}{\tau}W_{region} = J_0\frac{pn - n_i^2}{n_i^2}\ , \tag{3-21}$$

where W_{region} is the region thickness. Here, J_{rec} is assumed to be constant over the thickness of that region.

In practice, τ is mostly used to characterise the silicon bulk, while J_0 is usually utilized for surface or highly doped region. It is important to note that R and τ are both injection dependent, so it is required to report lifetime together with the

corresponding Δn. In contrast, J_0 is injection independent but depends on the value of n_i, which in turn depends on temperature and is subject to revision; hence J_0 should be reported together with the used value of n_i.

3.3.2 Influence of recombination on solar cell performance

3.3.2.1 Influence on V_{oc}

In the reference [126,128], Swanson suggested the influence of recombination on the output voltage. To determine the output voltage, the band diagram of a representative p^+-base-n^+ solar cell in steady state under non-equilibrium conditions is shown in Fig. 13. In Fig. 13 φ_{Fn} and φ_{Fp} are the quasi-Fermi potential (i.e. chemical potential) of the electrons and holes respectively, and φ_{Fi} is the intrinsic Fermi level. The changes of these potentials within this solar cell have been illustrated using corresponding colours in Fig. 13. Due to the high concentration of majority carriers within the p^+ and n^+ regions, only a small gradient of quasi-Fermi potentials is required to drive a relatively large current. Hence, it is a reasonable approximation to assume φ_{Fp} constant through the p^+ region and its space charge region until the edge of the quasi-neutral base near the p^+ region at position 1. The same approximation can be applied to φ_{Fn} in the n^+ region and its edge at position 2. Then, the output voltage V_{out} can be given by

$$V_{out} = V_{jp} + V_{jn} + V_B + V_c + V_m \ , \tag{3-22}$$

where

$$V_{jp} = \varphi_{Fp}(1) - \varphi_{Fi}(1) = \frac{kT}{q} \ln\left(\frac{p(1)}{n_i}\right) , \tag{3-23}$$

$$V_{jn} = \varphi_{Fi}(2) - \varphi_{Fn}(2) = \frac{kT}{q}\ln\left(\frac{n(2)}{n_i}\right), \tag{3-24}$$

$$V_B = \varphi_{Fi}(1) - \varphi_{Fi}(2) . \tag{3-25}$$

V_c, V_m and V_B are negative value in normal operation and indicate the voltage loss caused by the resistance of contact, metal and base respectively. In the case that V_c and V_m can be neglected,

$$V_{out} = V_{jp} + V_{jn} + V_B = \varphi_{Fp}(1) - \varphi_{Fn}(2) . \tag{3-26}$$

From Eqs. (3-22) to (3-26), it can be seen that it is the separation of the quasi-Fermi potentials that mainly determines terminal voltage.

In the open circuit condition, as the total current equals to zero, V_c, V_m and V_B are zero. Therefore, Eq. (3-22) can be simplified as

$$V_{oc} = \frac{kT}{q}\ln\left(\frac{p(1)n(2)}{{n_i}^2}\right) . \tag{3-27}$$

To consider a p-type doped base with concentration of N_A and to assume the Δn is uniform in the base region, in low injection condition, Eq. (3-36) becomes

$$V_{oc} = \frac{kT}{q}\ln\left(\frac{N_A \Delta n}{{n_i}^2}\right) . \tag{3-28}$$

As indicated in Eq. (3-18), $\Delta n \propto \tau$, so in turn $V_{oc} \propto \ln(\tau)$. Therefore, in order to increase V_{oc}, the recombination requires to be controlled as low as possible.

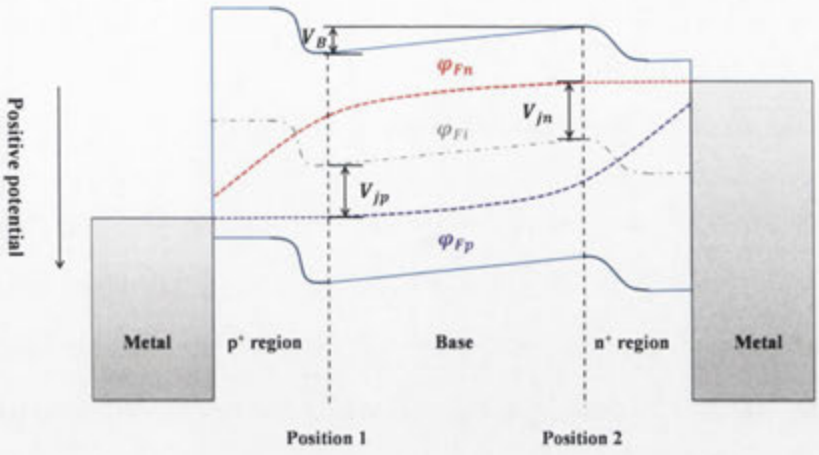

Fig. 13 Band diagram of a p^+-base-n^+ solar cell. Based on [126,128].

3.3.2.2 The influence on I_{sc}

As indicated in Eq. (3-17), I_{sc} is determined by the number of generated excess carriers that can diffuse to the contact before recombination, therefore the less the recombination, the higher the I_{sc}.

3.3.2.3 The influence on FF

In the absence of parasitic resistive loss, i.e. ignoring series and shunt resistances, Green [129] gives a simple but accurate expression of FF:

$$FF = \frac{v_{oc} - \ln(v_{oc} + 0.72)}{v_{oc} + 1}, \tag{3-29}$$

where

$$v_{oc} = \frac{V_{oc}}{\frac{n_{ideal} kT}{q}}, \tag{3-30}$$

where kT/q represents the thermal voltage, and n_{ideal} is the ideality factor.

From Eqs. (3-29) and (3-30), a higher V_{oc} will result in a higher FF. Since V_{oc} is

increased by reducing recombination, FF is also increased by reducing recombination.

3.3.3 Recombination of each part of the cell

For investigation purpose, rather than the total recombination of a given sample, the recombination property of a certain part of the cell is of more interest. The recombination theories for each part of the cell, including the bulk, the highly doped region and the surfaces, have been investigated by previous researchers and will be briefly reviewed below.

3.3.3.1 Bulk recombination

In the bulk, there are three well-known recombination mechanisms: band-to-band radiative recombination [130], Auger recombination [131], Shockley-Read-Hall (SRH) recombination [132,133]. The radiative and Auger recombination together are called intrinsic recombination, as they are unavoidable in silicon material. The SRH recombination is used to describe the defect assist recombination, which is a function of the substrate resistivity and the properties of the recombination centre. These three mechanisms are all injection dependant, with SRH dominating the low injection level while Auger the high injection level.

3.3.3.2 Surface recombination

The surface recombination is mainly related to the dangling bonds of silicon atoms at surface, which results from the discontinuity of crystalline structure [134]. Although the surface recombination can be calculated via a modified SRH model, it is more practical to extract the surface recombination from experiments by defining an effective surface recombination velocity S_{eff}.

$$J_{rec\_surf} = qS_{eff}\Delta n_{surf} \ , \tag{3-31}$$

where J_{rec_surf} is the surface recombination current density (A/cm^2), and n_{surf} and p_{surf} are the electron and hole concentrations at the surface. S_{eff} can increase, decrease or remain constant when the injection level changes as discussed by Aberle [135]

In low injection level, an effective surface recombination current pre-factor J_{0surf}, provided it is injection level independent, can also be used to describe the surface recombination as below:

$$J_{rec\_surf} = J_{0surf} \frac{p_{surf} n_{surf} - n_i^2}{n_i^2} . \tag{3-32}$$

The surface recombination (either S_{eff} or J_{0surf}), similar to SRH recombination, is dependent to the doping centration of the region which the surface contacts to.

3.3.3.3 Highly doped region recombination

The highly doped region near the surface has three main functions in solar cell. First, it works as a *carrier selective collector* [27]. As the name indicates, through forming significant conductivity difference between two types of charge carriers, the highly doped region facilitates the transport of only one type of charge carriers towards an external circuit but suppresses the other type. Second, the highly doped region offers a field passivation effect by reducing the concentration of one type of charge carriers. Last, the highly doped region is a necessary method to form low contact resistivity and low series resistance.

Due to the importance of the highly doped region, the analysis of the recombination property of this region is of great interest. The accurate theoretical modelling of this region is difficult. The doping profile in the highly doped region is normally not uniform and not easy to be accurately measured, especially for the laser-doped region. Further, the heavy doping effects [136,137], for example the band gap narrowing,

make the analysis rather complex. Therefore, a recombination current pre-factor (J_{0e}, the subscript e is used because this region is conventionally named as emitter) is used to collect all complicate effects into one experimentally measurable value, provided the highly doped region is in low injection level [27,138]:

$$J_{rec\_e} = J_{0e}\frac{p_e n_e - n_i^2}{n_i^2}\ , \tag{3-33}$$

where J_{rec_e} is the recombination current density (A/cm^2) of the doped region, and n_e and p_e is the electron and hole concentrations at the internal edge of the highly doped region [139]. However, in practice, the pn product at the edge of the space charge region in the base is used, because the pn product is constant with a small error across the space charge region [128].

3.3.3.4 Arbitrary boundary recombination

In some cases, it is not necessary to separate the recombination happening at different parts of a cell (for example, the surface and the diffused/doped region), but rather convenient to consider these parts together using an integral approach (or called *conductive boundary condition* method) as suggested by Alamo and Swanson [126,128,139]. In this way, a boundary is drawn at a suitable position to include all the parts of interest inside. All the recombination within the boundary can be obtained by calculating the recombination current flowing into the boundary surface. In the case that this boundary only includes the surface and the highly doped region, a recombination current pre-factor $J_{0boundary}$ can be defined as below, provided all the regions within the boundary are in low injection level:

$$J_{rec\_boundary} = J_{0boundary}\frac{p_{boundary} n_{boundary} - n_i^2}{n_i^2}\ , \tag{3-34}$$

where $J_{rec\_boundary}$ is the recombination current density per unit area (A/cm^2) within the boundary, and $n_{boundary}$ and $p_{boundary}$ are the electron and hole concentrations at the edge of the space charge region close to the base side.

3.3.3.5 Separating recombination of different parts

All experimentally measured lifetime is an effective value over the whole sample. In order to isolate the recombination of a specific region of interest, special sample structure and theory calculation based on some assumptions are required. The strategy is to create a case that the only unknown variable is the recombination of the interested region. For example, if J_{0e} of a highly doped region is of interest, the influences from surfaces and bulk have to be suppressed or calculated, which can be done by using good surface passivation (i.e. assuming zero surface recombination velocity) and high quality FZ wafers (i.e. only considering intrinsic recombination, which can be theoretically calculated).

3.3.4 Lifetime measurement strategy

Nagel *et al.* [140] summarized the lifetime measurement principle as below:

$$\tau_{eff} = \frac{\Delta n_{av}(t)}{R_{av}(t)} = \frac{\Delta n_{av}(t)}{G_{av}(t) - \frac{\partial \Delta n_{av}(t)}{\partial t}}, \tag{3-35}$$

where G is the generation rate. G and Δn can be varied with time (t). The subscripts *eff* and *av* are used to emphasize the essence discussed above that all the experimentally measured parameters are the effective or averaged values over the sample.

As indicated by the Eq. (3-35), the lifetime can be calculated if $\Delta n_{av}(t)$, $R_{av}(t)$ can be determined. Therefore, the strategy to measure the lifetime consists of three steps as below:

A. To measure a parameter that is closely related to the $\Delta n_{av}(t)$, for example:
   - ✧ Conductivity (Photoconductance)
   - ✧ Emission of photon (Photoluminescence)
   - ✧ *etc.*

B. To measure the $R_{av}(t)$, for example:
   - ✧ Quasi-steady-state (QSS), which is done by determining the generation rate and assuming the $R_{av}(t) = G_{av}(t)$ at quasi-steady-state
   - ✧ Transient, which is done by determining the time dependence of Δn $(\frac{\partial \Delta n_{av}(t)}{\partial t})$ and assuming there is no generation
   - ✧ Generalized, the combination of QSS and Transient

C. Data analysis based on the methods used in Step B

Based on the same strategy, using different options in each step, several techniques have been developed and some of them are commercially available. In the following Sections 3.3.5 and 3.3.6, two lifetime measurement techniques used in this thesis will be briefly reviewed.

3.3.5 Photoconductance

A light (or other excitation sources) can be used to excite the sample to generate electron-hole pairs which will change the conductance of the sample. Following the Step A in Section 3.3.4, by monitoring the excess photoconductance, for example using inductive coil method, the excess carriers concentration can be calculated as given by [119]:

$$\Delta\sigma = q\left(\Delta n_{av}\mu_n + \Delta p_{av}\mu_p\right)W = q\Delta n_{av}\left(\mu_n + \mu_p\right)W \ , \tag{3-36}$$

where $\Delta\sigma$ is the excess photoconductance, μ_n and μ_p are the electron and hole mobilities. The mobilities can be calculated according to the doping and injection level [141,142].

Based on the different methods used in Strategy B, there are three main techniques: *transient photoconductance decay* (TPCD) [119,143], *quasi-steady-state photoconductance* (QSSPC) [119,144] and *generalized photoconductance* [140]. The measurement conditions and data analysis methods will differ depending on which technique is used. In terms of which method needs to be used in practice, Table 3 compares the TPCD and QSSPC [144]. The generalized method is not compared as it is a combination of TPCD and QSSPC.

Table 3 The comparison between TPCD and QSSPC [144]

	TPCD	**QSSPC**
Measurement of photon flux	No	Yes
Measurement of sample optical property in advance	No	Yes
Light pulse	very short (complex, expensive)	Long, slow varying (relatively simple, cheap)
Measurable lifetime range	≥ 50 μs [144] (easily and accurately); ≥ 10 ns [144,145] (sophisticated instruments required)	Wide (limited by signal strength; > 3 ns in reference [144])
Injection dependence	Yes	Yes

3.3.6 PL imaging

If the sample surface is irradiated by photons with energy larger than the silicon band gap energy and the incident photon has an uniform intensity across the sample surface, photons generated from the entire sample due to band to band recombination can escape from the front surface (i.e. photoluminescence, shortened as PL) and can be captured by a camera sensor to generate a spatially-resolved 2D image. The pixel count of this image is directly related to local PL emission that is determined by the local

excess carriers concentration as [146-149]:

$$I_{PL} = ABp_{local}n_{local} = AB(p_{0local} + \Delta n_{local})(n_{0local} + \Delta n_{local}), \qquad (3\text{-}37)$$

where I_{PL} is the pixel intensity (in counts), i.e. the measured local PL signal, A is a scaling factor which takes into account the fact that in most cases the pixel count is measured only in relative units, B is the radiative recombination coefficient, Δn_{local} is the local excess carrier concentration, and n_{0local} and p_{0local} are the local equilibrium concentration of electrons and holes. B is assumed to remain constant for low injection level [149]. From Eqs. (3-37) and (3-18), it can be seen that the PL image is a direct reflection of the lateral lifetime distribution across the sample.

In most PL image systems, a diode laser with ~800nm wavelength having low intensity variation (<5%) across the sample area is used to illuminate samples [146]. The band-to-band emission from crystalline silicon at room temperature is a broad spectrum, which can be partially detected with a silicon CCD camera and almost completely with InGaAs detectors [150]. A long-pass filter between the sample and the CCD camera is used to block the laser reflection from the sample surface [146], while a short-pass filter is suggested for partially reducing the smearing effects (more discussion in next paragraph) [151,152]. The illumination laser intensity and the exposure time are controlled by computer to achieve images with high signal to noise ratios [146]. As a contactless method, PL imaging can be used at any fabrication stage without the requirement of any metal or specific cell structure. The fast measurement speed and 2D spatially-resolved results with pixel resolution of as low as several tens of μm make PL imaging a very powerful tool. As the PL signal can be related to many different properties of silicon, PL imaging can be used for a variety of imaging applications, for example imaging carrier lifetime [146,153,154], series resistance [155], shunt resistance [156], iron concentration [157,158], and the J_{0e} and sheet resistance of contiguous laser-doped region [159]. With the help of numerical simulation, as introduced in Section 3.3.7, PL imaging can be applied to analyse the

recombination property of small/localized features generated by laser process.

One challenge for PL imaging is to accurately characterize the luminescence signal at highly localized features, which is mainly caused by three lateral smearing effects in PL imaging:

1) **Light smear in the sample**. The photon emission within the sample is isotropic. Photons may be reflected several times at the front and rear surfaces of the sample before being coupled out, especially when the sample surfaces are rough or textured. Photons can escape from the sample at a location where they were not originally generated and reach the camera, causing smearing [160-162];
2) **Carrier smear in the sample**. If the carrier concentration is non-uniform across the sample, carriers start to diffuse. If the carrier diffusion length is comparable to the feature of interest in PL images, the carrier smear will have a noticeable influence [163,164];
3) **The infrared photon smear within the silicon CCD** [152,165,166]. Because the silicon used for the sensor elements in the CCD camera is a weak absorber of the near-infrared luminescence spectrum, photons may be absorbed in a different pixel (element) from the element on which they were initially incident.

Some methods can be employed to control the three lateral smearing effects respectively:

1) If the sample has smooth, planar surfaces, the influence of light smear is nearly eliminated. The use of a short-pass filter can further control this effect since the light smear is dominated by long wavelength light [160-162].
2) Phang *et al.* suggested a post-measurement data process to compensate the carrier smear. However, this method is highly sensitive to the measurement noise [163]. Therefore, in practice, if localized PL signal is of interest, optimization of the layout of testing patterns is a better choice, for example increasing the size of the test pattern, and arranging the patterns with similar recombination properties

together to reduce carriers diffusion.

3) A short-pass filter can partially control the photon smear in the silicon CCD [151,152]. A post-processing deconvolution that is based on quantifying the point-spread function of the used censor can further correct this effect [152,165,166].

3.3.7 Localized recombination property analysis

The dimensions of the laser processed regions are in the range of several μm, so techniques only obtaining average lifetimes of a relatively large area, such as QSSPC, are not suitable for analysing laser processed samples. PL imaging can provide spatially-resolved lifetime information; however, the pixel resolution of most commercial PL imaging equipment is not high enough for analysing μm sized features. For example, the pixel resolution of the PL imaging equipment in the author's lab with the maximum magnification lens can only reach ~21 μm/pixel, which means the critical dimension of a laser processed region can only be presented by ~ 1 pixel in the PL image. In addition to the poor pixel resolution, the smearing effects in PL imaging as discussed in Section 3.3.6 makes the direct application of PL imaging impractical.

Fortunately, by applying advanced analytical models [167-170] or by using numerical simulation tools [127], the surface recombination properties of a regular array of small features can be extracted from a relatively large-area measurement. Because the analytical models make several simplifications and assumptions, which do not strictly apply in practice, in this thesis, numerical simulation is used. More specifically, the advantages of using the numerical simulation, compared to analytical methods [127], are listed below:

- The sample can be measured under any injection level, instead of only low injection for analytical method;
- The series resistance is more accurately estimated;

- Finite or spatially varying bulk lifetimes are taken into account;
- Non-uniform carrier profiles are taken into account;
- Non-uniform and injection dependent recombination at boundaries is taken into account;
- Non-uniform excess carrier density can be applied to surface and local features.

The localized recombination analysis based on the numerical simulation tool of Quokka [171] has been introduced in details by Fell *et al.* in their publication [127]. Here, only a short summary of Quokka and the localized recombination analysis procedure are given.

3.3.7.1 Quokka

Quokka is a freely available 1/2/3-D solar cell simulation tool developed by Fell [171]. The fast simulation speed of Quokka results in part from two important simplifications: quasi-neutrality in the bulk [172] and conductive boundaries [126,128,139]. Firstly, by assuming quasi-neutrality in the bulk, solution of the Poisson equation is no longer necessary. Secondly, the conductive boundary assumption, as also discussed in Section 3.3.1, allows the use of recombination current pre-factor ($J_{0boundary}$) to simplify the recombination model of the highly doped region and surface. In this way, it is not necessary to consider the complex doping profile, heavy doping effects and space charge regions any more. If non-ideal recombination is present, non-ideal recombination current pre-factor (J_{02}) can be included in the conductive boundaries. The model of Quokka is briefly summarized in Fig. 14, where the most important simulation inputs are highlighted in red. In Fig. 14, φ_{Fn} and φ_{Fp} are the quasi-Fermi potentials of electrons and holes, σ_n and σ_p are the conductivity of electrons and holes, R_{sheet} is the sheet resistance of a diffused region (to set to extremely high for no diffusion), V_{ext} is the external voltage, φ_F is the equilibrium Fermi potential, and $\vec{n}$ is the normal vector for the corresponding surface. There are two modes within

Quokka — an operation mode and an optimization mode. In the operation mode, after inputting all required parameters, Quokka will run the simulation and provide the outputs of interest, such as V_{oc}, excess carriers distribution, I-V curves and *etc*.. In the optimization mode, which is important for the work in this thesis, Quokka can fit one unknown input parameter according to the designated output. As Quokka has integrated the function of predicting PL signal, when the measured PL signal is designated as the optimization goal, the localized recombination property of the laser processed region can then be extracted as introduced in next section.

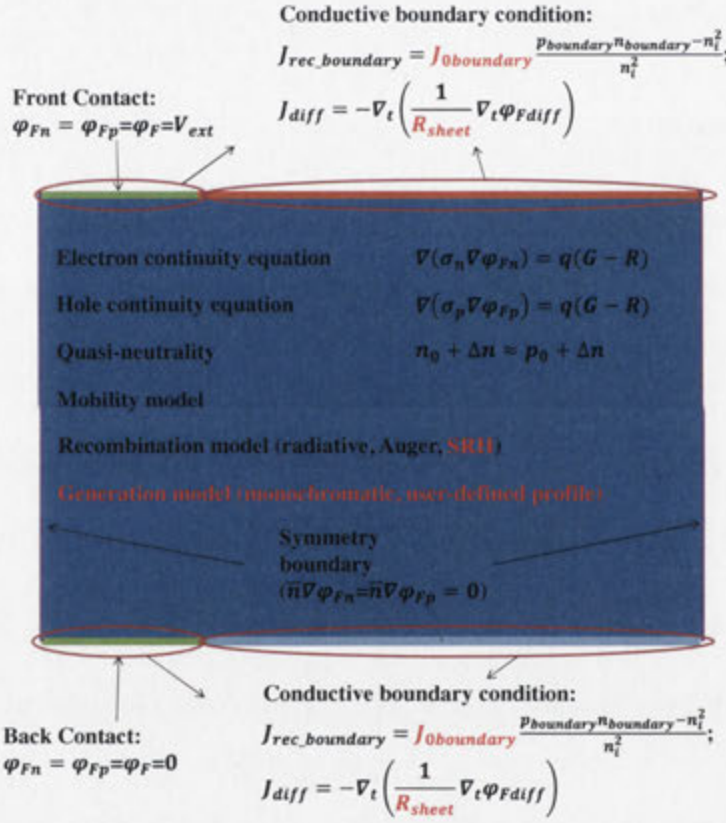

Fig. 14 Summary of the mathematical model used in Quokka.

3.3.7.2 Experiment procedure and data analysis

The details of the experimental procedure and data analysis can be found in reference [127]. The procedure and the parameters flows have been summarized in Fig. 15. An

example of the application of this method and a more detailed description of the analysis procedure can be found in Section 6.3.

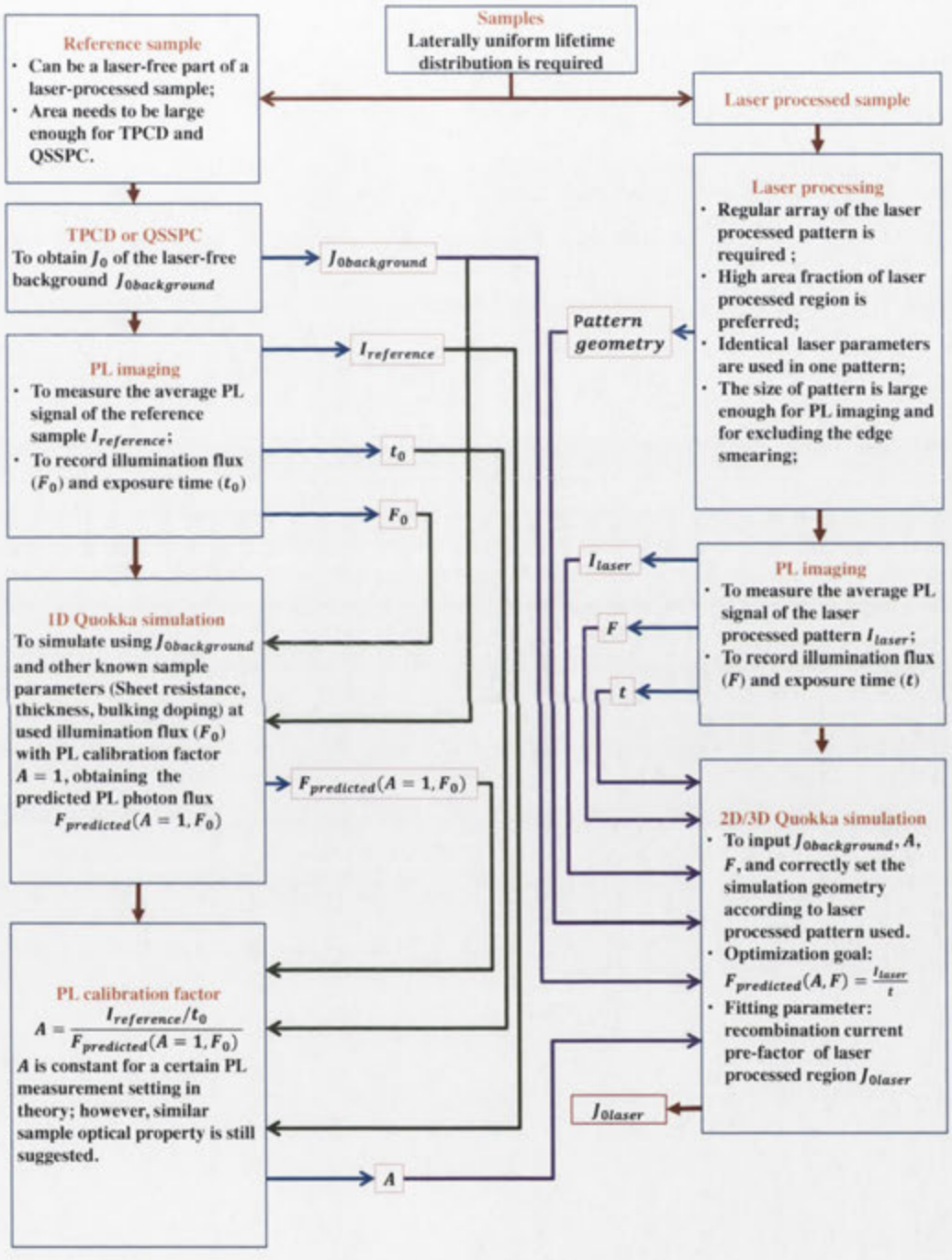

Fig. 15 The experimental and data analysis procedure of localized recombination measurements.

4 Secondary electron microscopy dopant contrast imaging (SEMDCI)

4.1 Motivation

An effective way to evaluate the quality of laser doping is to measure its cross-sectional dopant distribution. Previous researchers have achieved this goal using Secondary Ion Mass Spectroscopy (SIMS) [17,63,119,173,174] and Electron Beam Induced Current (EBIC) [17] measurements. SIMS has high sensitivity to dopant concentration, but there are also three significant disadvantages. Firstly, SIMS cannot distinguish between active and inactive dopants [175]. Secondly, the spatial resolution of SIMS is limited, so that the depth profile values obtained from SIMS are mean values over a relatively large area [17,73]. Last, SIMS in particular is time-consuming and expensive. The main drawbacks of the EBIC technique are that the shape of the EBIC curve depends on the surface recombination velocity of the surface where the beam impinges [176] and that it only gives information on the location of the p-n junction but not on the dopant density profile. EBIC, though relatively simple, still requires significant sample preparation in most cases, as well as electrical contacting in the microscope. Therefore, developing fast and cheap dopant mapping methods is of great interest. In this chapter, secondary electron microscopy dopant contrast imaging (SEMDCI), will be used in order to image laser-doped cross-sections. To the author's knowledge, this is the first time the application of this technique for this purpose has been reported.

4.2 History

SEMDCI itself is not a new technique. It was first observed in 1967 that a contrast exists between p-doped and n-doped regions in certain secondary electron images (SEI)

obtained by a scanning electron microscope, where p-doped regions appear brighter than n-doped regions [177]. In 1995, Perovic *et al.* found the contrast observed by SEI is not only related to doping type but also depends on doping concentration levels [178]. The most significant advantage of SEI is its fast data measurement speed, high spatial sensitivity and simple sample preparation.

Many attempts have been made by previous researchers to correlate the SEI dopant contrast with the doping concentration in order to use SEMDCI as a quantitative method to characterize doping profiles. A roughly linear relationship between the observed contrast and the logarithm of the dopant concentration in p-type silicon has been observed by several authors. It was reported that a doping concentration as low as $\sim 10^{16}$ can be measured and a doped line as thin as 1 nm can be detected though the spatial resolution is only ~19 nm [178-183]. Most studies of the quantitative application of SEMDCI are based on p-type diffused samples. For the quantitative analysis of n-type doping, to the authors' knowledge, there is no relevant report to date. Though some theories have been proposed during past decade, unfortunately, there is not a commonly accepted theory for SEMDCI and different microscope setups used for SEMDCI have slightly different properties. As a result, it is not possible to derive a universally applicable, analytical relationship relating dopant contrast and dopant concentration. Hence, the focus is on establishing an empirical relationship which may be slightly different for each instrument.

4.3 Mechanism

There is not a complete theory that can fully explain the mechanism of the dopant contrast, and predict quantitatively the contrast observed under a wide range of conditions. However, during past decades many researchers have proposed some possible theories that are in good qualitative agreement with at least some or most observations. The theories can be roughly classified into three groups.

4.3.1 Surface-induced energy band bending theory

Perovic *et al.* , first proposed this theory in 1995 [178]. Surface states generated by the disruption of the periodicity of the lattice at the surface pin the Fermi level of silicon, causing band bending close to the surface of the semiconductor. The resulting surface internal electric fields accelerate electrons from p-type doped regions to the surface but repel electrons from n-type doped region from the surface, as shown in Fig. 16 [178]. This theory was further supported and enhanced by other researchers [184] who extracted surface band bending from Kelvin probe force microscopy measurements and found surface band bending is the main factor determining the dopant contrast.

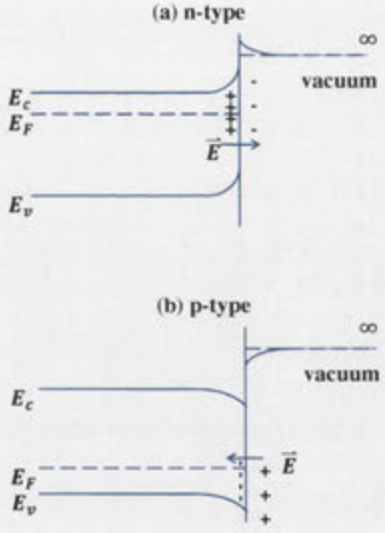

Fig. 16 Energy band diagrams showing the band bending due to surface states of (a) n-type and (b) p-type silicon. Adopted from [178].

4.3.2 Theory based on work function effects

Sealy *et al.* in 2000 [179] proposed this theory. When two materials are brought into contact, contact voltages occur as a result of the alignment of Fermi levels. In order to be collected by detectors, the emitted electrons must have sufficient energy to surmount the higher energy barrier of either the SEI detector level or the vacuum level. Therefore extra energy is required for the SEs emitted from the n region compared to

that of the p region [179], as shown in Fig. 17. Further experimental results by Cazaux[185], Elliott *et al.* [183] and Buzzo *et al.* [186] provided strong support for this theory. An extension of this theory was proposed by Schonjahn *et al.* [187], who pointed out that because the barrier height is smaller for the SEs escaping from the p region than from the n region, the number of SEs emitted with small angles to surface normal is larger for SEs from the p region compared to the n region. Therefore, for small collection angles of the detector, more SEs are collected from the p region than the n region, resulting in contrast as observed.

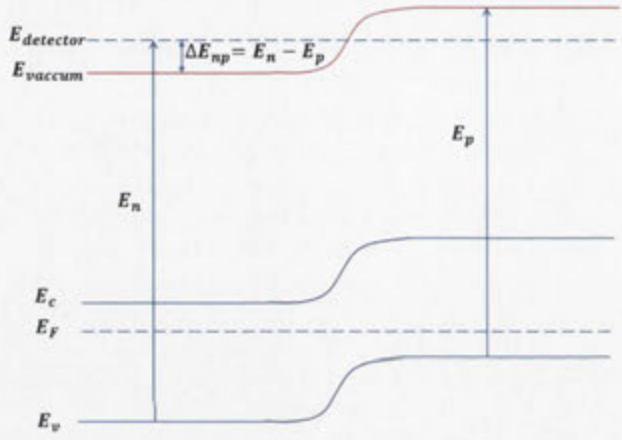

Fig. 17 Band diagram of the p-n junction showing an extra energy ΔE_{np} is required for SE emission from the n-type region compared to the p-type region. Adopted from [179].

The theories of Sections 4.3.1 and 4.3.2 can be combined together, as shown in Fig. 18. The band bending has two effects. Firstly, it will decrease the built-in potential between the n region and p region (decreasing from ΔE_{np} to $\Delta E_{np}{}'$) reducing the contrast caused by work function effects. Secondly, it will generate surface internal electric fields that accelerate electrons from the p doped region but suppress electrons from the n doped region. In other words, band bending is a mechanism that can both increase and decrease the dopant contrast. Calculations, therefore, are needed to determine the net effect of band bending. Sealy *et al.* developed a model and found that the extra energy required for SE emission from the n-type region as a result of surface band bending is only ~0.02 eV, which is negligible compared to the ~0.5 eV difference

caused by the work function effect [179]. However, the opposite conclusion was obtained by Volotsenko *et al.* [184]. Volotsenko *et al.* defined the dopant contrast as

$$C_{pn} = \frac{\lambda_{esc}^{p} B_p}{\lambda_{esc}^{n} B_n} - 1 \ , \tag{4-1}$$

where λ_{esc}^{p} and λ_{esc}^{n} are the mean escape depth of SEs of p-doped and n-doped regions respectively, and B_p and B_n are the electron escape probability of p-doped and n-doped regions respectively. The near-surface internal electric fields resulting from surface-induced energy band bending are directly related to λ_{esc}^{p} and λ_{esc}^{n}, while the work function effect is represented by B_p and B_n. Volotsenko *et al.* found that λ_{esc}^{p} and λ_{esc}^{n} contributes 89 % of the total calculated contrast, compared to 11 % for B_p and B_n. These two models both have their assumptions and limitations. The general conclusion is that the dopant contrast observed in SEI is not the result of a single mechanism, but rather the result of multiple mechanisms that interact in a complex way. This is the main reason why it has proven difficult to build up a quantitative method based on dopant contrast in SEI.

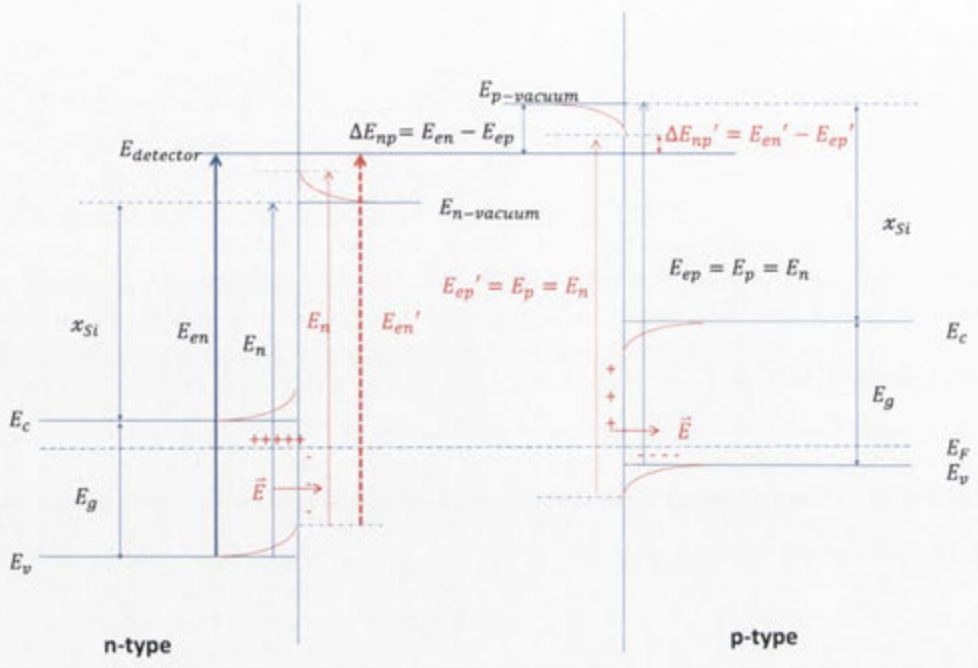

Fig. 18 Synthesis of the two theories for contrast formation outlined above. Red lines and symbols in the diagram represent the situation when surface band bending is taken into account.

4.3.3 Metal-silicon contact theory

El-Gomati *et al.* [188,189] considered the effect of contamination on the surface of samples. When samples are prepared, transported or stored in air for a long time, the surface of the samples often builds up a layer of contaminants, consisting chiefly of hydrogen, carbon and oxygen. El-Gomati *et al.* observed the formation of a carbon rich film similar to graphite on their samples. The properties of this graphite film are similar to those of metal films and therefore a metal-silicon contact forms at the surface. Because the work function of the graphite is larger than that of silicon, the energy bands of n^+, n and p doped silicon samples all bend upwards. Therefore a Schottky contact forms between graphite and n^+ or n doped silicon, while an ohmic contact forms for p doped silicon [188,189]. Though El-Gomati *et al.* proposed a useful idea, the descriptions of the exact mechanism in their papers are not clear. Here, I interpret this theory as shown in Fig. 19. When graphite carbon forms on the surface,

the energy bands of n^+, n and p/p^+ all bend upwards, because the work function of graphite carbon is larger than that of the silicon. Electrons are firstly transferred from silicon to the graphite then emitted from graphite to the graphite vacuum level or detector level. The energy of SEs required for emission from graphite to the detector or vacuum is the same for all types of silicon, so the main difference resulting in different SEs yield among differently doped regions is the energy to transfer electrons from silicon to metal. Because the electrons are depleted at the surfaces for all types of regions, very few electrons are present in the conduction band. Therefore, the SEs originate from electrons in the valence band. Because band bending for n doped silicon is larger than for p doped silicon, ($\Delta E_n > \Delta E_p$), more energy is required to transfer electrons from n doped silicon. For n^+ silicon, the energy barrier created by band bending becomes sufficiently narrow that electrons are able to tunnel through the barrier. Therefore, the energy required for SEs to be collected by the detector is smallest for n^+ silicon. Therefore, the effect of such a graphite film on the surface is to change the brightness(B) of doped silicon such that $B_{n^+} > B_p > B_n$.

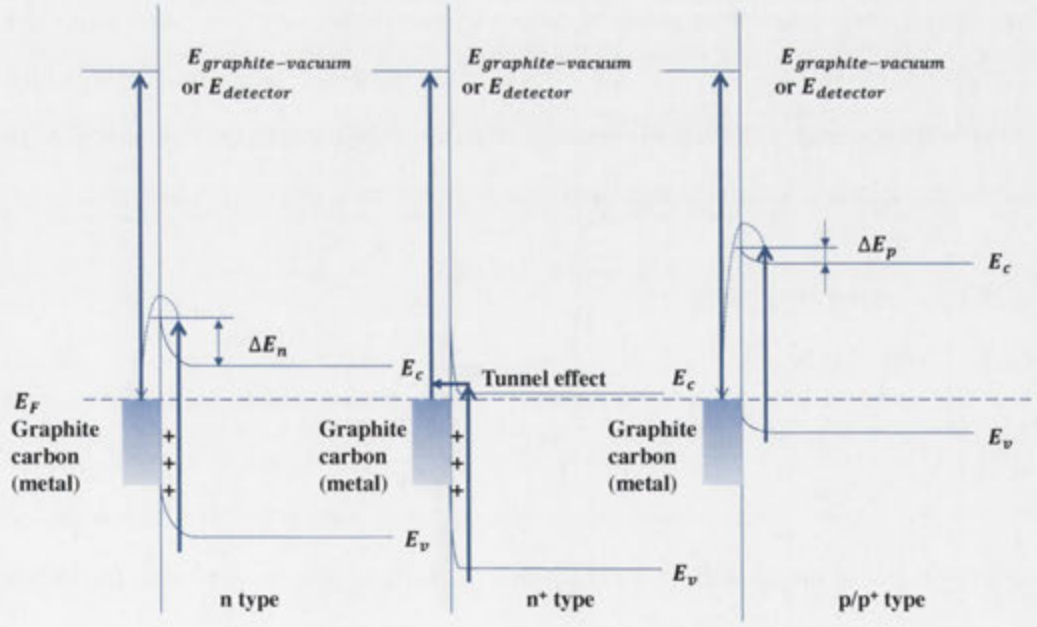

Fig. 19 Band diagrams illustrating the metal-silicon contact theory

4.3.4 Conclusion

In summary, theories in Section 4.3.1 and 4.3.2 can be combined to explain the dopant contrast observed on freshly cleaved samples, while the theory in Section 4.3.3 can be used to explain the contrast reversal phenonnon frequently observed for samples stored in air for a long time, whereby n^+ doped silicon regions that initially appear dark, become bright after storage for an extended period of time.

4.4 Determination of suitable SEM parameters

SEMDCI can be used in at least two different ways. At a basic level, it can be employed to delineate between heavily doped regions and the underlying substrate, giving information about the extent and shape of the doped region. For this application, all that is required is that there is good contrast between the substrate and the laser-doped region. In a more sophisticated application, image contrast within the laser-doped region is used to obtain quantitative or semi-quantitative information about the dopant density variation within the laser-doped region. This is discussed in more detail in Section 4.6. Here I focus on the broad range of parameters over which reasonable contrast is obtained between heavily doped (n or p) regions and an underlying substrate of opposite doping type.

4.4.1 Experimental

For the convenience of wafer cleaving, <100> wafers were used. For n-type laser-doped or diffused samples, p-type substrates were used and vice versa. Wafers were single side polished or saw-damage etched prior to processing. The dopant source for n-type laser doping is different according to the laser system used. For the DPSS laser, phosphorus-spin-on dopant (P-SOD) P509 commercially available from Filmtronics Inc. was used (this solution was used as P-SOD for all the experiments in this thesis), while phosphoric acid solution was applied for the LCP system. P-type

laser doping samples were processed by DPSS laser and Excimer laser. Boron-spin-on-dopant (B-SOD) B155 commercially available from Filmtronics Inc. (this solution was used as B-SOD for all the experiments in this thesis) and evaporated Al were used as dopant sources for DPSS laser, while atomic layer deposition (ALD) Al_2O_3 was applied for the Excimer laser. Most samples were cleaved just before loading into the SEM. The Zeiss UltraPlus Field Emission Scanning Electron Microscopy (FESEM) is the equipment used in all experiments. Some samples were deliberately stored in air for several days. Boron and phosphorus diffusion samples were prepared for comparison with laser-doped samples.

4.4.2 Results and discussion

Four main FESEI parameters are considered here: detector type, accelerating voltage (AV), working distance (WD) and aperture size. To isolate the influence of each parameter, when one parameter was varied, all other parameters were kept constant.

4.4.2.1 Detector type

The detection yield of back scattered electrons (BSE) is directly related to changes in the mean atomic number of the sample being studied, and is not considered capable of imaging the dopant contrast of semiconductors at the normally used doping concentrations in the order of 10^{17}-10^{20} cm^{-3}, which correspond to between 0.02 and 0.0002 at % [179,183,190,191]. Therefore, only secondary electron detectors were used in experiments. Theoretically, the dopant contrast could be seen in both the upper (through-the-lens) and lower (conventional SE) detectors, but it is enhanced in through-the-lens mode due to the preferential collection of pure SEs (i.e. SE1) produced from the near-surface region of samples and the suppression of the contribution from SE2 or the SEs produced by scattering from the lens, pole-piece and chamber walls [179,180,190]. In our experiments, the dopant contrast was seldom

observed in conventional SE mode.

4.4.2.2 Accelerating voltage

An accelerating voltage (AV) from 0.5 to 20 kV was used in previous investigations [179,180,183,189,191,192] for dopant contrast delineation. In our experiments, it was found that for boron diffused samples the available AV window is in agreement with that reported in the literature, with an extension of the lower limit to 0.2 kV. For phosphorus diffused samples, 1 kV to 3 kV is the optimum working window; although the dopant contrast is still visible above 4 kV, the edge effect (shown in Fig. 20 below) strongly interferes with the pure doping contrast, making interpretation difficult. In contrast to diffused samples, for both n- and p-type laser-doped samples the dopant contrast was observed to disappear for AV > 7 kV, despite the fact that the surfaces of laser-doped regions are generally more heavily doped than for the diffused samples. The reason for this observation is not yet understood. Although the AV working window is relatively wide, especially for p-type samples, AVs at the low or high end should be avoided. Very low AVs are likely to cause sample surface contamination, high image noise and difficulty in focus finding, while high AVs tend to result in electron scan damage and a more pronounced edge effect as shown in Fig. 20.

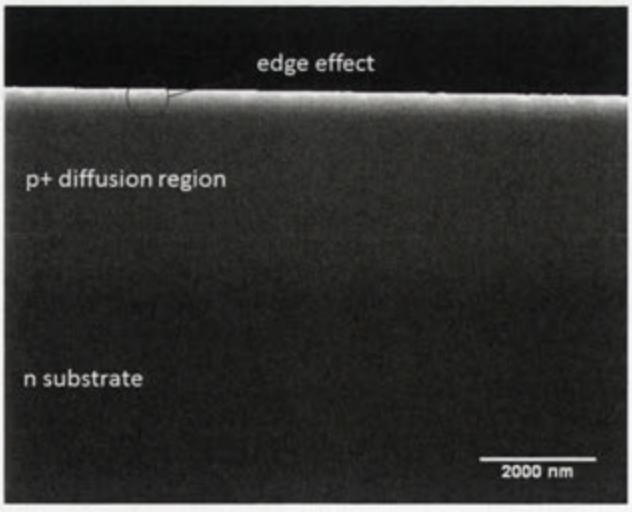

Fig. 20 Edge effect caused by high AV (7 kV) in a boron diffused sample.

4.4.2.3 Working distance

Relatively short working distance (WD) (below 6mm) were used by previous researchers [179,183,184,192,193]. It was reported that a shorter WD will enhance the dopant contrast in most cases [179,184]. However, Schonjahn *et al.* [187] found the opposite phenomenon. They found that the detector's collection angle is a function of the WD and decreases for larger WD. Considering the dopant contrast is also related to the SE angular distribution, the contrast for a small WD was found to be always lower than for a large WD in their experiments [187]. Practically, in this work, it is found for all samples that dopant contrast can be seen at a WD from 1-6 mm. Though the dopant contrast can still be seen at a WD as large as 10 mm for some samples, a large WD will significantly increase the image noise and reduce the image resolution. A very low WD, such as 1 mm, is not recommended since it results in significant electron scan damage.

4.4.2.4 Aperture size

Six available aperture sizes (7.5/10/20/30/60/120 μm) were tested. Using different aperture sizes under the same AV is actually an indirect way to adjust beam current. It was found that small apertures, such as 7.5 and 10 μm significantly reduce the signal intensity, while large apertures, such as 120 μm, result in low resolution, significant substrate charging and a strong edge effect. 30 μm and 60 μm size apertures were found to be optimal and were used in this work.

4.4.2.5 Sample preparation

One of the advantages of SEMDCI is the simple sample preparation. In the published literature it has been reported that p-type samples need to be freshly cleaved immediately prior to insertion in the FESEM, but that a HF dip is not necessary. [181,183]. However, n-type doping contrast was reported to be weak unless the sample

was HF dipped before loading into FESEM [179].

In this work, it is found that for all samples, regardless of whether the doped region is n- or p-type, dopant contrast can be observed without a HF dip. Furthermore, the condition that the samples need to be freshly cleaved was also found to be not necessary. After storing samples in a clean box for several days in air, the dopant contrast was still visible. However, for n-type laser-doped samples, following long time exposure to air, the contrast between the n- and p-type regions was reversed, as shown in Fig. 21. This phenomenon only happens to n^+-p samples but not to p^+-n samples. This is believed to be the result of the formation of a high work function surface layer, as discussed in Section 4.3.3.

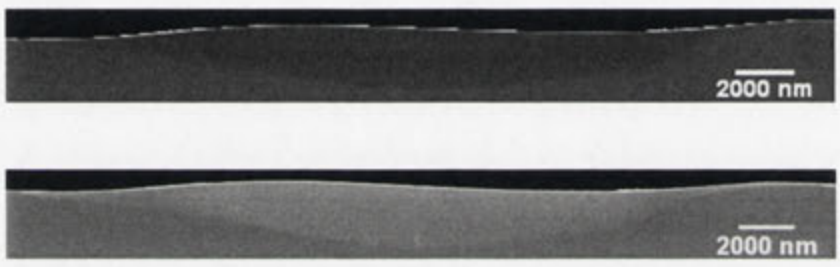

Fig. 21 Contrast reversal in n-type laser-doped samples after a long exposure to air:(a) freshly cleaved stample; (b) following storage for 8 days in air.

4.4.2.6 Applicability

Different dopant sources and doping methods were used to test the applicability of SEMDCI. It was found that SEMDCI can be applied to all the laser-doped and diffusion samples prepared in this study. Examples of laser-doped samples are shown in Fig. 22. This demonstrates that SEMDCI doesn't depend on certain dopants or laser sources. Observation of laser processed but undoped samples did not reveal any contrast; this confirms that the observed contrast is due to doping and not crystallographic or other effects.

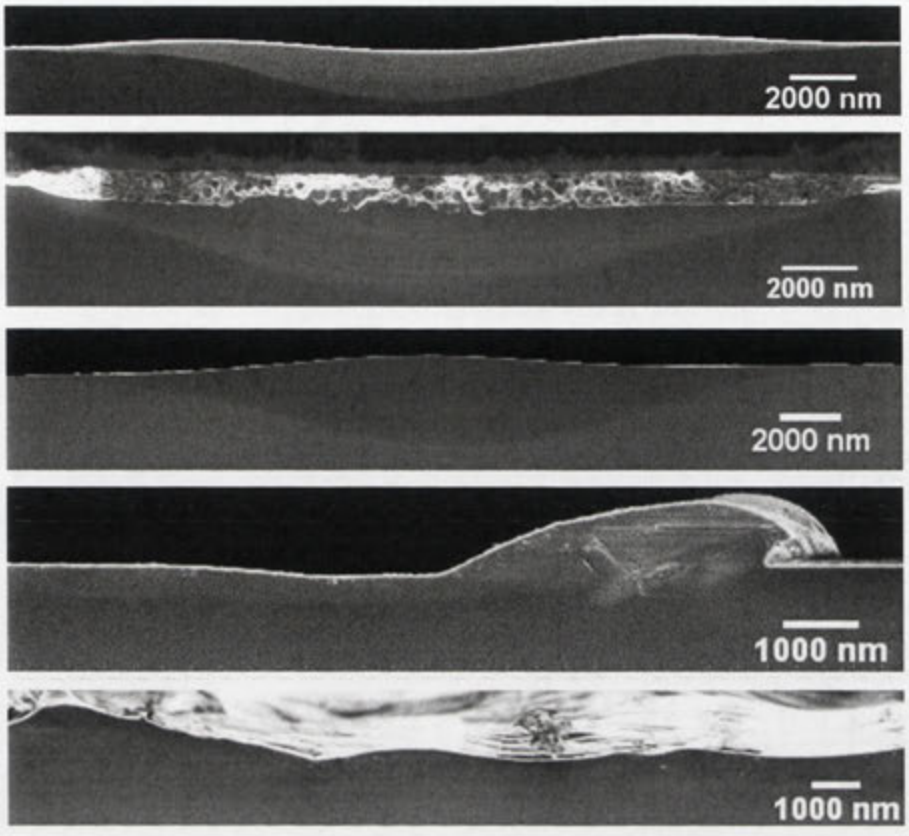

Fig. 22 Dopant contrast observed for samples processed with different laser systems using different dopant sources: (a) B-SOD by DPSS laser; (b) evaporated Al by DPSS laser; (c) P-SOD by DPSS laser; (d) ALD Al_2O_3 by Excimer laser; (e) phosphoric acid by LCP laser.

The application of SEMDCI to both boron and phosphorus diffused samples with textured surfaces is shown in Fig. 23. Because the surfaces were randomly texture etched, the p-n junctions of these samples are almost impossible to be well detected by SIMS or ECV. In contrast, there is no strict requirement for the surface topography of samples for SEMDCI.

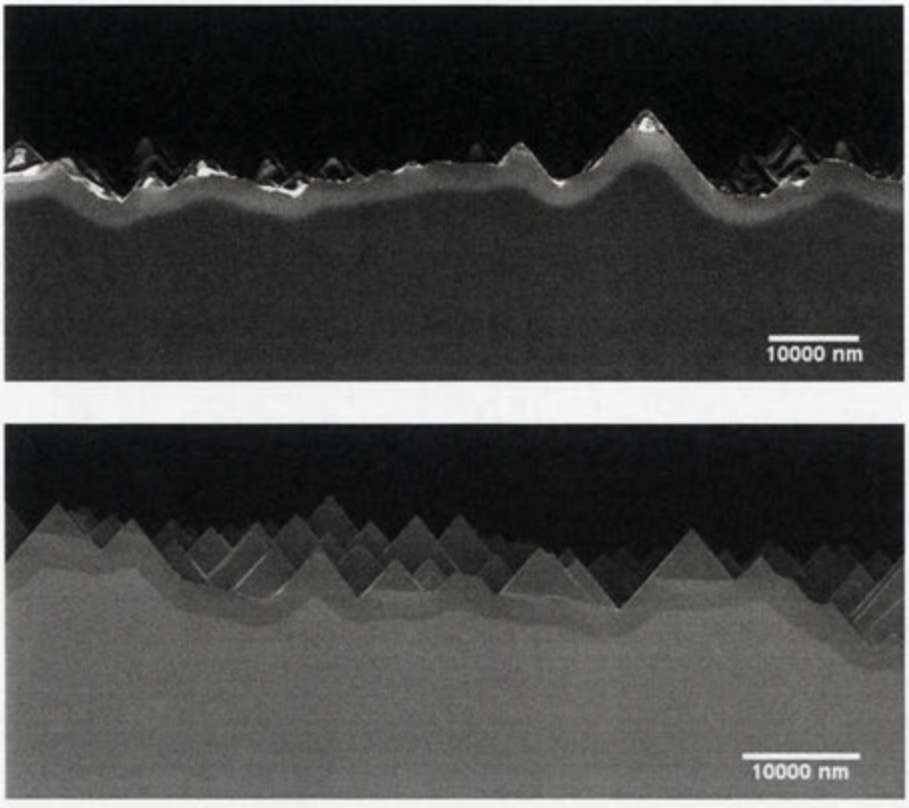

(a)

(b)

Fig. 23 Application of SEMDCI to the delineation of diffused surface regions of textured surfaces: (a) boron diffusion on n-type textured substrate (b) phosphorus diffusion on p-type textured substrate

4.4.3 Conclusion

It is demonstrated that SEMDCI can be used for a large range of different dopant sources and different laser methods, and that good dopant contrast can be obtained under a relatively wide range of microscope parameters.

4.5 Comparison with EBIC

SEMDCI is compared with the widely used EBIC method in this section to evaluate the reliability and accuracy of the SEMDCI method. The comparison also highlights the advantages and the limitations of each of the techniques, so better use of them can be made.

4.5.1 EBIC review

As the laser-doped junction depth and shape have a crucial impact on the performance of the solar cell, a method to measure them is required. A widely used method for this purpose is the EBIC technique [17,194], which is based on collection of electrons in vicinity of the junction. When an electron beam, such as that in a SEM, strikes a semiconductor sample, it generates electron-hole pairs within the beam's interaction volume. If the sample contains a p-n junction and contacts, electron-hole pairs generated within a diffusion length from the junction may be collected, producing an electron beam induced current. In this case, the collected signal indicates the p-n junction location and can be superimposed on the SEM data to create an image. One of the main drawbacks of the EBIC technique is that it depends on the recombination rate at the surface where the beam impinges [195]. Another main limitation is that it only provides information on the location of the p-n junction but not on the dopant density profile. In addition, in most cases EBIC requires significant sample preparation, as well as electrical contacting in the microscope.

4.5.2 Experimental

B-SOD/P-SOD solutions, commercially available from Filmtronics Inc., were used as dopant sources. Single-side polished wafers with opposite dopant type to the spin-on-dopant (SOD) solution were chosen as substrates (see Table 4 for further details on the samples). Laser doping was achieved using a DPSS laser operated in a pulsed mode with a repetition rate of 40 kHz. The spatial overlap between consecutive laser pulses was controlled by variation of the laser scanning speed. In SEMDCI, the p-n junction boundary of an n-type doped surface region is influenced by the p-type bulk doping concentration [180,181,186,196,197]. Therefore, both moderately and highly doped p-type substrates were used for the P-SOD samples. Samples were divided into three groups according to the substrate polarity and resistivity. Within

each group, three different scanning speeds were used (20 laser-doped lines at each speed). In order to perform an accurate comparison between SEMDCI and EBIC, the laser-doped lines were cleaved into two parts, one for SEMDCI and one for EBIC. In this way a direct comparison between the two sides of the same cross-section was possible. Since a freshly cleaved surface is preferred for SEMDCI, the SEMDCI measurements were performed immediately after cleaving. From each group of lines, 2-3 cross-sections with a good SEMDCI signal were chosen for further investigation by EBIC. The sample structure is shown in Fig. 24. The SEM equipment used for SEMDCI is a Zeiss UltraPlus FESEM located at the Centre for Advanced Microscopy, Australian National University, while the EBIC measurements were done using a DISS 5 EBIC from Point Electronic installed on a Zeiss Auriga 39-35 SEM at the Solar Energy Research Institute of Singapore (SERIS).

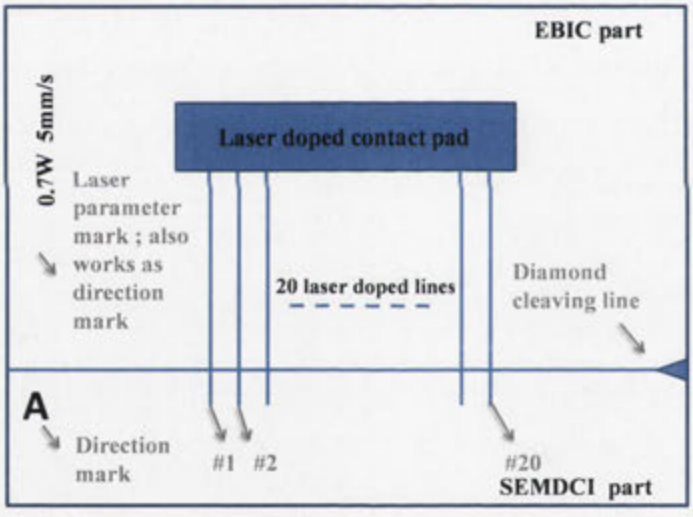

Fig. 24 The sample structure for the comparison of SEMDCI and EBIC

Table 4 Sample details

Sample ID	Substrate type	Substrate resistivity (Ω·cm)	Laser Power (W)	Laser scan speed (mm/s)	SEMDCI detectability	EBIC detectability
A1	P/Boron	1~10	0.7	5	Yes	Yes
A2	P/Boron	1~10	0.7	40	Yes (but very weak)	No
A3	P/Boron	1~10	0.9	200	Yes (weak)[1]	Yes[2]
B1	P/Boron	0.01~0.05	0.7	5	Yes	Yes
B2	P/Boron	0.01~0.05	0.7	40	Yes	No
B3	P/Boron	0.01~0.05	0.9	200	Yes	Yes[2]
C1	N/Phosphorus	1~10	0.7	5	Yes	Yes
C2	N/Phosphorus	1~10	0.6	20	Yes	Yes
C3	N/Phosphorus	1~10	0.9	150	Yes	Yes

[1] A few lines were not detectable or the signals were too weak.

[2] Only some lines were detectable. Different cross-sections were used for the comparison.

4.5.3 Results and discussion

4.5.3.1 Detectability

For each sample group, laser parameters and the detectability of the SEMDCI and the EBIC signals are listed in Table 4. As can be seen, with the exception of Sample A2 which was processed at low laser power and high scanning speed, the detected SEMDCI contrast was sufficient to allow characterization with a reasonable signal to noise ratio. In contrast, several of the laser-doped lines could not be characterized by EBIC. As EBIC requires a good electrical contact between the imaged area and the contact pad, samples with lowly doped lines or samples with discontinuous doping are not always suitable for EBIC measurement. Although this problem can be solved by metallization of the doped line, this requires additional preparation, which complicates the sample preparation. As a contactless characterization method, SEMDCI has an advantage over EBIC in this respect.

4.5.3.2 Agreement between the methods

Figure 25(a) is a representative example of a sample with good SEMDCI and EBIC

signals. It demonstrates good agreement between SEMDCI and EBIC in terms of the shape of the p-n junction boundary. Similar agreement was observed for most of the samples. These agreements indicate that SEMDCI can be used as a reliable technique for characterising the p-n junction, similar to the well-established EBIC method. Moreover, as shown in Fig. 25(b), a high contrast signal in SEMDCI likely corresponds to a high signal intensity in EBIC (compare the middle circled region in Fig. 25(b) with the two edge circled regions). This relationship is possible if the electric field effect is taken into consideration. A possible mechanism of SEMDCI is the patch field effect caused by energy band bending. As discussed in Section 4.3.1, the stronger the patch field the higher the contrast observed in SEMDCI. The patch field strength is basically proportional to the built-in electric field of the p-n junction [179,186]. Therefore, if there is a strong built-in electric field within the depletion region of the p-n junction that normally produces a high intensity EBIC signal, a corresponding strong patch field will result in a high contrast in SEMDCI. However, the signal generated by the EBIC technique is not only related to the electric field of the depletion region but also the surface recombination and bulk lifetime, which might partially explain the disagreement between SEMDCI contrast and EBIC signal intensity within the middle circled region in Fig. 25 (b).

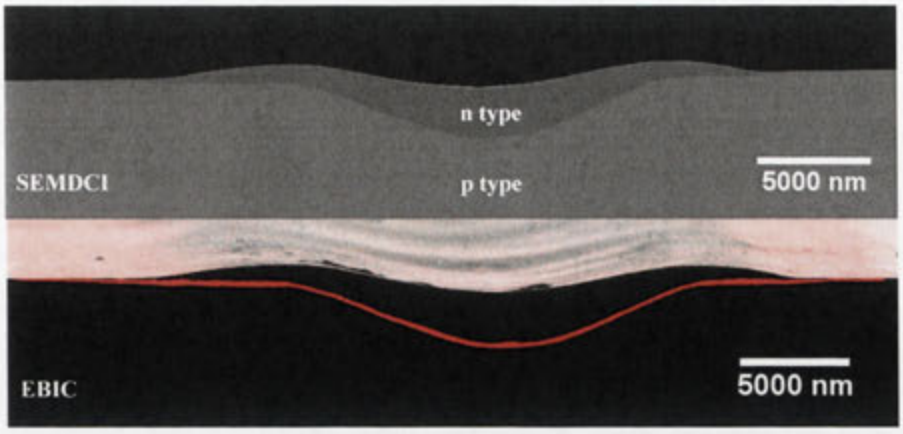

(a)

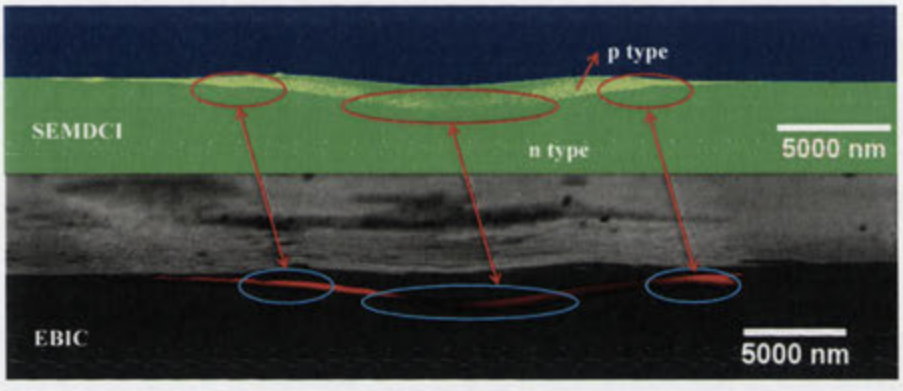

(b)

Fig. 25 (a) SEMDCI and EBIC images of Sample B1. The good agreement between the two images regarding the shape of the p-n junction is evident; (2) SEMDCI and EBIC images of Sample C2.

4.5.3.3 Resolution and Sensitivity

An example of the challenges associated with non-uniform and discontinuous doping distribution is presented in Fig. 26(a). Due to the high energy pulse used for this sample, a poor electrical contact was formed. The EBIC signal was detected only from one line. Unfortunately it was not possible to characterize this line by SEMDCI. Therefore a direct comparison of the same cross-section is not available for this sample. However comparison between similar lines of the same sample still provides valuable insights. Fig. 26(a) demonstrates the ability of both SEMDCI and EBIC to image a

rough, complicated, non-uniform and discontinuously doped region. Given the high spatial resolution of the EBIC technique evident in Fig. 26(a), the apparent disagreement between SEMDCI and EBIC images for some samples regarding the uniformity of doped regions, as illustrated in Fig. 26(b), is likely explained by the different sensitivity of the two techniques. In particular, the dark regions within the lightly coloured p doped regions visible in the SEMDCI image would at first glance appear to suggest that these regions are not p doped but are instead n doped with similar doping concentration to the substrate. However, contrast in SEMDCI is often only observed when the p dopant concentration exceeds a few 10^{17} cm^{-3} [196]. Thus, the darker regions may instead be lightly doped p-type, an interpretation that is supported by the EBIC image. Whether this lack of contrast at low doping concentrations is significant or not will depend on the particular application, but the limitations must always be kept in mind. In addition, by inspecting the edge of the laser-doped region as circled in Fig. 26(b), it can be found that the EBIC signal has a sharp top edge that basically agrees with the p-n junction location imaged by SEMDCI. However, the main part of the EBIC signal width extends into the lowly doped bulk with a blurry bottom edge. This is believed to be caused by two following reasons. Firstly, the built-in electric field of the depletion region distributes mainly within the lowly doped region, therefore resulting in more EBIC signal from the bulk. Secondly, during SEM electron beam scanning, if the carrier diffusion length is long, the carrier pairs generated close to but not in the depletion region are possible to flow into the depletion region. They are then accelerated by the built-in electric field there to form a measurable current. Because the lightly doped bulk normally has fewer defects compared to the highly doped laser doping region, the excess carriers generated in the bulk have longer diffusion length leading to a higher possibility to flow to depletion region and to generate EBIC signal.

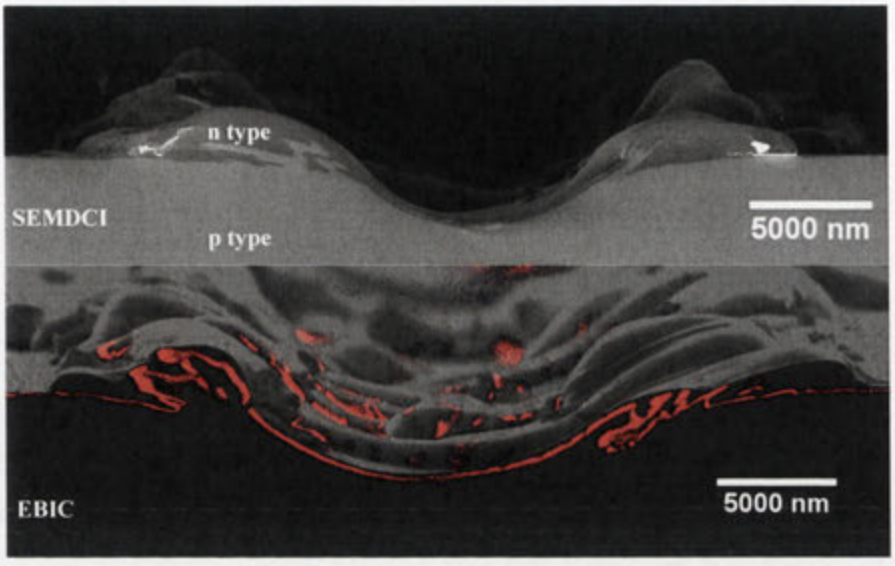

(a)

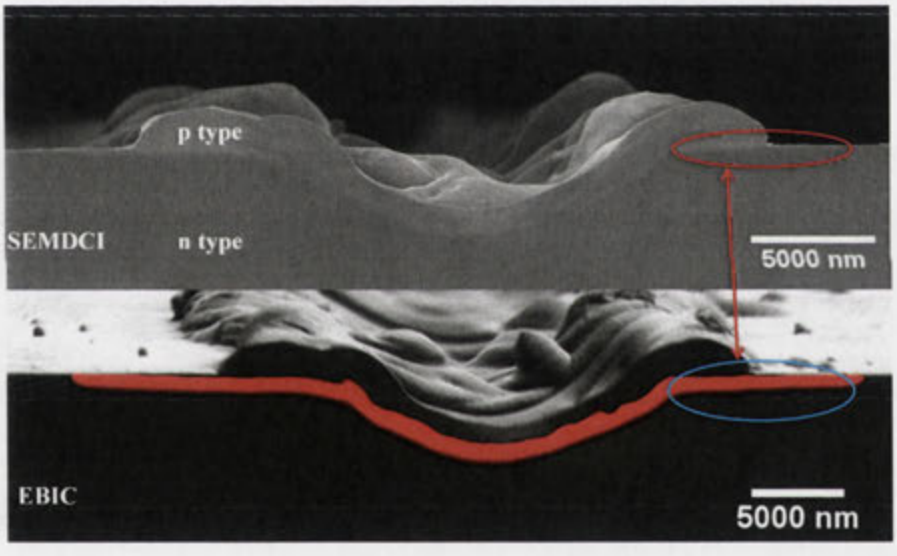

(b)

Fig. 26 (a) SEMDCI and EBIC images of Sample B3; (b) SEMDCI and EBIC images of Sample C3.

4.5.3.4 Quantitative analysis difficulty and error

As the SEMDCI and EBIC images were taken using different equipment in different institutes, there are unavoidable differences between the SEMDCI and EBIC images,

for example the sample tilt angle which is nearly impossible to be accurately recorded since samples are manually loaded into the sample holder. Therefore, it is difficult to do an aligned 2D comparison. However, 1D information such as maximum doped region width can still be extracted from the images for a comparison.

Fig. 27 shows the maximum doped region widths and the dimensions of some obvious topographical features (such as the laser induced surface lump as shown in Fig. 26(b)) extracted from SEMDCI and EBIC images where the same cross-section comparison is available (note that there is no measurable topographical feature for the very smooth Samples C1 and C2). The results are shown in the form of the ratio between the EBIC and the SEMDCI data. It was found that the maximum doped region widths obtained from EBIC are wider than those of SEMDCI. This finding can be explained by system error and difference in the sensitivity of the two techniques. Firstly, the system error was evaluated by measurement of the dimensions of some obvious topographical features. It was found that the measurements from the EBIC system consistently produced larger values. This disagreement is likely caused by the different working distances used for the SEMDCI and EBIC. The longer working distance which was used for EBIC might causes image distortion, especially near the image edges. It was found that this systematic error is similar for all the tested images and can be easily corrected by using a correction factor. The modified maximum doped region width ratio after this correction is also plotted in Fig. 27. It was found that this systematic error contributes around half of the measured difference between SEMDCI and EBIC. Therefore the sensitivity difference between the systems can then be estimated to be ~10 %.

It is worth mentioning that although EBIC has higher sensitivity and usually detects deeper/wider junctions compared to SEMDCI, this effect can be partially compensated by the depletion region effect [180,181,186,196,197] of SEMDCI. As n-type and depletion regions both appear dark in the SEMDCI image, if the substrate is lowly doped (such as Sample A1), the depletion region extends mainly into the p-type region

so the p-n junction outline shown by SEMDCI image is deeper than the actual position. This might partially explain the low corrected ratio of Sample A1.

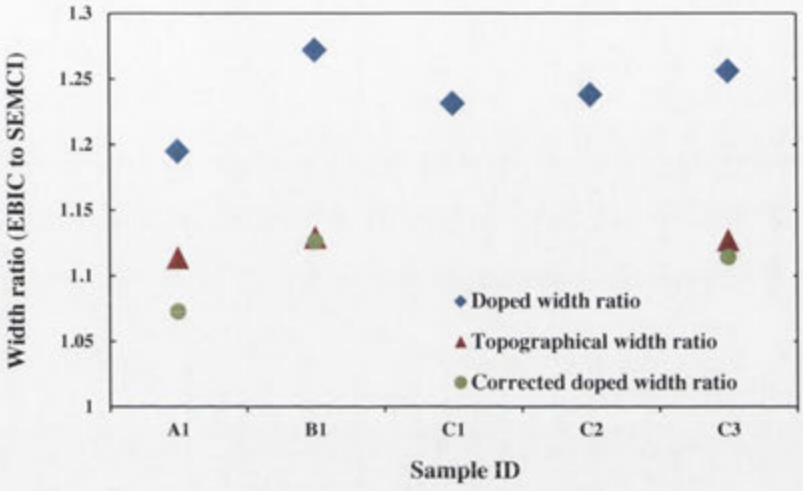

Fig. 27 Comparison between data measured by SEMDCI and EBIC including the maximum doped region width, the size of topographical features and the corrected maximum doped region width after taking into account the systematic error (see text). The results are shown in the form of a ratio between the EBIC and SEMDCI data. No obvious measurable topographical feature was found on Samples C1 and C2.

4.5.4 Conclusion

EBIC is a well-established and widely used characterization method for laser doping to display the p-n junction position, while SEMDCI is a technique that may provide a faster, easier and cheaper measurement. The two techniques were compared qualitatively and quantitatively for laser doping applications. The good agreement demonstrated between of the two methods in terms of p-n junction shape indicates that SEMDCI can be used as a reliable technique for characterising laser-doped p-n junction. Both techniques were shown to be able to detect a complicated, non-uniform and discontinuous doped region. It was found that EBIC provides a better detection sensitivity regarding the doping concentration than SEMDCI, while SEMDCI requires less and easier sample preparation. The comparison highlights the advantages and the

limitations of each of the techniques.

4.6 Quantitative dopant density measurements based on SEMDCI

The properties of SEMDCI that were not fully investigated in previous contributions, such as the sensitivity of the contrast to the doping concentration for differently doped substrates, and the influence of the doping depth scale on the relationship between contrast and concentration, are studied and discussed.

4.6.1 Experimental

Silicon (100) wafers of varying resistivities were used. For n-type laser doped or diffused samples, p-type substrates were used and vice versa. Wafers were single side polished or saw-damaged etched prior to processing. Boron and phosphorus diffusion samples were prepared for comparison with laser doped samples. The doping profiles of the diffused samples were determined by electrochemical capacitance-voltage (ECV) measurements using a CVP21 Wafer Profiler system by WEP to establish the quantitative relationship between image contrast and dopant density. B-SOD solutions, available commercially from Filmtronics Inc., were used as dopant sources of laser doping. Laser doping was achieved using a DPSS laser, operated in pulsed mode and scanned across the target at different speeds so as to vary pulse distance. All samples used for quantitative measurements were cleaved just before loading into the FESEM.

4.6.2 Quantitative dopant density calibration through diffused samples

The requirements for SEMDCI to be suitable for quantitative analysis are:

1) A unique and monotonic relationship between contrast and doping concentration.

2) A good sensitivity of contrast to doping concentration. A situation where the contrast varies with the logarithm of the doping concentration is generally desirable as it potentially allows dopant imaging over several orders of magnitude of dopant concentration.
3) A relative insensitivity of the dopant concentration-contrast variation to other factors such as slight changes in the microscope parameters, substrate doping etc. It would be most convenient if it was possible to determine a relationship that is independent of factors such as WD, AV etc. However, this is unlikely to be the case. An alternative is to use a set of calibration samples with known dopant density profiles. Images taken of these samples under a specific set of conditions then allow the determination of the relationship for that set of conditions.

Diffusion profiles determined using ECV measurements was used in an attempt to establish the relationships between contrast and doping concentration. The contrast of SEI is defined as follows [186,192,193]:

$$C_p = 100 \times \frac{I_x - I_{sub}}{I_x + I_{sub}}, \tag{4-2}$$

$$C_n = -100 \times \frac{I_x - I_{sub}}{I_x + I_{sub}}, \tag{4-3}$$

where C_p (C_n) is the contrast of the p (n) laser-doped or diffused regions, I_x represents the unknown intensity level and I_{sub} represents the substrate average intensity level. For the data shown from Fig. 28 to Fig. 30 below, all the curves in each figure were obtained under the same SEI settings, including AV, WD, aperture and artificial brightness and contrast settings, unless specifically noted. As can be seen from Fig. 28, ECV and SEMDCI show reasonable agreement for the position of the p-n junction and also a monotonic relationship between dopant concentration and contrast, except for the region close to surface where the edge effect caused by the fact that electrons preferentially flow to and are emitted from edges and peaks makes the relationship

difficult to establish [113]. It can be noted that the dopant contrast curve for the boron diffused sample indicates a shallower p-n junction than the corresponding ECV profile, while for the phosphorus diffused sample the situation is reversed. One possible reason is that, as previously noted [180,181,186,197], the n-type region and depletion region both appear dark in SEI.

As shown in Fig. 28, the substrate doping concentration has a significant impact on the observed contrast. A similar phenomenon has been reported by Venables *et al.*, although these authors only reported the situation of p-type doping on n-type substrates [181]. The changes of dopant contrast with the change of substrate doping level observed here are also different from those observed in [181]. In [181], for p-type diffusions on n-type substrates, a higher substrate doping resulted in a reduced sensitivity of the contrast to the doping level for high doping concentrations. In contrast, as shown in Fig. 29, for the p-type diffusion, the sample with the highest substrate doping investigated here shows the highest sensitivity for high doping concentrations but the lowest sensitivity for low doping concentrations. Although the substrate doping plays an important role in the sensitivity for low or high doping concentrations, the sensitivity for moderate concentrations (between 3.0×10^{18} to 3.0×10^{19} cm^{-3} for the investigated samples) is roughly independent on the substrate doping. Therefore, variable substrate doping can be regarded as a factor that limits the applicable concentration measurement range of SEMDCI. The observation that contrast sensitivity changes with substrate doping cannot be explained by a variation in I_{sub} with different substrate doping, since if there was only a variation in I_{sub} then the qualitative relationship between doping and contrast would be maintained. This is true since for all the cases investigated here; the denominator in the Eq. (4-2) or (4-3) does not vary significantly for a given profile as the contrast value never exceeds 20 %, so to a first order the contrast is proportional to the numerator. More detailed analysis of the data also confirms this. Further work is needed to determine the reasons for the observed dependence of dopant contrast on substrate doping. However, it is clear that

accurate quantitative analysis requires the use of substrates with the same and appropriately chosen doping concentration.

For n-type diffusions, as shown in Fig. 28 (b), the use of lowly doped substrates results in higher dopant sensitivity, but the observed relationship between doping and contrast is unlikely to be suitable for quantitative imaging. For very high substrate doping, on the other hand, the sensitivity to changes in doping is rather low, but the sharp reduction in contrast at the p-n junction makes this substrate type very suitable for qualitative imaging and p-n junction delineation. Therefore, in this study, n-type doped samples are not included in quantitative analysis.

As mentioned above, a key requirement for quantitative imaging is the existence of a unique relationship between contrast and dopant density under same SEI setting and substrate. In order to investigate this, samples were prepared using identical substrates but with diffusion profiles of different depths. These were then analyzed using identical SEI settings. It can be seen from Fig. 30 that the two curves corresponding to different diffusion profiles show reasonable agreement, but the agreement is worse for low doping concentrations. One significant contributing factor to the discrepancy is the error in the depth scale, perhaps for both the SEI contrast and the ECV profile, but certainly for the latter. In a region where the doping concentration changes rapidly, even a slight difference in the depth scales will lead to a large error in the established relationship. In conclusion, for p-type samples, a quantitative relationship has been established, albeit over a limited range of dopant concentrations and with still considerable error.

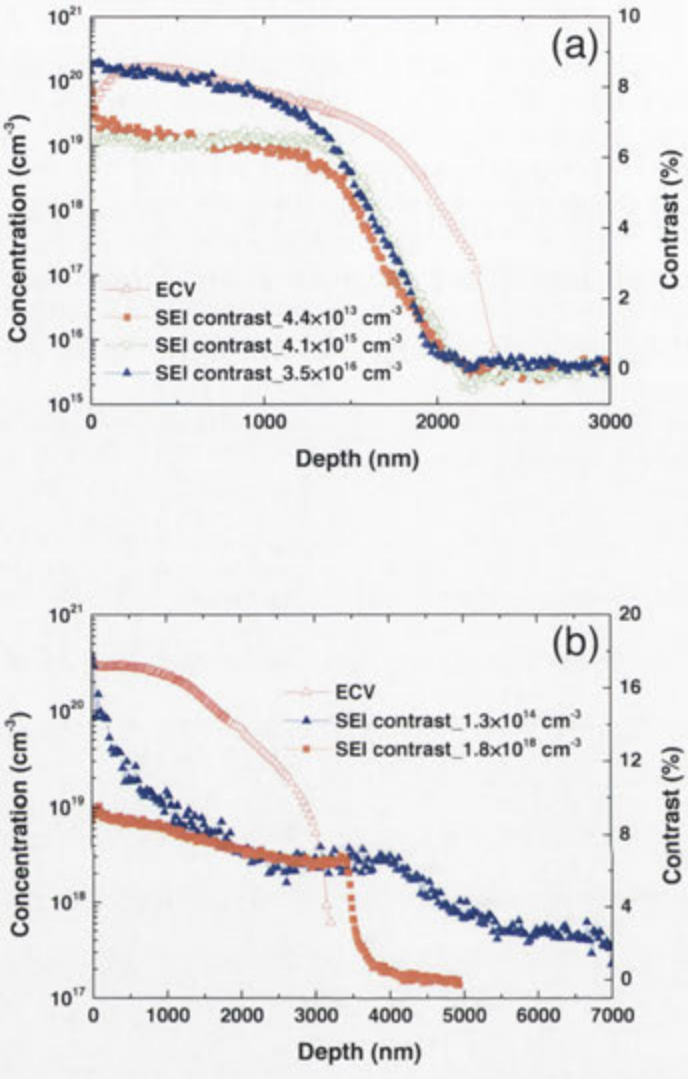

Fig. 28 Impact of substrate doping on SEI contrast: (a) boron diffused samples on n-type substrates with different substrate doping concentrations; (b) phosphorus diffused samples on p-type substrates with different substrate doping concentrations.

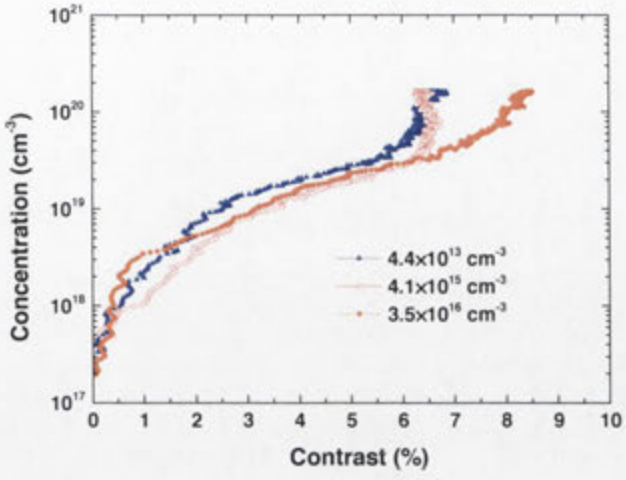

Fig. 29 Dopant concentration as a function of SEI contrast for p-type diffusions on n-type substrates with different substrate doping concentrations based on the data shown in Fig. 28(a)

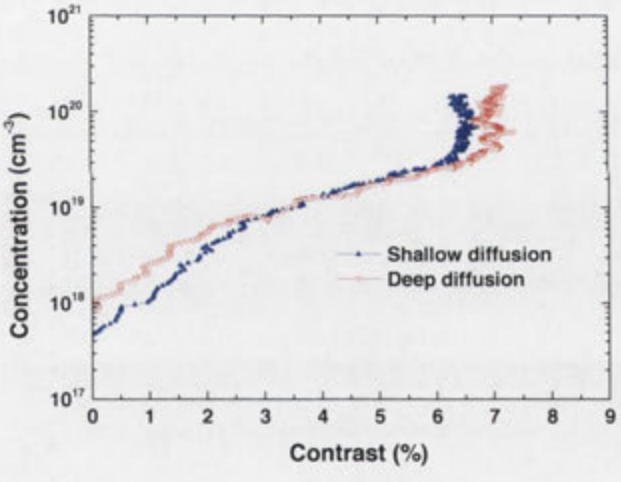

Fig. 30 Dopant concentration as a function of SEI contrast for two different boron diffusion profiles on n-type substrates (4.1×10^{15} cm^{-3})

4.6.3 Quantitative dopant density of the laser-doped cross-section

In this section, the application of the SEMDCI technique to laser doped samples is illustrated. Dopant contrast images were converted to 2D dopant concentration colour

maps based on the quantitative relationship established in Section 4.6.2, as shown in Fig. 31. The microscope parameters were the same as those used to establish the relationship in Fig. 29. Different laser parameters were used to create a series of lines on the same sample, thus allowing quick and reliable comparison. The laser-doped lines on the same wafer were analysed using the transfer length method (TLM) to determine the line resistance R_L (Ω/cm) for each line. In addition, quantitative SEMDCI was performed to determine the cross sectional dopant concentration profile and hence the estimated line resistance, assuming the mobility of single crystal silicon and using the mobility model of Masetti [142]. The comparison of the values of R_L determined using the two methods is shown in Fig. 32. TLM is a reliable and accurate method to measure the line resistance of laser-doped lines, as discussed in Section 3.2.2, and can be regarded as a good reference to test and verify SEMDCI results. Note that to ensure accurate TLM measurements, low resistivity substrates (4.43×10^{13} cm^{-3}) were used here even though this type of substrate does not display the optimal dopant density-contrast relationship, as discussed in Section 4.6.2.

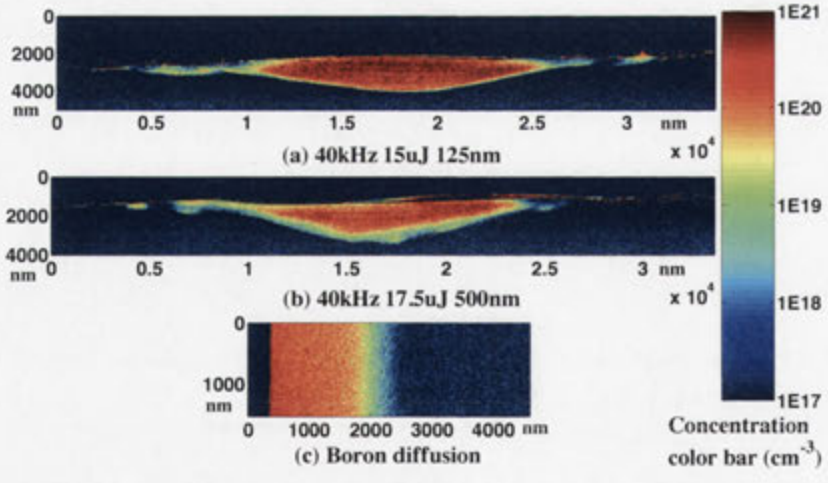

Fig. 31. 2D dopant concentration colour map image of laser-doped samples produced with a DPSS laser at 40 kHz using a boron spin-on dopant and a lightly doped n-type substrate (N=4.4×10^{13} cm^{-3}). (a) 15 μJ, 125 nm; (b) 17.5 μJ, 500 nm; (c) Boron diffusion into the same substrate (see Fig. 28 for the corresponding profiles).

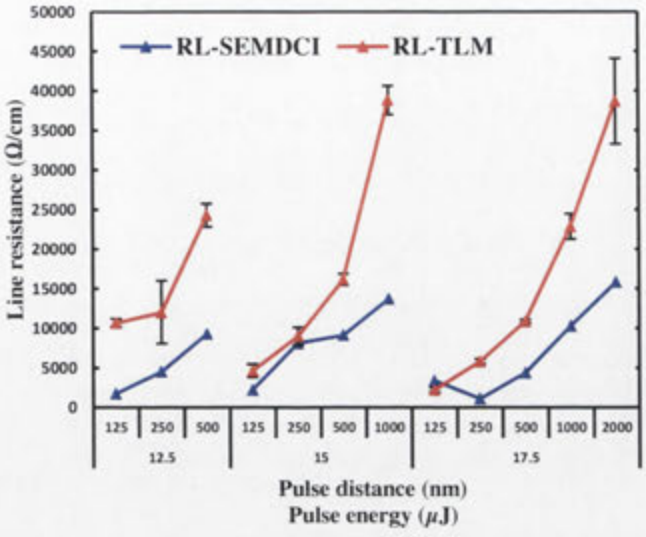

Fig. 32 Comparison of line resistance (R_L) obtained from TLM and SEMDCI.

Figure 31 reveals that the incorporation of dopant in laser-doped samples is not always homogeneous and laser parameters have a significant impact on the dopant distribution. The sample processed at pulse energy of 17.5 μJ and pulse distance of 500 nm in particular can be seen to be inhomogeneous compared to the 15 μJ-125 nm sample. This would be expected to impact on the electronic quality of the doped region in a solar cell, potentially resulting in poor electrical contact and/or increased recombination at the metallized surface.

From Fig. 32, it can be seen that the trend in the line resistance R_L determined by SEMDCI shows qualitative agreement with the line resistance values measured by TLM. However, the absolute R_L values obtained from SEMDCI often depart significantly from those determined by TLM. In particular, it is apparent that the line resistance determined from SEMDCI appears to underestimate the actual line resistance in most cases. There are several possible reasons that could explain the observed discrepancy. Firstly, the mathematical fitting used to establish a quantitative relationship between SEMDCI contrast and dopant concentration causes an inherent error, especially considering that for the sample substrate used here, dopant contrast is

relatively insensitive to doping for highly doped regions as discussed above. Secondly, the cross sections along a laser-doped line are not uniform in most cases. For some laser parameters, a few but not many small ablation spots can be found along the same laser-doped line. Even for optimum laser parameters, because of variations in the sample, there are a few relatively poor laser-doped regions along a good laser-doped line. This non-uniformity cannot be properly reflected in SEMDCI, because SEMDCI only records one cross-section of a laser-doped line and the cross sections used here are of "good" regions. Therefore, SEMDCI will underestimate the line resistance. Thirdly, the edge effect phenomenon will lead to an overestimation of doping near the sample surface, which could at least partly explain why the R_L values from SEMDCI are systematically lower than that from TLM. In conclusion, SEMDCI provides very useful information about the 2D dopant distribution of laser doped regions. SEMDCI also potentially offers a faster and easier way to measure the line resistance of laser doping line compared to using other methods albeit still with considerable error. Other line resistance characterization methods such as TLM normally involve significant sample preparation and measurement effort.

4.6.4 Conclusion

The substrate doping level was shown to have a significant impact on the relationship between dopant density and image contrast, suggesting that substrate doping should be carefully chosen for accurate results. The impact of substrate doping on the relationship between dopant concentration and contrast was found to be different from that previously reported [181], and therefore should be established independently for each microscope setup. However, importantly, the relationship between contrast and dopant concentration appears to be independent of substrate doping profile for medium doping level.

2D dopant distribution images of laser doped regions were created using the established relationship between doping and contrast from diffused samples of the

same substrate resistivity. Lines resistance values determined from TLM and SEMDCI images were compared for the first time.

4.7 Interaction between different materials during the laser doping process

Because SEMDCI not only shows the doping contrast but also all the topographic details that SEI can provide, it is useful to use SEMDCI to observe the tilted cross-section of laser-doped lines with the dopant precursor and dielectrics on the top surface. In this way, some interactions between the different materials during the laser doping process can be revealed.

4.7.1 Literature review

A short review of the laser-induced dielectric ablation (limited to SiN_x and SiO_2 here; same mechanisms might be applicable to other dielectrics) from the silicon surface and the doping mechanism through SOD is given below to provide the context for subsequent discussions.

4.7.1.1 Laser-induced dielectric ablation

The mechanism of laser-induced dielectric ablation (in the case there is no other coating on top) from the silicon surface can be classified into three categories based on where the laser light is absorbed [198-200]:

Direct ablation:

In this category, the laser light is mainly absorbed in the dielectric layer itself. The dielectric layer is then heated and removed as a result of melting and vaporization. In the case where a Gaussian laser beam is used, the ablation results in a Gaussian-like crater opening with a gradual variation of the thickness from the centre to the edge.

This type of ablation normally happens when using a laser with short wavelengths such as a UV laser.

Indirect ablation:

If the laser is mainly absorbed in the silicon and the dielectric layer can be regarded as transparent to the wavelength of the laser light, the silicon melts or evaporates locally and lifts off the dielectric layer on top of it mechanically. The lift-off process is either caused by the different thermal expansion coefficients between the melted silicon and the dielectric layer at low laser pulse energy, or because of the increasing vapour pressure of the generated plasma at the silicon-dielectric interface at high laser pulse energy. Indirect ablation normally results in a dielectric-opening with a sharp edge.

Although in the indirect ablation case the dielectric film can still be heated up by thermal conduction, a phase change of the dielectric is not considered, because most commonly used dielectrics, for example SiO_2 (1970 K [201]) and SiN_x (2150 K [202]), have higher melting points than silicon (1687 K [49]).

Combination ablation:

If the laser is absorbed by both the dielectric layer and the silicon, direct and indirect ablation take place simultaneously.

4.7.1.2 Doping through SOD

SOD has been widely used as a dopant source for both furnace diffusion and laser doping, because a uniform dopant-rich layer can be simply and quickly produced using this technique. SOD can be divided into two main categories: silicate based compounds and dopant-organic compounds [203].

The silicate SOD is produced by a condensation reaction of $Si(OH)_4$ by losing water and by adding dopants into the Si-O network. Most phosphorus SODs belong to this category. After spin deposition at room temperature and baking at low temperature,

polymer cross-linking occurs and a porous SOD structure is formed as a result of the solvent evaporation. When employing this SOD in furnace diffusion, the impurities are driven into the silicon [203].

The dopant-organic compound SOD is mainly used to produce boron SOD. This boron SOD is based on a boron-nitrogen backbone polymer dissolved in organic solvent. After spin deposition and baking, most of the organic solvent evaporates resulting in a porous SOD layer. At diffusion temperature, the B-N bonds are broken by the existing oxygen in the SOD layer or the ambient, producing B_2O_3 which then reacts with the silicon to enable the diffusion of Boron atoms [203].

4.7.1.3 Laser doping through SOD coated dielectric films

The discussion in above two sections is based on the scenario where there is either only the dielectric film or only the SOD present. The SOD doping mechanism discussed above applied for furnace diffusions where the temperature is below the silicon melting point.

For the one-step laser doping process where the SOD is applied on top of the dielectric film, the situation is rather more complicated. The laser pulse energy used for laser doping is high. The local temperature can continue to increase after melting the silicon and possibly reach the melting (even evaporation) points of both the dielectric film and the SOD.

To the knowledge of the author, there is no any publication about what happens exactly between the SOD, the dielectric film and the silicon during the laser doping process. The application of SEMDCI, as shown below, cannot fully explain the process, since it records only the start and the end of this process. However, useful information can still be drawn out.

4.7.2 Experimental

n-type <100> 1-5 Ω.cm wafers were used. After a tetramethylammonium hydroxide (TMAH) surface etch, ~90 nm SiN_x was deposited via plasma-enhanced chemical vapor deposition (PECVD). B-SOD solutions, available commercially from Filmtronics Inc., were applied on top of the SiN_x film as the dopant precursor. More specifically, the B-SOD was applied at 2000 rpm spin-speed and at 400 rpm/second spin-acceleration for 50 seconds. After spin-coating, the samples were backed at 120 ^oC for 20 minutes. The SEMDCI of a tilted cross-section of a non-laser-processed region is shown in Fig. 33. All groups were then processed on the side with the dielectric and SOD using a PyroFlex^{TM} 25 laser system at a wavelength of 532 nm and a frequency of 20 kHz. The laser pulses had approximately Gaussian temporal and spatial beam profiles. The $1/e^2$ Gaussian radius of the focused laser beam used is 9.8 μm, which was measured by the method of Kiang and Lang [204]. The laser is operated in pulsed mode and scanned across the target at different speeds so as to vary the pulse distance. Different sets of pulse durations, pulse energies and pulse distances were used. The chosen sets of laser parameters were pre-tested via 4PP laser-doped box method (see Section 3.2.1) to be able to produce reasonable sheet resistances. In order to distinguish between the effects of the laser overlapping in one or two directions, both lines (1D) and areas (2D) are produced. A 1D line is formed by laser scanning in only one direction (referred to as the y direction in this study) and is perpendicular to the observed cross-section in SEMDCI. A 2D area consists of multiple 1D lines (1 to 4 lines) produced by shifting 1D lines in the x direction (parallel to the cross-section) with a constant interval distance (4μm in this study). A sample includes many patterns. The structure of a pattern is illustrated in Fig. 34. In this figure, only the case of a 2D area consisting of 4 1D lines is shown, but in experiment, the number of the 1D lines can be from 1 to 4.

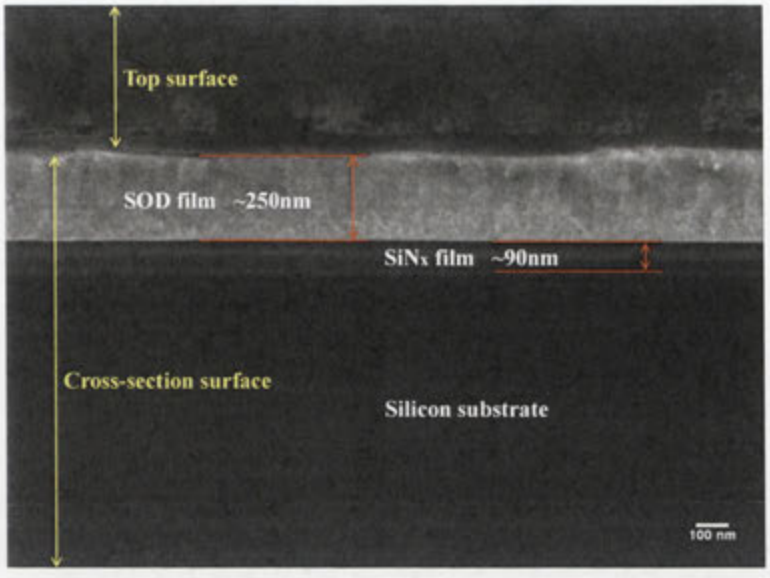

Fig. 33 A tilted cross-section of a non-laser-processed region with SOD and SiN_x on top surface.

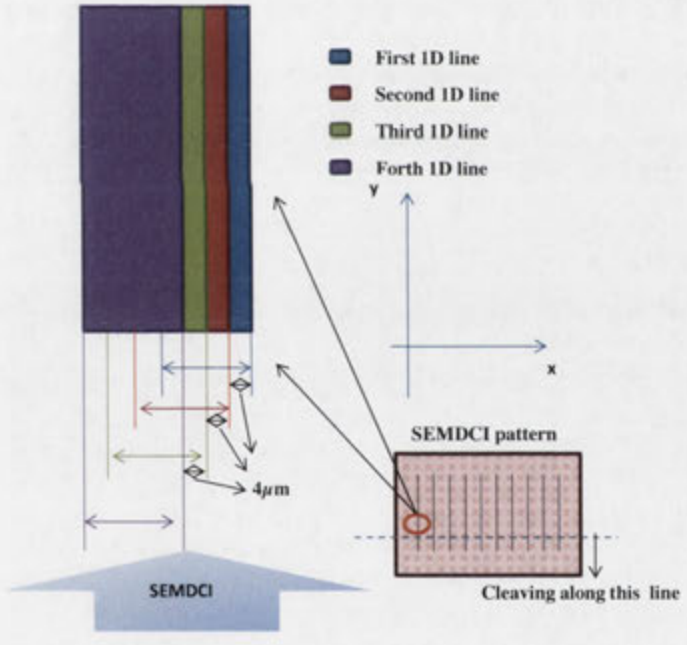

Fig. 34 Illustration of an experimental pattern. The width of each line was the same, but only the full width of the fourth line can be displayed in the figure, since subsequent lines were always shifted by 4μm in the x direction relative to the previous line.

4.7.3 Results and discussion

4.7.3.1 Single 1D line

Firstly, I focus on the case of a 1D line. In this way, only the y direction laser pulse overlapping needs to be considered. Two representative cross-sections are shown in Fig. 35. A high magnification image of the right edge of the Fig. 35 (a) is shown in Fig. 36.

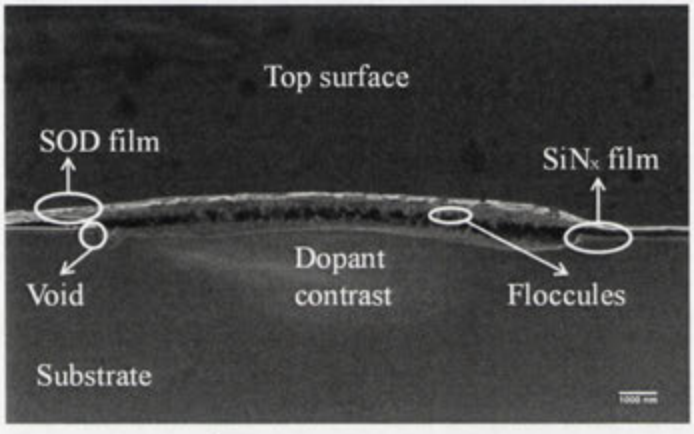

(a) 20kHz-50ns-2.5μJ-0.25μm

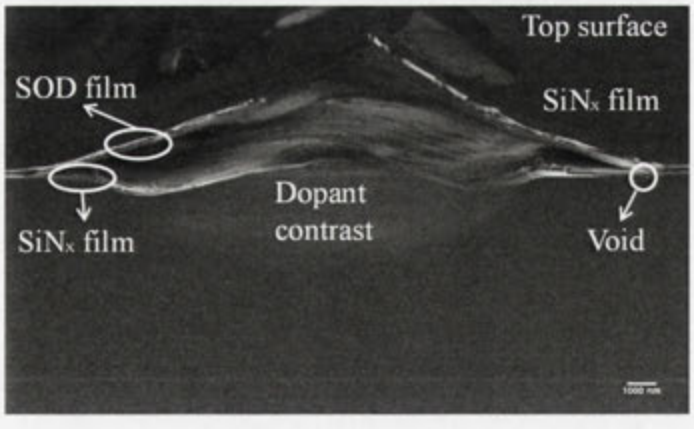

(b) 20kHz-220ns-11μJ-0.5μm

Fig. 35 Observation of the two representative cross-sections: (a) processed at 20 kHz using a pulse duration of 50 ns, a pulse energy of 2.5 μJ and a pulse distance of 0.25 μm; (b) processed at 20 kHz using a pulse duration of 220 ns, a pulse energy of 11 μJ and a pulse distance of 0.5 μm.

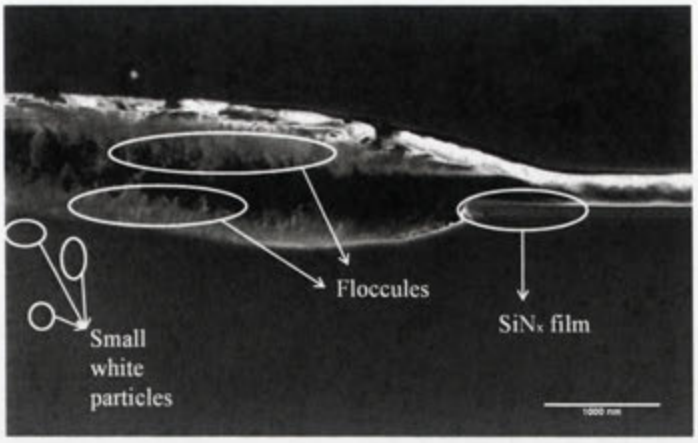

Fig. 36 A high magnification image of the right edge of Fig. 35 (a).

From Fig. 35 and Fig. 36, it can be found:

1) The SOD films can either be slightly warped upwards (Case A) or be cracked roughly along the centre of the line and peeling off (Case B). Case A is observed when the laser pulse energy is low, while Case B happens at high pulse energy, especially when the energy is sufficiently high to heat the silicon above the evaporation threshold.
2) In both cases, doping as deep as around 2μm is achievable.
3) In both cases, the SiN_x film is opened by the laser.
4) In both cases, the SOD top surface (the surface facing the laser) is nearly intact, while the interaction between the silicon and the SOD happens at the back surface of the SOD film. This indicates that the SOD film does not interact significantly with the laser beam. This is supported by spectrophotometer measurements of the SOD film which show negligible optical absorption for wavelengths from 250 to 1200 nm.
5) In both cases, voids in the silicon can be noticed at the edge of the window opened in the dielectric film. Similar defects have been observed by Hameiri *et al.* [63] in dielectric-coated and laser-processed samples after Young's etch. This is likely to be related to the thermal coefficient mismatch between the silicon and the dielectrics [63,205].

6) In Case A, where the SOD film slightly warps upwards, a gap is generated between the SOD film and silicon. Within this gap, on both the back side of the SOD and the silicon surface, there are a large number of floccules. The floccules only form in regions where the SiN_x is removed. At the edges, the SOD is lifted off but the SiN_x remains intact and this doesn't form floccules. It is unknown yet what the floccules exactly are, but they are properly a special form of SOD or SiN_x film residuals.

7) In Case A the SOD film caps the sample surface, so the SiN_x film or its constituent materials will remain within the gap between the SOD and the silicon. One possibility is that the ablated SiN_x film residuals might be part of the observed floccules, which is unlikely as will be discussed later. Another possibility is that the SiN_x film might break up on the melted silicon and subsequently be incorporated into the silicon, or that it is dissolved into the silicon. Evidence for the dissolution of the nitride into the silicon comes from the high measured nitrogen concentrations up to a depth of 0.2 μm in silicon substrates after laser doping through SiN_x films, as measured by SIMS [63]. In this case, the nitrogen might introduce recombination active defects into the silicon as reported in the literature [206,207] and as discussed in Chapter 6, where the samples coated with SiN_x films do show extreme lifetime degradation after laser processing. In addition, if the dielectric film is not completely dissolved into the silicon, it may result in SiN_x precipitates, which could be the origin of the small white particles that can be seen in Fig. 36.

8) The detachment of the SOD film from the substrate shown in Fig. 35 implies that the optical conditions at the interface will change compared to the conditions for the initial surface, when the SOD film is in direct contact with the dielectric film. If subsequent laser pulses irradiate the substrate where part of the SOD film is detached from the silicon surface, the mechanism of incorporation of the dopant source into silicon will be affected both as a result

of changed optical properties and altered conditions for the dopant incorporation.

9) In both cases, the width of the detached SOD film is greater (by several μm) than the width of the opened window in the dielectric film and the doped region. This width difference means there will be no SOD film directly contacting the silicon for the region irradiated by the following pulse unless the pulse distance is larger than this width difference.

4.7.3.2 Overlapping lines

In this section, the work of the previous section is extended to the observation of 2D areas consisting of multiple overlapping 1D lines. Fig. 37 and Fig. 38 show aligned images of overlapping lines using two sets of laser parameters and covering both cases A and B in the previous section. Four images with an increasing number of overlapping lines (from 1 to 4 lines) are shown. The images are aligned to the right edge of the opened window in the dielectric (blue line), while the red lines mark the left edge of the opened windows. Interestingly, the spacing between two adjacent red lines in both Fig. 37 and Fig. 38 varies rather than being constant at 4 μm. This is very likely caused by the different optical conditions for each line process. As the laser is first scanned along the y direction followed by translation along the x direction, the results show the composite effects of overlapping laser pulses in both directions.

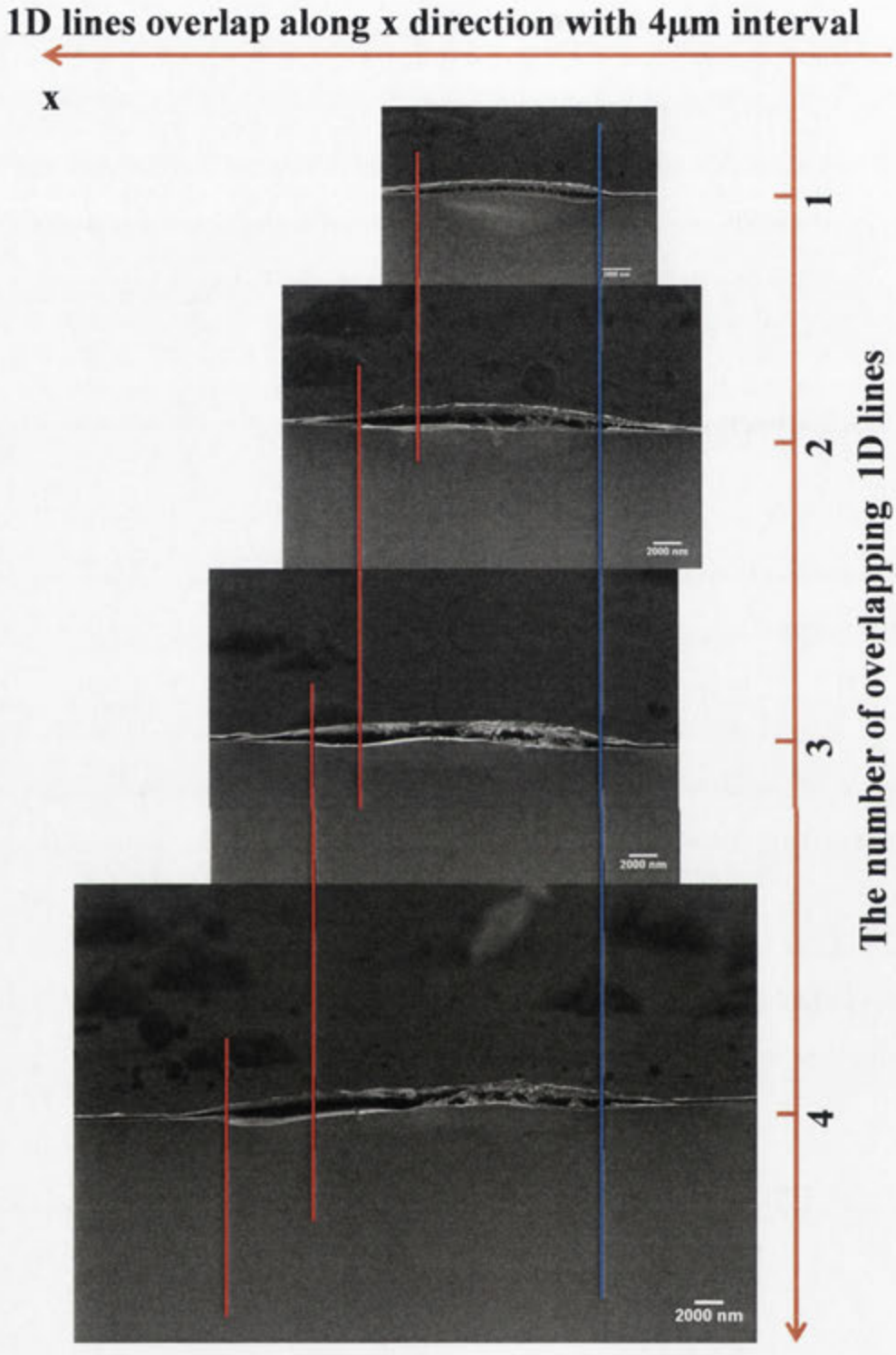

Fig. 37 Aligned images of different numbers of overlapping lines. All lines were processed at 20 kHz using a pulse duration of 50 ns, a pulse energy of 2.5 μJ and a y direction pulse distance of 0.25 μm. The lines are overlapped along the x direction with a 4 μm spacing.

In Fig. 37, the first line warps the SOD film, resulting in a gap and a large number of small floccules between SOD film and silicon surface as discussed in Section 4.7.3.1. The second line has ~73 % overlap with the first line (4 μm line interval and ~15 μm line width). This second line changes the amount and form of the floccules generated by the first line:

1) On the left side where the second laser line irradiated the substrate, the floccules almost disappear, leaving a relatively smooth and clear doped silicon surface. This observation suggests that the floccules are not generated from the SiN_x film.
2) On the right side, especially the 4μm wide region where the second laser line did not overlap, the floccules are still observable, but bigger in size and less fluffy in distribution than that of the first line. It seems that the small and fluffy floccules grow into a "cluster" structure.

Based on these observations, the floccules only form in regions where the silicon is melted and where the SOD film is in direct contact with the nitride prior to the laser pulse. Therefore, at the edges where the SOD film is lifted off but the nitride remains intact, no floccules form. The hypothesis can explain the images following the formation of further lines (3rd and 4th line in Fig. 37). However, it raises the questions why the floccules would form at all, given that the creation of a line involved multiple overlapping pulses along the y direction.

The answer may lie in the different time intervals between subsequent pulses along the y direction (50μs for the 20 kHz repetition rate) and the x direction (in the order of several seconds). The time interval between pulses in the y may be insufficient for the SOD film to warp near the edges between one pulse and the next, allowing the generation of floccules. In conclusion, the laser – SOD – substrate interaction is somewhat different for single lines compared to contiguous areas created from multiple overlapping lines, and this may have an effect on dopant incorporation as well (though

this cannot be ascertained from the SEM images).

The dopant incorporation mechanism from the SOD into the silicon coated with dielectrics using a laser is not as same as the one when applying the SOD in furnace diffusion, where the SOD directly contacts to the silicon and the diffusion temperature is not sufficient to cause the phase change of both the silicon and the SOD film. From Fig. 37, it can be seen that continued doping from subsequent lines can be obtained, which means that the initial contact between the SOD and the SiN_x film, and the formation of floccules, is not necessary for doping. The fact that there appears to be no intimate contact of silicon with the doping source, yet doping still occurs, supports the idea that doping occurs mainly from the dopant source in liquid or gas phase. Due to the extremely high local temperature, it's possible that SOD film melts or vaporises some of it especially from the side facing the silicon, with the dopants then getting incorporated into the silicon.

The analysis of Fig. 38 is more difficult than Fig. 37, because the optical conditions are more complicated here. During the creation of the first doped line, the SOD film breaks roughly along the center of the line. Subsequent lines result in the complete removal of the SOD film above the doped region. After SOD removal by the laser process, thick floccules are generated and cover the surface. In Case B, a laser pulse energy much higher than the silicon evaporation threshold is used, resulting in a higher local temperature, a longer melt duration and a higher local vapor pressure of the silicon than in Case A. This is believed to be the reason for the break-up of the SOD film. Under this condition, floccules appear to originate from the removal of the "peeling off" SOD film rather than the separation of the SOD from the dielectrics with molten silicon underneath as in Case A.

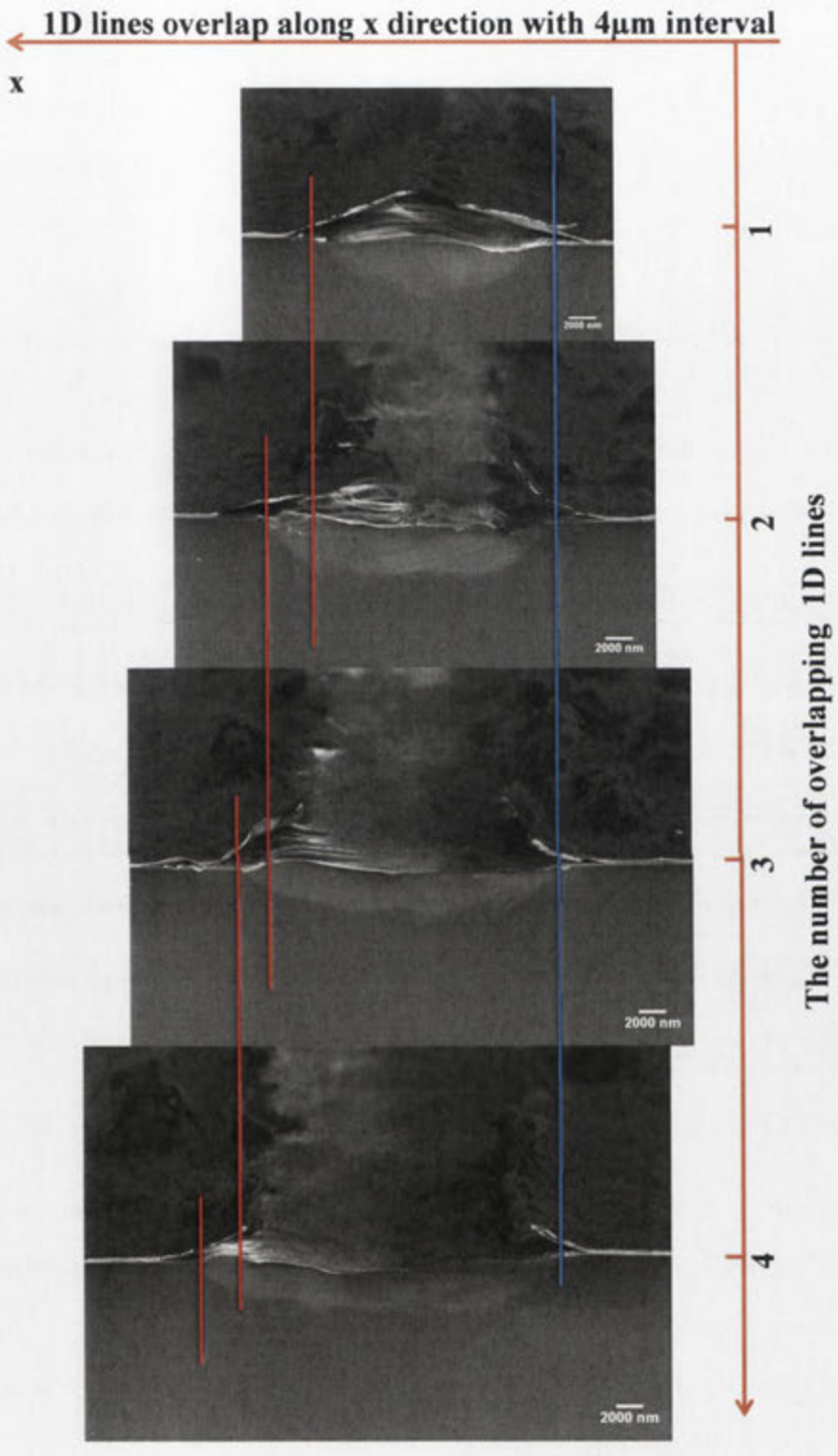

Fig. 38 Aligned images of overlapping laser lines. Lines were processed at 20 kHz using a pulse duration of 400 ns, a pulse energy of 19.9 μJ and a y direction pulse distance of 1 μm. The line spacing along the x direction was 4 μm.

4.7.4 Conclusion

Use of SEMDCI allows more direct observation of the processes taking place during laser doping. Because of the limited knowledge about the interaction of the SOD film with the laser pulses, the dielectric film and the silicon substrate, it is not possible to explain the above observations in detail, but they highlight the complex nature of the interaction between the various materials and the laser pulses. The detachment of the SOD film from the dielectric during laser irradiation is likely to significantly influence the doping process, by influencing the optics of the SOD/dielectric/silicon stack and by altering the processes by which dopant source is incorporated into the melted silicon. The fact that doping is achieved even in cases where the SOD film is already detached from the dielectric prior to silicon melting and doping lends weight to the idea that doping of the silicon occurs, at least in this case, from the liquid or gas phase of the dopant source. The difference in the formation of floccules observed between single and multiple, overlapping lines may indicate that the detachment of the SOD film requires a certain period of time to take place. Furthermore, it is likely that the SiN_x film is incorporated into the melted silicon, potentially introducing recombination active defects.

4.8 Characterization of top surface doping profiles

In addition to cross-sections, SEMDCI can also be used to measure top surface doping profiles, which complement the cross-section data and are particularly useful for point contact characterization. Due to the small and locally isolated features created by point contact doping, it is almost impossible to use other techniques, like EBIC, to do this characterization. An illustrative example of this ability of SEMDCI is to characterize a 'donut' beam profile created by laser beam shaping.

The output of most commercial laser systems is a Gaussian beam profile. If such a beam profile is used in a laser doping process, the cross sectional doping profile

(resulting from a single dot or line) generally follows an approximately Gaussian distribution as well. Such a doping profile is not optimal for solar cell applications, because it increases the risk of shunting or high recombination at the edge of the doped region where the doping depth is much shallower than at the centre. The goal of laser beam shaping is to convert the Gaussian profile into other profiles, for example a donut or a flat-top profile, to improve the uniformity of the produced doping profile. To achieve this, the F-πShaper9 beam shaper from AdlOptic Inc. was employed. In the experimental setup, a collimated Gaussian profile laser beam is passed through the beam shaper and a focussing lens. By carefully choosing the position of the process surface above or below the focal plane, different intensity profiles, for example donut or flat-top profiles, can be obtained.

Figure 39 shows both the initial Gaussian profile of the used laser system at the focal plane and the converted donut profile. Both profiles were measured by placing the laser beam profiler in the beam path.

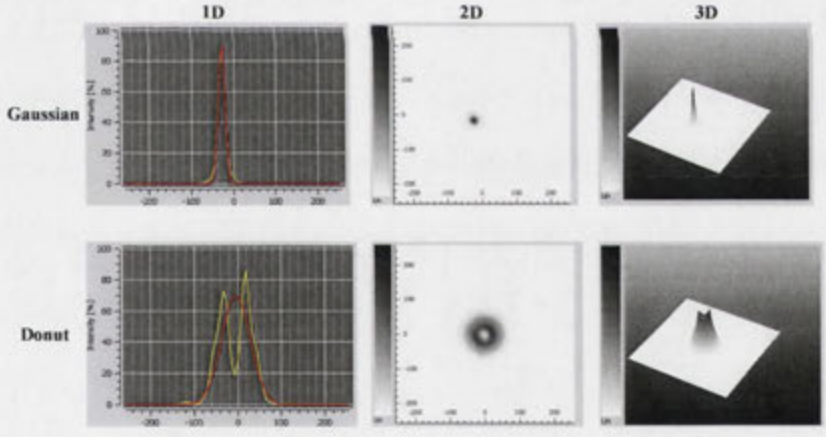

Fig. 39 Beam profiles (1D/2D/3D) of Gaussian and donut distributions measured by placing beam profiler in the beam path. The red lines in the 1D profiles are the corresponding fitted Gaussian profiles. The Gaussian profile fit to the donut profile should be ignored. The length scales on the 1D and 2D profiles are in units of μm.

In order to illustrate the ability of SEMDCI to characterise the top surface doping profiles of small and locally isolated features, I employed SEMDCI on a laser-doped sample (B-SOD on top of the n-type silicon as dopant source) using a donut intensity

profile processed by pulse energies much lower than the silicon evaporation threshold. Low pulse energies reduce the interaction between the regions irradiated by the peak and the bottom of the donut profile, creating maximum contrast in the SEMDCI profiles. The SEMDCI result is shown in Fig. 40. The doped region ring is consistent with the doping profile that would be expected from a donut shaped laser beam. In addition, within the ring the doping distribution is not uniform, instead showing intriguing patterns whose origin is not related to the beam intensity profile. Hence, the doping profile does not only depend on the intensity profile of the laser beam but also on other effects taking place during doping. Figure 41 shows a light microscope image of the SOD film following laser doping, which displays very similar structures to the SEMDCI image. Hence, the porous SOD film is believed to be responsible for the non-uniform doping, through either a lack of dopant availability or the different optical conditions along the lines and spots visible in Fig. 40 and Fig. 41. This SOD effect and the beam profile effect (donut shape) are less significant at high pulse energies, as shown in Fig. 42, where the long melt duration and the enhanced thermal conduction average out the non-uniformity. With the further increase of pulse energy, strong material turbulence (during liquid phase) or even evaporation may happen, so that non-uniform patterns start to appear, as shown in Fig. 42(D).

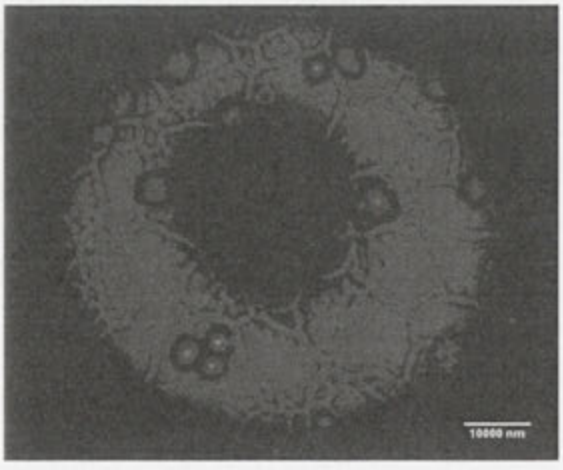

Fig. 40 The top doping profile of a laser-doped silicon processed by a single pulse with a donut intensity profile (300 ns pulse duration) characterized by SEMDCI.

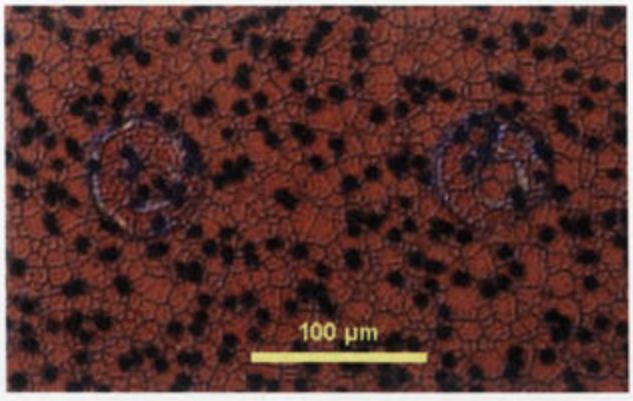

Fig. 41 The light microscope image of the SOD film top surface processed by a single laser pulse with a donut intensity profile (300 ns pulse duration).

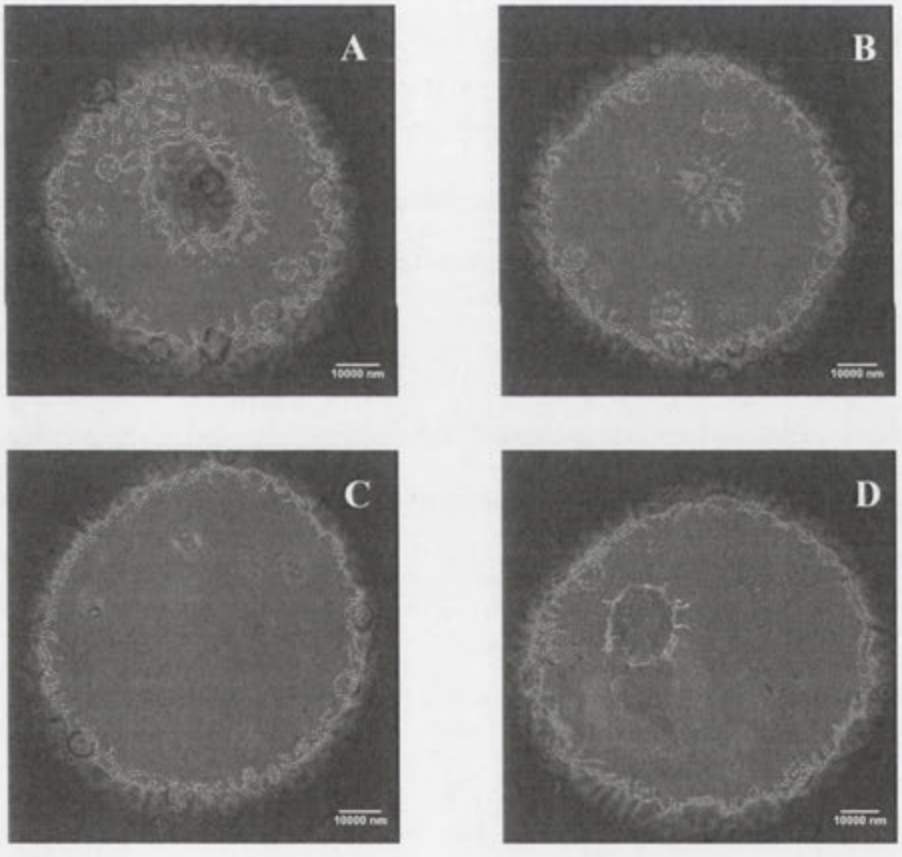

Fig. 42 Top doping profiles of laser-doped silicon processed by a single pulse with a donut profile (5 ns pulse duration) at different pulse energies characterized by SEMDCI. The pulse energy increases going from image A to image D.

4.9 Chapter summary

The mechanisms of the SEMDCI are reviewed and summarised. SEMDCI was tested and successfully applied to the characterization of the diffused or laser-doped silicon regions qualitatively. For p-type doping samples, a quantitative relationship between the contrast and doping concentration has been established, albeit over a limited range of dopant concentrations and with still considerable error. The reliability of the SEMDCI technique was confirmed by comparing it with other reliable and widely used technique —ECV, EBIC and TLM.

The observation of the interaction between SOD, SiN_x, and silicon during the laser doping process shows the detachment of the SOD film from the dielectric during laser irradiation may influence the doping process, by influencing the optics of the SOD/dielectric/silicon stack and by altering the processes by which dopant is incorporated into the melted silicon. The fact that doping is achieved even in cases where the SOD film is already detached from the dielectric prior to silicon melting and doping lends weight to the idea that doping of the silicon occurs, at least in this case, from the liquid or gas phase of the SOD. The difference in the formation of floccules observed between single and multiple, overlapping lines may indicate that the detachment of the SOD film requires a certain period of time to take place. Furthermore, it is likely that the SiN_x film is incorporated into the melted silicon, potentially introducing recombination active defects.

SEMDCI was found to be a powerful technique for the following applications:

1) Detection of p-n junction profile;
2) Determination of semi-quantitative dopant density distribution maps of laser-doped cross-sections;
3) Observation of materials interactions during the laser doping process;
4) Characterization of the top surface doping profiles, which is particularly useful

for characterizing point contacts;

In Chapter 5, SEMDCI will also be used to evaluate the laser doped regions near the edge of the laser-opened dielectric windows.

5 Degradation in the silicon/dielectric interface in the vicinity of laser-doped regions

5.1 Introduction

In the one-step laser doping method, the laser energy is used to selectively remove the dielectric film and simultaneously melt the silicon underneath it while incorporating dopants into the melted region, creating a heavily doped layer. In this process, the dielectric film is employed not only as an anti-reflection coating (ARC) and surface passivation layer, but also as a mask for the subsequent metallization. This one-step process is desirable as it simplifies the process and reduces the fabrication cost.

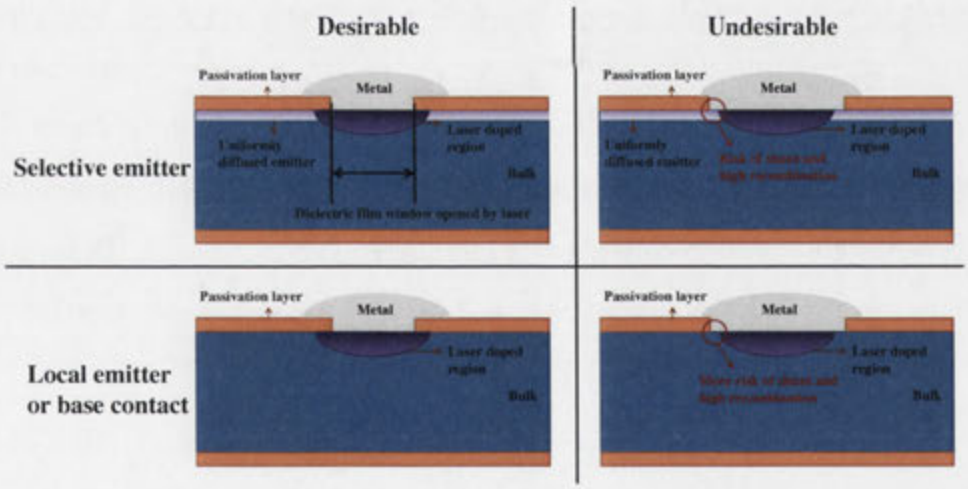

Fig. 43 Illustration of the two main applications of one-step laser doping to the fabrication of silicon solar cells, and the associated risk caused by the lack of doping near the edges in the dielectric window.

One-step laser doping applied to the fabrication of silicon solar cells can be differentiated into two applications, as illustrated in Fig. 43. In one application, laser doping is used to create the heavily doped contact regions within a pre-existing

diffusion, e.g. a selective emitter structure [81]. In this application the heavily laser-doped region is surrounded by a more lightly doped one of the same doping type. In the second application, laser doping is used to form local emitter or base contact regions, where the surrounding area is un-diffused. In this case, the laser-doped region serves the same functions of providing low contact resistivity and limiting contact recombination losses via the creation of a sufficiently deep and heavy locally doped region. However, in this second application, the region near the laser-opened dielectric window edges plays a critical role. If the dielectric window opened by the laser process is wider than the laser-doped region, an un-doped silicon surface will be exposed. This exposed, un-doped and un-passivated region will increase the recombination rate locally. If the laser process is used for local emitter formation, during the subsequent metallization process metal will directly contact the substrate, resulting in an additional conduction path which may manifest itself as a Shottky diode in parallel with the p-n junction diode or even as a shunt, depending on the combination of substrate doping and metallization. Therefore, it is highly desirable to laterally extend the laser-doped regions underneath the dielectric film in order to reduce recombination rates and to prevent the formation of parallel conduction paths. The lateral extension of dopant to a significant depth under the dielectric edge can be considered a necessary condition for the formation of a high quality contact region for this second scenario. The required depth of the doped and exposed region depends on the details of the metallization process, but is typically at least several hundred nm [208-211].

In this chapter, the qualitative and quantitative characterization of the silicon/dielectric interface in the vicinity of the laser-doped region will be explored.

5.2 Qualitative characterization

SEMDCI is an effective technique to characterise silicon/dielectric interfaces in the vicinity of the laser-doped region. In the simplest case, SEMDCI can be used to make a qualitative assessment of which regions are doped, and whether the doped regions

extend underneath the dielectric or not. The limited sensitivity of SEMDCI must be kept in mind in this analysis.

A qualitative assessment can be made both directly (with the dielectric film in place during measurement) or indirectly (with the dielectric removed prior to measurement).

5.2.1 Indirect Qualitative Assessment

5.2.1.1 Experimental

100 mm n-type, 1-20 Ω.cm Cz <100> single sided polished, 525±25 μm thick wafers were used. ~90 nm of thermal SiO_2 was grown on the polished side. B-SOD solutions, from Filmtronics Inc., were applied on top of the SiO_2 as the dopant source. Laser doping was achieved using a DPSS laser, operated in pulsed mode (at 40 kHz) and scanned across the target at different speeds so as to vary pulse distance. Multiple line scans were used for some samples. After laser processing, the residual SOD was removed. Samples were dipped in HF solution for a short time to remove any possible native oxides on the laser-opened surface. Then, the samples were etched in TMAH for 1 min. In this case, only those parts of the silicon exposed to the etching solution were selectively etched, but not the parts protected by SiO_2 films. After TMAH etching, residual dielectrics were removed by HF dip. Samples were freshly cleaved for SEMDCI.

5.2.1.2 Results

The SEMDCI results are shown in Fig. 44. It is apparent that, for some laser parameters, the laser-doped regions laterally extend under the SiO_2 film and have relatively deep junctions near the edges of the dielectric film ((a), (b), and (c)), while for other parameters this is not the case ((d) and (e)).

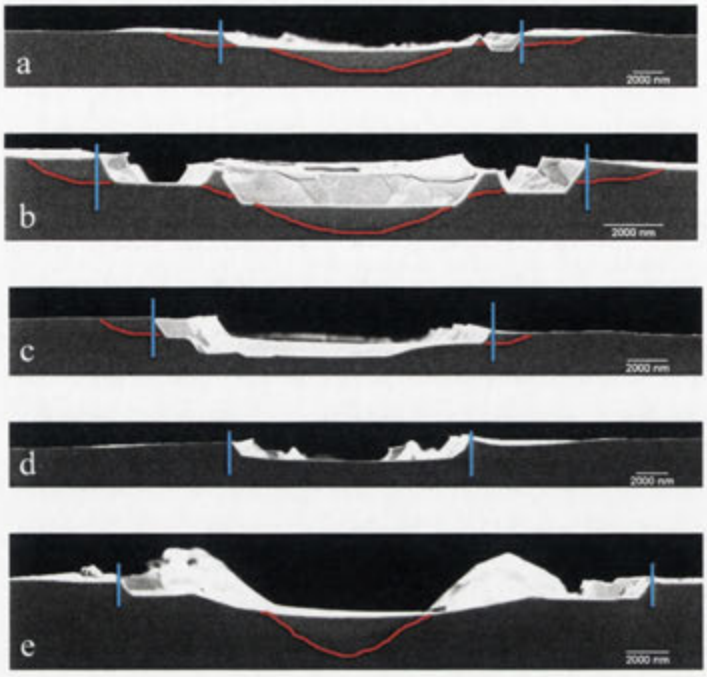

Fig. 44 Application of selective etching (as described in Section 5.2.1.1) to study the laser-doped regions near the edges of laser-opened dielectric windows using SEMDCI. Laser parameters were (a) 16.5 μJ (pulse energy), 0.1 μm (pulse distance), 5 (number of scans); (b) 16.5 μJ, 0.1 μm, 1; (c) 16.5 μJ, 0.2 μm, 1; (d) 16.5 μJ, 1 μm, 5; (e) 22.25 μJ, 5 μm, 5. The contrast boundaries are highlighted with red lines for clarity and the edges of the dielectric windows are indicated by blue lines.

5.2.1.3 Conclusion

The use of SEMDCI and TMAH etch allows the laser-doped samples to be characterized to determine whether the laser-doped region laterally extends underneath the dielectrics or not. Compared to the direct method in next section, the results of this method are relatively easier to be interpreted, since it is usually relatively easy to identify the dielectric window edge from the resulting etch step in the cross sectional profile. However, this method is sensitive to the TMAH itself. If the TMAH etch rate, which is doping concentration dependant, or etch time is not very well controlled, it is possible to etch off the whole doped region, therefore leading to a wrong conclusion.

5.2.2 Direct Qualitative Assessment

5.2.2.1 Experimental

100 mm n-type FZ <100> 525±25 μm thick 100 Ω.cm wafers were used after being shiny damage etched [212,213]. SiO_2/SiN_x stack were deposited on the wafer surfaces. B-SOD was applied as the dopant source. Laser doping was achieved using a DPSS laser, operated in pulsed mode and scanned across the target at different speeds so as to vary the pulse distance. The B-SOD was removed after laser doping but the SiO_2/SiN_x stack was left on surface. The samples were then cleaved for SEMDCI.

5.2.2.2 Results

The results are shown in Fig. 45. It can be seen in this case that a combination of 17.5 μJ pulse energy and 1000 nm pulse distance results in a large gap between the edge of the dielectric film and the doped region. The sample processed at 15 μJ-125 nm provides a better result. The doping region extends underneath the dielectric film with reasonable depth. However, the inhomogeneous doping means that even for this sample a significant risk of a shunt remains.

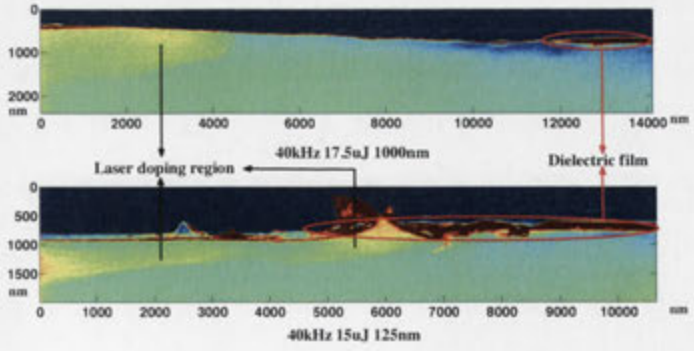

Fig. 45 Laser doped regions near the edges of dielectric film windows characterized by SEMDCI.

5.2.2.3 Conclusion

By leaving the dielectrics on the top surface, SEMDCI can be used to characterize the edge of the dielectric window directly without any further sample processing like TMAH etching. It is more convenient than the indirect method in terms of sample preparation, but a high magnification image is always required to determine the dielectric window edge; even then, in some cases the actual edge is difficult to be determined accurately.

5.3 The impact of SiO_2/SiN_x stack thickness

By applying the direct method discussed above, useful quantitative information about the silicon/dielectric interface in the vicinity of the laser-doped region can be obtained.

5.3.1 Introduction

From the comparison between the use of single layer dielectrics and the dielectric stack in laser doping process, previous researchers suggested the use of a SiO_2/SiN_x stack [17,63,205,214,215]. Tjahjono *et al.* [205] compared the performance of laser-doped solar cells with SiO_2, plasma enhanced chemical vapor deposited (PECVD) SiN_x and SiO_2/SiN_x. Other than the front passivation and ARC layers, the solar cell structures of these three groups were exactly the same. All structures had a textured front surface, front laser-doped selective emitter formed via phosphorus SOD and full aluminum back contact with back surface field. It was found that the SiO_2 group demonstrated the highest V_{oc} but the lowest J_{sc}. The low J_{sc} in the SiO_2 group was due to non-optimized ARC performance of SiO_2 compared to SiN_x and due to the deeper emitter formed by thermal oxidation. A low fill-factor FF in the SiN_x group was assumed to be due to junction recombination/shunting, as more punctures were found in the SiN_x group than in the SiO_2 group. The SiO_2/SiN_x group demonstrated the best overall performance, with good V_{oc}, J_{sc} and FF [63,205]. Further, the high-quality passivation of the

SiO_2/SiN_x stack for both p^+ and n^+ surfaces [215] makes this stack suitable for laser doping applications mentioned previously. Sugianto *et al.* [214] investigated the influence of SiN_x thickness (75 nm and 150 nm) in the SiO_2/SiN_x stacks on laser-doped solar cells by comparing illuminated current-voltage (J-V) curves, using the same structures that Tjahjono *et al.* [205] had used. It was found that the samples with thin SiN_x (75nm) offered a better performance in terms of FF and local ideality factor. The poor performance of the thicker stack group was attributed to higher thermal stress.

It has been found that the thermal expansion mismatch between the different materials contributes significantly to the formation of defects at high temperatures, such as voids adjacent to the laser-doped area and dislocations at the interface between the molten and solid regions [63]. To minimize the formation of such defects, double-layer dielectrics can be used whereby the layer in contact with the silicon is chosen to have a thermal expansion coefficient lower than that of silicon. In this case the underlying silicon is placed under compression [63]. As silicon is stronger under compression [216], the generation of defects in the interface is significantly reduced. The thermal expansion coefficient of SiO_2 is one order of magnitude lower than that of silicon (5×10^{-7} K^{-1} and 2.6-4.6$\times10^{-6}$ K^{-1} for SiO_2 [217] and for silicon [49,63], respectively), so SiO_2 is an excellent choice for this layer due to its ability to simultaneously passivate the silicon surface. SiN_x was chosen as a capping layer due to its suitability as an anti-reflection coating (ARC) and its widespread use by the industry [17,63,214]. Furthermore, the presence of the SiO_2 beneath the SiN_x film is known to provide relaxation of the SiN_x stress [218].

In this section, the influence of SiN_x layer thickness on laser doping is investigated from other perspectives. The focus is on the impact of the SiN_x thickness on the electrical performance (line resistance and contact resistivity) and on the doping profile near the edge of the dielectric window. In order to accurately measure line resistance and contact resistivity, TLM was used. For the investigation of the doping distribution near the edge of the dielectric film windows, SEMDCI was employed.

5.3.2 Experimental

Two phosphorus-doped n-type (100) silicon wafers with resistivity higher than 100 Ω·cm were used in this study. Wafers were saw-damage etched prior processing using a nitric acid and hydrofluoric acid solution. The wafers were RCA cleaned before thermally growing a 19 nm SiO_2 layer on both sides of the wafers. In order to observe a noticeable influence of the SiN_x thickness on the laser doping process, two low pressure chemical vapor deposited (LPCVD) SiN_x layers with substantially different thicknesses (~60 nm, 'thin' group and ~170 nm, 'thick' group) were deposited onto the SiO_2. LPCVD SiN_x was used because it displays a low pinhole density and excellent etch resistance [219]. In addition, while LPCVD nitride does not provide significant surface passivation, SiO_2 / LPCVD SiN_x stacks do provide excellent surface passivation [220,221]. B-SOD solution from Filmtronics Inc., was used as the dopant source. The B-SOD was applied by a spinner followed by oven baking, laser processing and SOD removal. Laser doping was achieved using a DPSS laser (532 nm wavelength, ~30 ns pulse duration, ~30 μm focused beam diameter), operated in a pulsed mode (40 kHz) and scanned across the target at different speeds in order to vary the overlap between laser pulses on the wafer surface. Half of each wafer was used for TLM measurements, while the other half was used for SEMDCI. The laser-doped lines were analysed using TLM to determine the line resistance and the contact resistivity for each set of laser parameters. The contact pads for TLM measurements were formed by aluminium evaporation following a short nitrogen anneal process. Six contact pads with contact spacing between 10 and 280 μm were used for the TLM structure. All samples used for SEMDCI measurements were cleaved just before loading into the FESEM. The SEMDCI method was used to measure the distance between the edge of the laser-doped region and the edge of the SiO_2/SiN_x stack window opened by the laser. An example of an SEMDCI measurement is shown in Fig. 46. In Fig. 46, the vertical axis is the depth scale from the surface of the sample; the horizontal axis is the length

scale along the laser-doped cross-section. Colours indicate dopant concentration, with a darker colour in the cross-section region indicating heavier. While in principle the local image intensity at any point can be used to estimate the actual doping concentration [196], I do not attempt to do so here due to the complexity of the process. The gap distance is defined as the sum of the difference between the dielectric window edge and the edge of the laser-doped region for both sides of a cross-section. Each side of a cross-section was measured separately. In order to increase the accuracy and to decrease the influence of the non-uniformity of doped contrast profiles at different positions along the same laser-doped lines, for each set of laser parameters, at least three cross-sections from different positions along the line were analysed. The final result is an average of these cross-sections. As illustrated in Fig. 46, a negative gap indicates that the doped region extends underneath the dielectric edges, which is the desired result to minimize the risk of very high contact recombination. In contrast, a positive gap implies that there exists an exposed, undoped and unpassivated silicon surface near the edge of the passivation window. The gap distance was measured at high magnification, focusing on the dielectric window edge part in order to increase measurement accuracy. The dielectric window width was then measured at low magnification to include the whole laser-doped region in the field of view. The maximum doped region width is obtained by subtracting the gap distance from the dielectric window width. As shown in Fig. 47, for some samples, while the edge of the doped region is easily defined at high magnification, the edge of the dielectric window is difficult to clearly define. Therefore, maximum and minimum opening positions are estimated and used to determine the measurement error. The maximum opening position marks the position where the dielectric film is visually intact, while the minimum opening position is at the location where the dielectric film is clearly continuous and indistinguishable from the dielectric film further away from the edge. Error bars of the SEMDCI measurements results include the consideration of the standard deviation of measured values from different cross-sections from the same set

of laser parameters, as well as the measurement error as defined above. The error bars allow the estimation of the worst-case situation. This is important because isolated instances of exposed and non-laser-doped regions along a line will result in high recombination along the metal contacts, even if the average gap for that particular laser parameter set is negative.

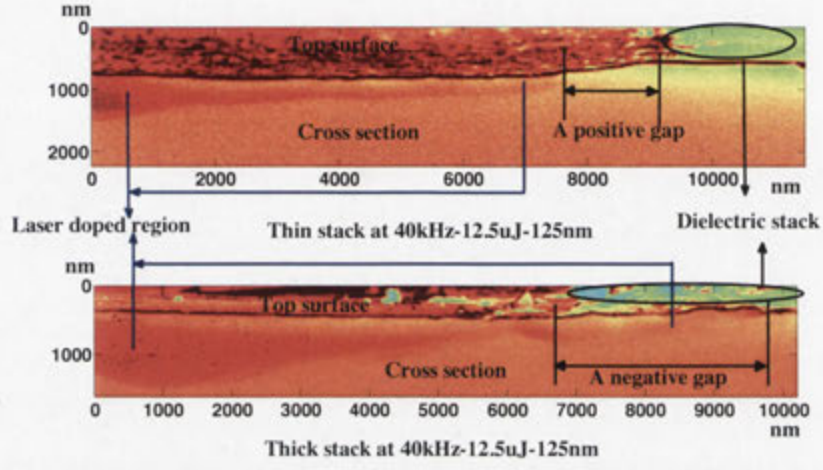

Fig. 46 SEMDCI results (tilted to see both cross section and top surface) of laser doping regions near the edges of dielectric stack windows processed with the same set of laser parameters but different dielectric stack thicknesses. A negative gap indicates that the doped region extends underneath the dielectric edges, which is the desired result to minimize the risk of high contact recombination or shunt.

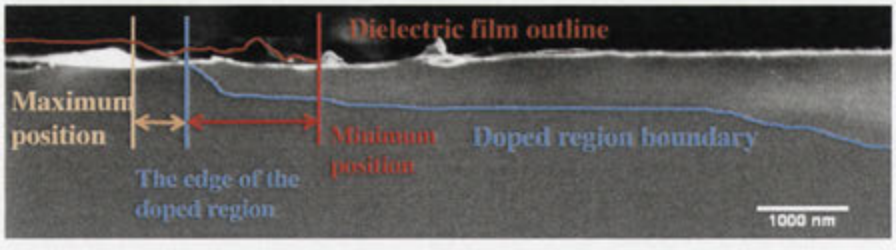

Fig. 47 An example (thick group-15 μJ-250 nm) diagram to demonstrate the maximum and minimum positions of dielectric films opening window that are defined to evaluate the measurement error. The colour solid lines are used to highlight the outline of the dielectric film and the boundary of the doped region. The maximum opening position marks the position where the dielectric film is visually intact (no obvious thickness variation), while the minimum opening position is at the location where the dielectric film is clearly continuous and indistinguishable from the dielectric film further away from the edge.

5.3.3 Result and analysis

The results of TLM, i.e. line resistance and contact resistivity, are shown in Fig. 48 and Fig. 49 respectively. Fig. 48 reveals several interesting results.

Firstly, the variation of resistance values for a given parameter set is larger for samples from the thick group than those from the thin group, especially for samples processed using large pulse distances and high pulse energies. One possible explanation for this variation is that a higher density of surface defects, discontinuities and local ablations are observed in the thick group, which may be partly due to the higher residual thermal stress as discussed by Sugianto *et al.* [214].

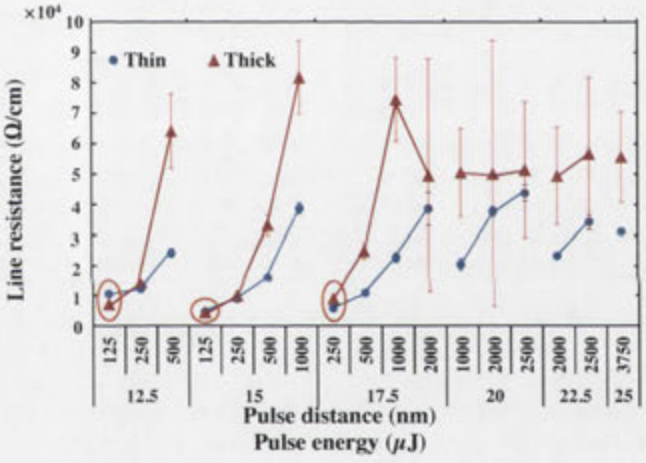

Fig. 48 Line resistance of different sets of laser parameters of two dielectric film stack thicknesses measured by TLM. Note that for some data points the error bars are too small to be visible.

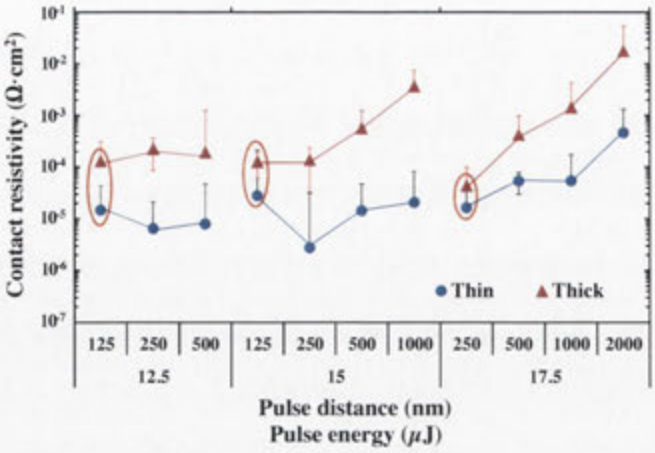

Fig. 49 Contact resistivity of different sets of laser parameters of two dielectric film stack thicknesses measured by TLM. As negative value cannot be presented in log scale graphs, only positive error bars are presented for some of the data points.

Secondly, in most cases, when the pulse energy is constant, the line resistance increases with increased pulse distance. For a pulse energy of 17.5 μJ and above the scatter in the data for the thick group is too large to draw any meaningful conclusions, therefore excluding from analysis. The rate of increase of line resistance with increase in pulse distance is greater for the thick group than for the thin group, for pulse energies lower than 20 μJ. This might indicate that for the thick group, more laser pulses are required before the dielectric film no longer presents a barrier to dopant incorporation into the silicon.

Thirdly, the line resistances of the thin group are lower than those of the thick group for most of the laser parameters. This suggests that the thin stack disintegrates more easily upon melting of the underlying silicon, thus allowing more dopant incorporation. For low pulse energies, with a decrease in pulse distance, an increasing number of pulses irradiate the same region without causing ablation, which enables the dopant to diffuse further into the molten region, until the doping starts to saturate. As a result, similar line resistances (0.45-1×10^4 Ω/cm) are obtained for the samples processed at pulse energies of 17.5 μJ and below with pulse distances lower than 250 nm. This range of line resistance roughly corresponds to sheet resistances of 6-14 Ω/□ if the

doping profile is approximated to a rectangle as wide as half of the maximum doped region width.

The contact resistivity results of the two groups presented in Fig. 49 indicate that for the thin group, the contact resistivity is lower than that of the thick group for all cases, which agrees well with the fact that the line resistance of the thin group is globally lower than that of the thick group as shown in Fig. 48. As the contact resistivity is mainly related to the surface dopant concentration, while the line resistance is also related to the dopant distribution, some discrepancy between the two data sets is not unexpected. While the trend of the contact resistivity is less clear than the trend of the line resistance, the contact resistivity also generally increases with increasing pulse distance, for the same pulse energy. Importantly, the contact resistivity of most laser parameters is lower than $10^{-3}\ \Omega\cdot cm^2$, and thus sufficiently low to ensure minimal contact resistivity losses, for a relatively broad range of parameters. A value of $10^{-3}\ \Omega\cdot cm^2$ corresponds to a contact resistance of 0.1 Ω for a low 1 % contact fraction, which is sufficiently low to not impact significantly on cell efficiency.

As discussed in Section 4.5 , the SEMDCI technique has limited sensitivity to lightly doped or very shallow regions compared to EBIC, and interpretation of SEMDCI is likely to result in an underestimation of the actual extent of the laser-doped region. However, it is assumed that doped regions that do not display SEM contrast are lightly doped and therefore may be considered as undoped for practical purposes, particularly considering the fact that metallization results in the penetration of metal into the silicon surface to a depth of up to several hundred nm. Note that, while EBIC provides an alternative technique to obtain information on the dopant profile, SEMDCI was used here due to the much simpler sample preparation (no contacts required) and much faster characterization speed. Further SEMDCI avoids the need for access to a sophisticated EBIC setup and allows samples to be capped with passivation film.

The results of the SEMDCI analysis are presented in Fig. 50 to Fig. 52. Figure 50

shows the variation in the dielectric window width with varying laser parameters. It is apparent that the dielectric window width is greater for the thinner dielectric layers for all tested conditions. This indicates that a thinner stack layer is more easily removed as the underlying silicon substrate is heated up and expands, and eventually being melted. For the thin dielectric stack, no clear trend of window width with varying pulse distance is evident. For the thick dielectric stack, for each pulse energy there appears to exist a value of the pulse distance which results in maximum dielectric window width, with both higher and smaller pulse distances resulting in smaller widths. This result is somewhat counterintuitive, as one might expect a larger number of pulses to always lead to an equally wide or wider opening than a smaller number of pulses. The behaviour of the passivation film removal in the laser doping process is rather complex, so further investigations are required to understand these trends.

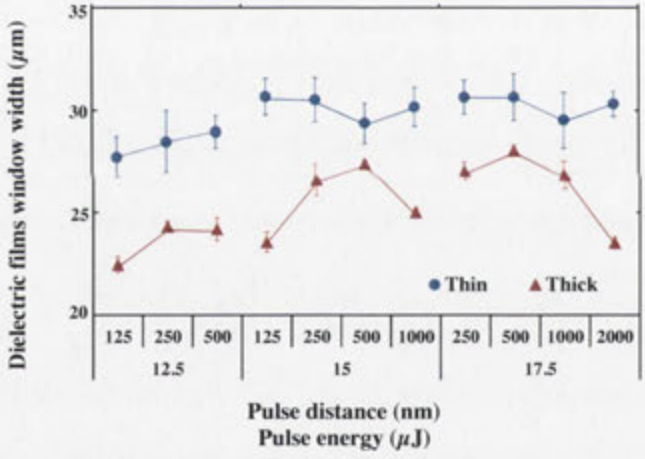

Fig. 50 Dielectric films window width of different sets of laser parameters of two dielectric film stack thicknesses measured by SEMDCI.

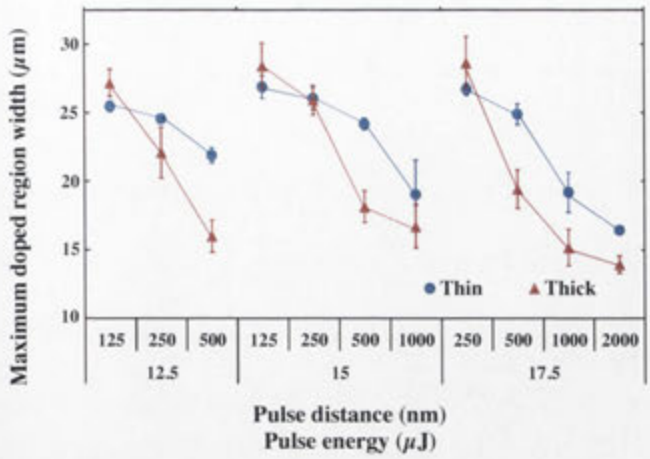

Fig. 51 Maximum doped region width of different sets of laser parameters of two dielectric film stack thicknesses.

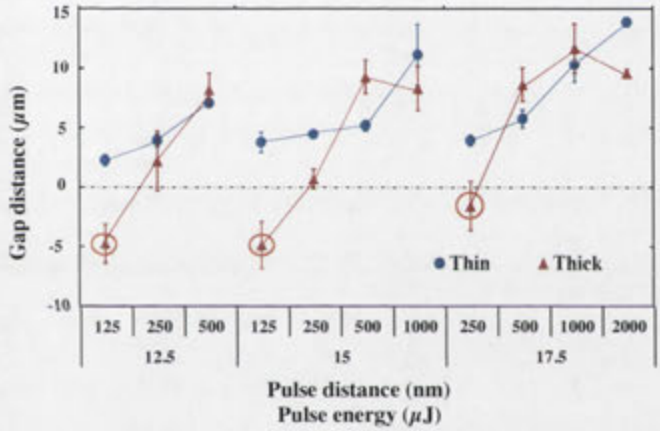

Fig. 52 Gap distance of different sets of laser parameters of two groups with two dielectric film stack thicknesses measured by SEMDCI. A negative gap indicates that the doped region extends underneath the dielectric edges, which is the desired result to minimize the risk of high contact recombination or shunt.

Figure 51 shows the variation in maximum doping region width with varying laser parameters. A clear trend is evident, with a shorter pulse distance resulting in a greater lateral extent of the doping. Comparison with Fig. 50 indicates that for large pulse distances, the doping region width is significantly smaller than the dielectric window width, resulting in exposed, undoped silicon regions near the dielectric window edges. A comparatively small number of pulses therefore appears sufficient to open up the full dielectric window but only results in very shallow or no doping near the window edges.

This may be a result of the shallow melt depth and short silicon melt lifetime in regions near the dielectric window edges because of the Gaussian beam spatial profile of the laser pulses. With an increasing number of pulses per unit line distance, more dopant can be incorporated even near the dielectric window edge and the width of the doped region increases significantly.

Figure 52 shows the difference between the dielectric window width and the doped region width by combining the results of Fig. 50 and Fig. 51. It is apparent that a negative gap is obtained only for specific combinations of the investigated parameters. In particular, the result is obtained for samples with a thick SiN_x, low pulse energies and low pulse distances. This combination of parameters simultaneously minimizes the dielectric window width and maximizes the extent of the doped region, therefore potentially lowering the risk of substantial additional recombination or shunting. This conclusion is different from the one obtain by Sugianto *et al.* [214]. This difference may be a result of the different pulse durations (30 ns in this study, compared to 200 ns), or the different dielectric layer (LPCVD in this study, compared to PECVD). Also, a direct comparison between the two studies cannot be done as different characterization methods were used to evaluate the laser doping process.

The results presented here highlight the fact that, when local laser doping is performed into an undiffused substrate, there are significant challenges presented by the shape of the doping profile which must be considered in order to create high quality contacts. It should be emphasised that the lateral extension of the doping profile under the dielectric is a necessary, not sufficient condition, for the creation of high quality contacts. Other conditions that must be satisfied include sufficiently heavy doping under the contacts and the avoidance of significant material degradation, due to crystal damage or contamination. Further, the depth of the heavily doped region must everywhere be sufficient to prevent metal spiking through this region. Since this depth depends on the metallization process, it must be determined for each particular process.

A way to test the influence of the gap distances shown in Fig. 52 is to measure the shunt resistances of these laser-doped lines. However, the substrates used in the study were high resistivity n-type ones which will not display (ohmic) shunts due to the difficulty in creating ohmic contacts to this material. Therefore, instead of measuring the shunt resistance, PL imaging of the metalized laser-doped lines in a structure of 5×5 mm boxes with line interval of 500 μm (~6 % laser processed area coverage in a box) was done. This method may show a correlation between gap distance and PL intensity provided that the recombination rate of excess carriers is much greater at undoped, metallised regions than in the doped, metallised areas. Therefore, the former recombination dominates, or at least significantly contributes to the overall recombination. Only the samples with thick stacks were tested, as the gap distances of these samples cover both positive and negative values. The laser processed side was facing down and a 1050 nm short pass filter was used for the PL measurement to exclude the possible optical interference of the laser-processed surface. The measured PL signals for different laser parameters were normalized to the maximum measured signal for ease of comparison. The result is shown in Fig. 53. The trend of the observed normalized PL signals is similar to the trend for the gap distances as shown in Fig. 52, with the exception of the data point at 17.5 μJ, 2000 nm. By plotting the normalised PL signal against the gap distance, as shown in Fig. 54, except for one data point, it can be seen that the PL signal decreases with the increase of the gap distance following a roughly linear relationship. However, the PL signal variation is quite small with a maximum variation of ~17 %. This was initially suspected to be due to the very small fraction of the laser-doped regions, since the laser doped regions make up only ~3 % of the total surface area. However, by extracting the effective localized recombination rate using the method mentioned in Section 3.3.7, it was found all the laser-doped lines display very high recombination rates. In this case, the recombination of the laser-processed regions is not dominated by the undoped and exposed regions at the edge as initially expected. Rather, recombination elsewhere, namely in the doped

regions or possibly in the undoped but dielectric covered regions near the dielectric window edge, contributes substantially to overall recombination. High recombination in the undoped but dielectric covered regions near the dielectric window edge could result if the localized heating due to the laser process is insufficient to remove the dielectric but nevertheless destroys the passivation. The result is a poor sensitivity of the PL signal to the gap distance.

Numerical simulations using Quokka (Section 3.3.7.1) under some extreme cases were made to test the influence of the gap distance with small area fraction (0 % to 4 %). In the simulation, the simulated unit (500 μm) and doped region (20 μm) had fixed lengths, and the gap distance was changed from 0 to 20 μm. The gap regions dominated the recombination and determined the PL signal with a 1×10^7 cm/s surface recombination velocity (S_{eff}, see Section 3.3.3.2), while the dielectric covered regions had zero S_{eff} and the J_{0e} of the doped regions varied from 0 to 1×10^6 fA/cm^2. The result is shown in Fig. 55. It can be seen that the simulated PL has an extremely steep decrease with increasing gap distance for gap distances smaller than 0.5 μm and for low to moderate J_{0e}.

Considering both the experimental and simulation results, although the low area fraction of the gap regions and the fact that the laser processed side was facing down in the measurements limit the sensitivity of the PL signal to the gap distance, the observed small variation in the PL signal suggests the presence of a source of high recombination from other effects, as mentioned above. Degradation of the doped regions will be discussed in more detail in Chapter 6.

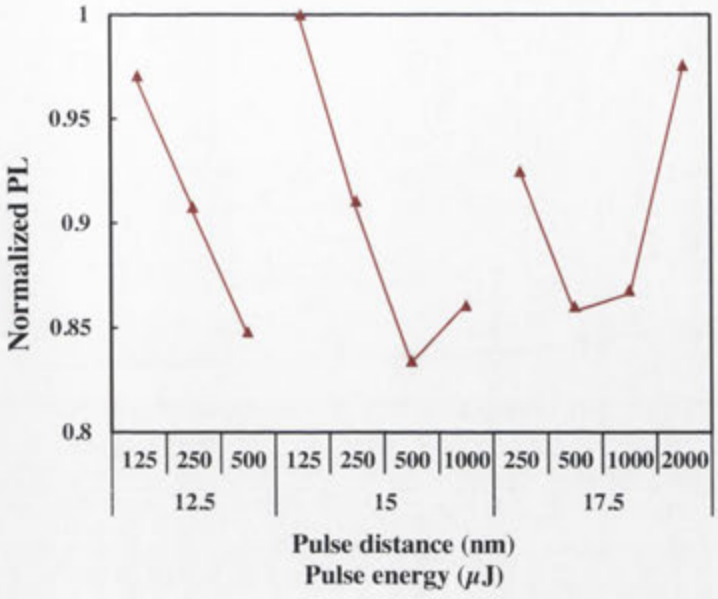

Fig. 53 The normalized PL results of metallised and laser-doped lines which were processed on the same materials using same laser parameters as in Fig. 52. The measured PL signals of different laser parameters were normalized to the maximum one within them for easy comparison.

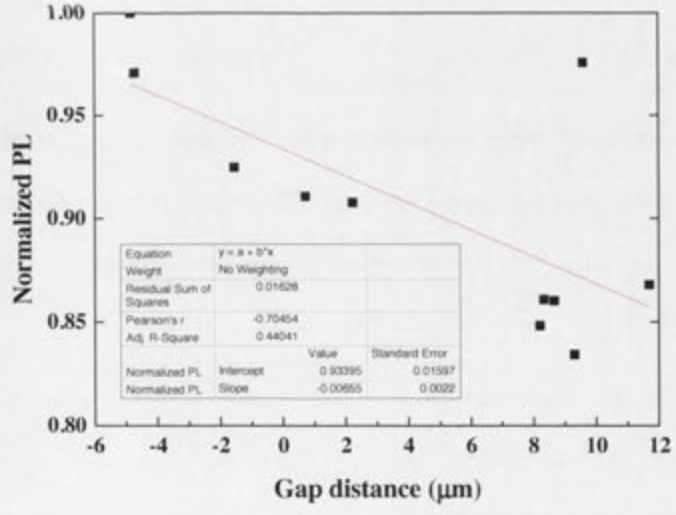

Fig. 54 The Normalized PL signal against the gap distance. A linear fit is shown by the red line.

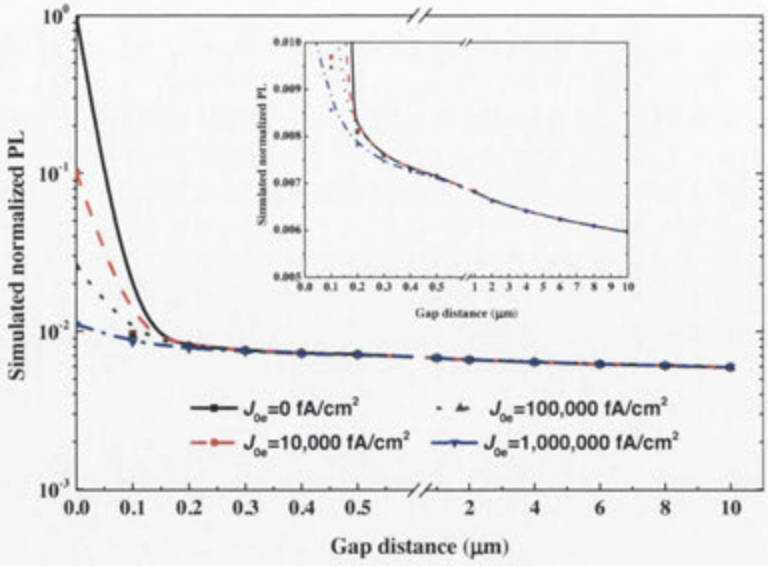

Fig. 55 The PL signal against the gap distance obtained from numerical simulations. The bulk lifetime was fixed as 5 ms. The PL signal is normalized to the PL signal obtained at zero gap distance when the doped region J_{0e}=0 fA/cm^2. The insert plot presents part of the data using a linear y axis. Different marks and colour lines indicate the use of different J_{0e} values of the laser doped region.

5.3.4 Conclusion

The influence of the SiO_2/SiN_x stack thickness on laser doping has been investigated in this section by measuring two pertinent groups of parameters, namely the line resistance and contact resistivity measured by TLM, and the gap distance between laser-doped regions and the edge of SiO_2/SiN_x stack windows opened by laser characterized by SEMDCI.

It was found that, for the used DPSS laser system, the detailed properties of laser-doped regions opened through dielectric films are significantly influenced by both the thickness of the dielectric films and by the laser process parameters. Over the range of laser parameters studied, the thin stack generally results in lower line resistance and contact resistivity, while the thick stack offers a smaller gap distance. An increase in laser pulse energy or pulse distance generally results in worse performance regarding the studied properties, in other words, higher contact resistivity and line

resistance, and larger (positive) gap distance. Fundamentally, a problem of positive gaps was identified and found to be present in most of the investigated parameter range. However, optimization of the laser parameters and dielectric film conditions has been shown capable of potentially overcoming this problem. Consideration of the line resistance, doping profile and dielectric window width indicates the existence of a process window that results in desired line properties. The samples capped with thick dielectric stacks processed at low pulse energies and with low pulse distance offer the optimal results over the parameter range studied.

It should be emphasized that the scope of the current study is limited. The optimal results mentioned here are necessary but not sufficient conditions for high quality contacts. Other considerations, such as the optimization of dielectric stack optical properties, are also important for designing high efficiency solar cells.

5.4 Measurement of passivation degradation near the edges of laser-opened dielectric windows

5.4.1 Introduction

In Sections 5.2 and 5.3, the possible gap between the laser-doped region and the edge of the laser-opened dielectric window was investigated. However, as shown in Fig. 56, even when there is no observable gap, good electronic properties are not guaranteed, since the passivation provided by the dielectric film may be degraded near the edge of the opened window as a result of the high temperatures and thermal stresses experienced in that region. To the best knowledge of author, there exists no published research on this problem. Detection and quantification of such degradation of dielectric passivation is not straightforward.

In theory, EBIC could be used for a qualitative assessment, if the cross-section of a sample can be well passivated. In this case, a decrease of the EBIC signal in the

vicinity of the residual passivation film could be regarded as evidence of passivation degradation. However, practically, it is very difficult to uniformly passivate a cleaved cross-section. In this section, an experimental method is proposed to investigate this problem. Unfortunately, to date attempts to implement this method have been unsuccessful due to inappropriate choice of the passivation film, as is discussed below.

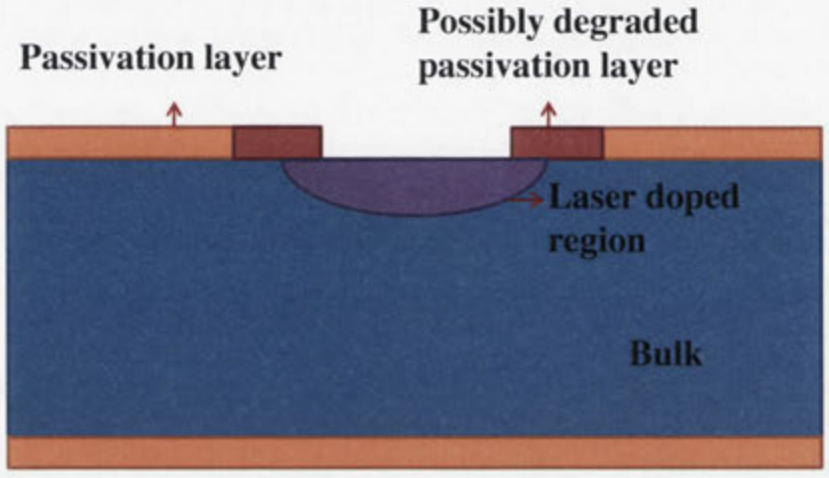

Fig. 56 Illustration of the possible passivation degradation at the edge of the laser-opened dielectric window.

5.4.2 Experimental plan and mechanism

The experimental procedure is described in Fig. 57. The experiment consists of 6 experimental steps from A to F. Using the localized recombination analysis method discussed in Section 3.3.7, the effective J_0 of the laser processed region in step F and D can be extracted.

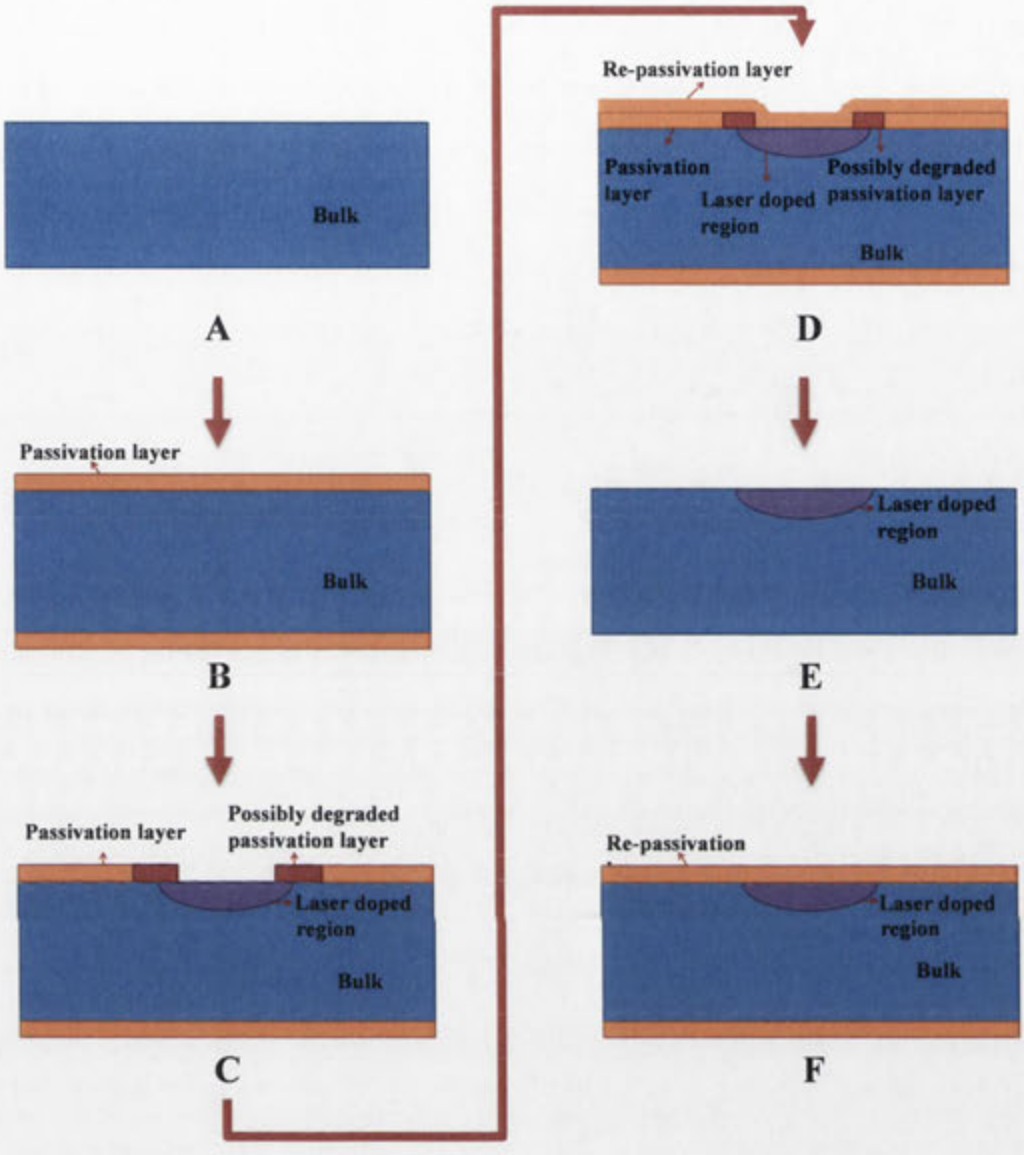

Fig. 57 Experimental procedure to investigate possible degradation of dielectric passivation.

Step F allows determination of the J_0 of the laser doped region, or at least an upper bound of the J_0 of the laser doped region assuming that the J_0 due to the passivated, laser-doped surface is small compared to the bulk J_0 (which may or may not be the case). In contrast, Step D includes the residual surface passivation layer at the edge of laser-opened windows in Step C. If this part of the passivation layer was degraded by the laser process, the extracted effective J_0 of the laser doped region of Step D could be dominated by the degraded surface passivation rather than the bulk J_0. Comparison

of the J_0 or directly the PL measurement results of step F with D allows determination of whether or not the passivation near the dielectric edge is degraded. The above relies on the ability to effectively passivate the laser doped surface, and good electronic quality of the laser-doped region (i.e. low to moderate recombination). Also, it is assumed that the second passivation does not passivate the laser-induced defects. If these conditions are not met, the measurements will not be sensitive to the possible degradation at the dielectric window edges.

5.4.3 Results and discussion

In initial attempts to apply the above experimental method, SiN_x was chosen as the passivation film. However, later experiments showed that SiN_x can induce significant degradation to the laser-doped region. This degradation will be discussed in detail in Chapter 6. The use of SiN_x, resulted in high values of J_0 of the laser-processed region, which made the application of the above method impractical.

5.4.4 Conclusion

The investigation of the passivation film (especially SiN_x) degradation at the edge of the laser-opened windows is of interest, particularly if one-step laser doping and contacting processes are considered. The proposed experimental method could provide an avenue to study this phenomenon for suitable dielectric films and dopant sources, which result in high quality laser doped regions which can be well passivated.

5.5 Chapter summary

In this chapter, some of the properties of the edges of the laser-opened dielectric windows were investigated. The SEMDCI technique, introduced in Chapter 4, was used to the lateral extent of the laser doped regions, relative to the dielectric window edge, and to correlate this extent with the laser and dielectric film parameters.

It is highly desirable to laterally extend the laser-doped regions underneath the dielectric film in order to reduce recombination rates and to prevent the formation of parallel conduction paths. This was shown to be achievable if the laser parameters and dielectrics film thicknesses and properties are carefully chosen. Meeting this condition is a prerequisite for producing a good laser-doped contact region. However, even when this condition is met, contacts with poor electronic properties may still result because of possible degradation of passivation films close to the window edge. Experimental methods are therefore proposed to detect such degradation.

6 The influence of thermal effects and dielectric films on the electronic quality of highly doped silicon processed by nanosecond laser

6.1 Introduction

One challenge of the application of laser doping to high efficiency solar cells is the need to maintain at least a moderate electronic quality in the laser-processed silicon. Fell *et al.* [222] estimated the efficiency potential for an idealized point-back-contact solar cell (1.5 Ω·cm, n-type bulk, 160 μm thickness) using numerical simulation with various J_0 and contact resistances (r_{cont}, in units of Ω·cm^2) of the local contacts. In the simulation, the pitch between contacts for each combination of the two parameters was optimized. Although that was an ideal case simulation because of a bulk lifetime limited only by Auger and radiative recombination, zero surface recombination other than the localized contact region, no shading, and optimized optics, it revealed that while good contact resistance ($r_{cont} < 10^3$ Ω·cm^2) is generally easy to achieve using laser doping, a moderate electronic quality ($J_0 \leq$10,000 fA/cm^2) is required for the cell with small localized contact size (10 μm ×10 μm) to achieve over 24 % high efficiency. The fact that a moderate rather than a small J_0 is already sufficient can be explained by the low area fraction and current crowding effects.

Although advanced characterization methods for laser doping have been developed [17,63,73,127,159,196,223], the dependence of the electronic quality of the laser-processed region on the combination of laser parameters, dopant precursors and dielectric films is complex and has not been fully elucidated. Literature reports do suggest the ability of laser doping to achieve successful dopant incorporation with low

material quality damage, as demonstrated either through measurements of the carrier lifetime and saturation current densities [224,225], or through demonstration of good cell performance [36,108]. However, in these publications, the lifetime and recombination parameters were characterized using large and contiguous doped areas that were produced with dopant precursors and two-directional laser pulses overlapping. This means that the results are a composite of the effects of dopant incorporation (with greater dopant incorporation generally resulting in lower recombination rates for the same defect types and densities) and defect generation. This makes it difficult to distinguish between these two effects. Further, the use of large and contiguous areas means that edge effects that will be present when lasers are used to form doped lines or dots, are not included in the measurements. Finally, because the focus in previous publications is usually on achieving overall good cell performance for a specific laser doping application, thermal effects and the impact of dielectric films were not systematically studied.

In this chapter, the influence of thermal effects and the impact of dielectric films on the electronic quality of p^+ doped silicon surfaces processed using a pulsed laser system are systematically studied. In contrast to previous work, sample doping is performed by furnace diffusion *prior* to laser processing rather than through dopant precursors. This allows the investigation of thermal and dielectric effects without the complicating effect of variable substrate doping concentrations. The diffusion provides a moderate degree of surface passivation required for PL imaging, and serves as a reasonable approximation of a laser-doped contact area, with very high surface recombination velocity and a doping profile approximating that of typical laser-doped regions.

In order to ensure the results are applicable to the laser-doped structures created in solar cell fabrication, laser processed lines and dots were produced; therefore, the potential large influence of the perimeter regions of laser processed lines is included.

Two sets of experiments were carried out in this study. In the first set, high lifetime

wafers with boron diffusions on both surfaces were used as the starting material. Various dielectric films were applied on one surface (or in some cases, the surface is left bare) and the samples were laser processed in air (on the side with the dielectric film if present) using a wide range of laser parameters. Following laser processing, any dielectric layers or native oxide films were stripped and the samples measured by PL imaging. The recombination current pre-factor (J_{0e}) of the laser processed regions was extracted by computational modelling (see Section 3.3.7). In a second set, a dopant precursor was applied to bare silicon wafers and used to dope the silicon. The same laser parameters as for experiment set 1 were used for set 2 to create doped, contiguous areas of sufficient size to allow measurement of sheet resistance by 4PP laser box method (see Section 3.2.1).

The first set of experiments allows assessment of the impact of thermal effects and dielectric films, nearly independent of the effect of doping incorporation and interaction with dopant precursors. The dopant present in the boron diffusion is redistributed during laser processing, but this distribution has comparatively little impact on J_{0e}, since J_{0e} is mainly determined by total dopant dose [27]. Therefore, in this study, it is assumed that the laser-induced dopant redistribution will not change the J_{0e} of the re-diffused regions. The extraction of recombination parameters of unpassivated, laser-processed areas is of relevance since laser doping is usually employed to create contact regions. Since a uniform diffusion is created prior to laser processing, the measurements do not take into account the complex dynamics of dopant incorporation and distribution through a dielectric film, which usually results in quite a non-uniform dopant profile [196,226]. Measurement on unpassivated surfaces means that damage to dielectric passivation at the edges of the laser-processed regions (see Chapter 5) is also not considered.

The second set of experiments allows an assessment of the doping, more generally the melting of silicon, achievable as a function of the laser parameters. Reasonable doping (typically ~100 Ω/□ or lower) is usually necessary to achieve acceptably low contact

resistivities. The values obtained represent an upper bound on the achievable doping since the presence of the dielectric impedes the incorporation of dopant into the silicon. Laser parameters that do not result in a sheet resistance lower than a threshold value (set to 200 Ω/□ in this chapter) are highly unlikely to allow the realization of good quality contacts. Comparing the doping/melting results with the recombination properties investigated in the first set of experiments, it fundamentally tests whether the low recombination and good doping (sufficient melting) can be achieved at the same time.

Thus, the nature of the processing and measurements used here is, necessarily, both an advantage and a limitation. They allow certain basic information about laser processes to be extracted, but do not necessarily simulate all the effects that will be encountered in the application of laser doping to device fabrication.

6.2 Experimental

Phosphorus-doped n-type (100) float-zone silicon wafers with resistivity higher than 100 Ω·cm were used. Wafers were saw-damage etched using a nitric and hydrofluoric (HF) acid solution. The wafers were classified as group A and group B for PL imaging and 4PP measurements, respectively.

Group A wafers were RCA cleaned and loaded into a boron diffusion furnace to achieve a shallow p doped layer with sheet resistance of ~90 Ω/□ on both sides. After boron diffusion, the wafers were deglazed in HF until hydrophobic. Group A wafers were then divided into several subgroups which were capped with different dielectric films as follows: bare silicon, 50nm thermal SiO_2, 20nm atomic layer deposited (ALD) Al_2O_3, ALD Al_2O_3 (10 nm) / TiO_2 (50 nm) stack, and plasma-enhanced chemical vapor deposited (PECVD) SiN_x deposited using three different recipes. These three films, referred to as SiN_xA, SiN_xB, SiN_xC below, were deposited at 230 °C ([Si-N] density ~1×10^{23} cm^{-3}), 290 °C ([Si-N] density ~1.05×10^{23} cm^{-3}), and 400 °C ([Si-N] density

~1.28×10^{23} cm^{-3}) respectively, but have similar optical properties (n=~1.9 at 633 nm) and thickness (~80 nm). All groups were then processed on the side with dielectrics using a PyroFlex™ 25 laser system at a wavelength of 532 nm and at frequency of 20 kHz. The laser is operated in pulsed mode and scanned across the target at different speeds so as to vary the distance between pulses on the wafer surface. The laser pulses had approximately Gaussian temporal and spatial beam profiles. The $1/e^2$ Gaussian radius of the focused laser beam used is 9.8 μm, which was measured by the method of Kiang and Lang [204]. Three pulse durations — 20 ns, 100 ns, and 400 ns were used, where pulse duration is defined as the full width at half maximum (FWHM). Four pulse distances (0.25, 1, 2.5, and 20 μm) were investigated to cover both overlapped and separated pulses conditions. Pulse energy, measured in units of μJ, was also varied over a wide range for each studied pulse duration. The layout of each set of laser parameters is a 4×4 mm^2 unit which consists of parallel laser processed lines with 30μm pitch. Figure 58 shows one of the measured PL images and illustrates the used laser-processed layout. Prior to measurement, wafers were dipped into HF solution until fully hydrophobic to remove all surface films, in order to ensure a bare silicon surface with high recombination velocity.

After HF dip, all group A wafers were characterized by PL imaging using a BT Imaging LIS-R1 system with a zoom lens (24 μm/pixel resolution) and 1050 nm short pass filter. Small area illumination, highest possible laser source power (~2.63×10^{18} photon flux) and long exposure times (30 s) were used to enable sharp PL images with high signal to noise ratios. Samples were illuminated with the laser processed side facing down, to ensure that the illuminated surface is optically uniform. To decrease the reflection from the center coil of PL sample table, a black absorptive film was loaded under wafers when taking PL images. The background (unprocessed region) PL signals of each sample were also recorded.

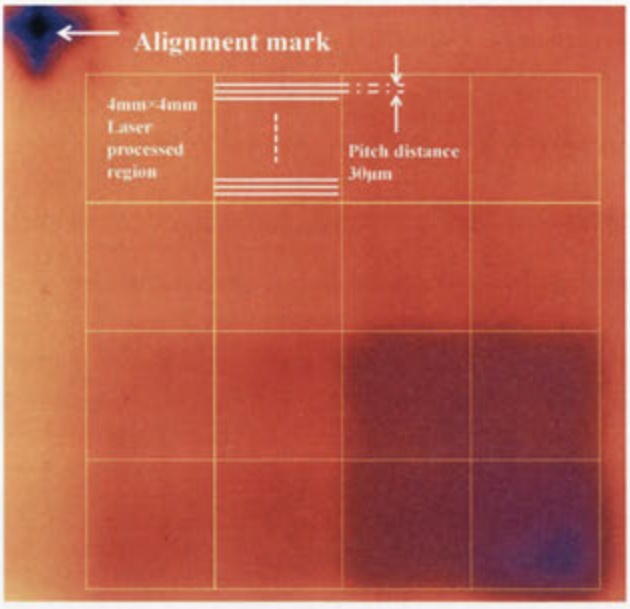

Fig. 58 An example of measured PL image and the illustration of laser process layout of group A wafers. This is the PL image of the wafer initially with Al_2O_3 film.

Group B wafers were RCA cleaned and capped with B-SOD, commercially available from Filmtronics Inc. The same laser parameters used on the bare silicon group of group A were applied to group B, except where the pulse distance (20 μm) generated separated dots that would not be measurable by the 4PP laser box method. The layout of each laser processed unit is a 5.5 mm×1 mm box consisting of parallel laser processed line with a 10 μm lines interval i.e. ~33 % overlapping ratio. The resistance of each box was measured by 4PP with an IV sweeper and was then converted into sheet resistance (R_{sh}) by applying the appropriate geometric calibration factor (see Section 3.2.1).

6.3 Data processing

Assessment of the impact of laser processing on material quality requires the conversion of the PL data to a parameter characterizing recombination in the laser processed regions. Since the laser processed region lies within the diffused region, J_{0e} is considered the most appropriate measure. In this chapter, the J_{0e} of the laser-doped regions, normalized to the J_{0e} of the unprocessed and diffused regions (referred to in

the chapter as J_{0en}), was determined and used as the main parameter to assess the quality of laser processed regions.

J_{0en} was determined using the method introduced in Section 3.3.7. First, the lifetime of a calibration sample from the group A wafers without any laser process and any dielectric was measured using a Sinton Instruments WCT-120 lifetime tester [144] and a PL image of the same sample was taken. The lifetime in the sample is completely limited by recombination at the surfaces, since the bulk lifetime of the wafers was measured to be several ms and the surfaces were unpassivated. The J_{0e} value of the calibration wafer was extracted from the lifetime measurements using the technique developed by Thomson [227]. Numerical simulation of the calibration sample using Quokka [127,171] allows determination of a simulated PL signal by assuming only intrinsic recombination in the bulk and by applying the determined J_{0e} value to both front and rear side emitters. Comparison of the measured PL signal with the PL signal simulated by Quokka enables determination of a calibration constant A. A is a measure of the fraction of photons emitted by the sample that is collected by the detector using a certain PL setting (choice of zoom lens, short path filters etc.). This calibration constant is the same for all samples studied because the PL settings used are the same.

J_{0en} of each laser processed region can then be determined by establishing the relationship between the PL signal and J_{0en} of the laser-doped regions, again using Quokka, with A an input into the simulation. This relationship will depend on the background (unprocessed region) J_{0e} and therefore has to be established for each sample, since the background J_{0e} of different samples was slightly different. For the purposes of the modelling, the electronic properties within a processed region are constant, so extracted J_{0en} values are the lumped or 'average' values of the actual ones, which are expected to be non-uniform in general.

Fig. 59 shows this relationship for several representative background J_{0e} values, obtained from different samples. Both J_{0e} and PL counts were normalised to the

background values for each sample and are referred to as J_{0en} and PL_n in the following discussion. Given that the background J_{0e} is ~2200 fA/cm^2 (for n_i=9.65×10^9 cm^{-3} [228]), only J_{0en} values < ~5 are considered of practical interest as larger values than this will impose significant limitations of solar cell parameters (particularly the achievable conversion efficiency), even for small area contact fractions [222].

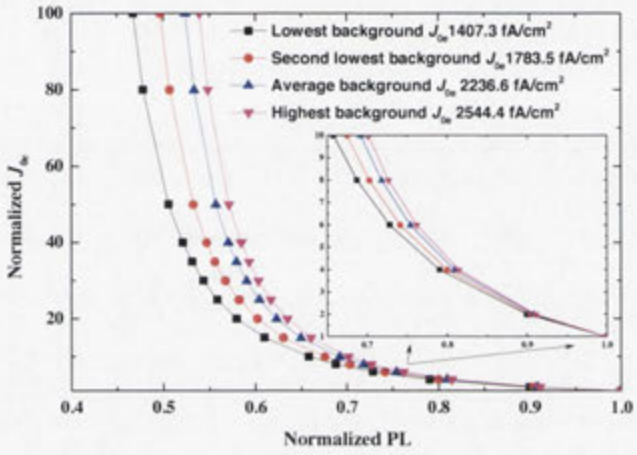

Fig. 59 The influence of background J_{0e} on the relationship between J_{0en} and PL_n. The insert plot magnifies the range of J_{0en} lower than 10. All the background J_{0e} annotated are valid for n_i=9.65×10^9 cm^{-3}.

Simulation of the laser processed samples using Quokka required knowledge of the line width. Optical microscope inspection of the samples showed ~15 μm line width for all samples and laser parameters, and this value was used for the simulations. However, the actual width of the laser processed regions may be different from the optical width. To quantify the error caused by this uncertainty, the Quokka simulation was repeated with different line widths using the average background J_{0e}. This is shown in Fig. 60.

As J_{0en}=1 represents the background without any laser processing, (J_{0en}-1) can be regarded as the additional recombination due to the laser process. When the recombination is not too large, the total additional recombination (i.e. the drop of PL signal) will be proportional to the product of (J_{0en}-1) and the laser doped line width.

Therefore, for sufficiently low J_{0en}, the following relationship holds:

$$(J_{0en1} - 1) \times W_1 \approx (J_{0en2} - 1) \times W_2 \ , \tag{6-1}$$

where W_1 and W_2 are two assumed line widths, and J_{0en1} and J_{0en2} are the values of J_{0en} extracted using the respective values of W. For J_{0en} <10, the data in Fig. 60 matches above relationship well. The percentage error associated with J_{0en} is therefore always smaller than percentage error in the line width (and approaches it for larger J_{0en}).

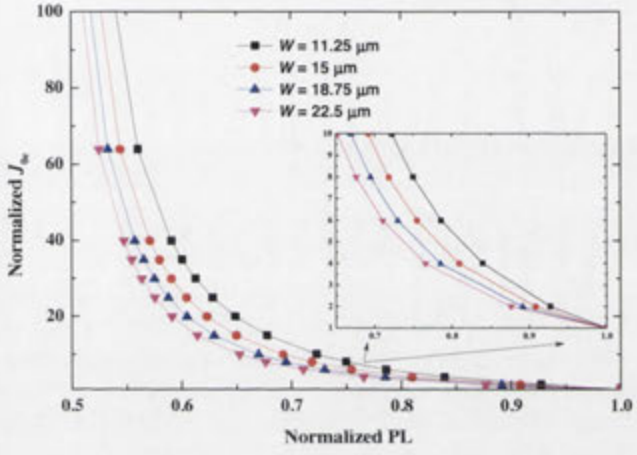

Fig. 60 The influence of the effective width of laser processed lines on the relationship between J_{0en} and PL_n. The insert plot magnifies the range of J_{0en} lower than 10. The average background of J_{0e} (2236 fA/cm^2, when n_i=9.65×10^9 cm^{-3}) is used in this simulation.

The ideality factor associated with recombination in the laser processed regions for the samples with or without dielectrics (except SiN_x group) was checked by measuring and simulating the PL signal at two different illumination levels (~2.6×10^{18} and ~7.9×10^{17} photons/cm^2·s flux, corresponding to ~10 and ~3 suns respectively where 1 sun=~2.7×10^{17} photons/cm^2·s). There was no observable increase in non-ideal recombination compared to the unprocessed background regions for J_{0en}<5. For samples with greater J_{0en}, measurements at the lower injection levels suffer from too low signal levels so no definitive conclusion could be drawn. Therefore, recombination can reasonably be represented by a single J_{0en} value for each set of laser parameters.

Fig. 59 and Fig. 60 are based on overlapping laser pulses resulting in contiguous lines (pulse distance $\leq 2.5\ \mu$m in experiments). Similar simulations were carried out for the case of separated dots (20 μm pulse distance) and led to the same conclusions.

As discussed above, in this chapter J_{0en} is used rather than J_{0e} as an indicator of electronic quality of the laser processed region. Although J_{0e} is a more physically meaningful value, the variation in background J_{0e} values for the different group A samples will make the comparison and interpretation of J_{0e} from these different samples problematic. Hence, the use of normalized J_{0e} values was considered preferable.

6.4 Laser processing on bare silicon

In order to test whether high dopant incorporation (sufficient silicon melting) and low recombination (for highly recombining surfaces in the presence of boron doping) can be achieved at the same time, the J_{0en} results of the bare silicon samples of group A and the R_{sh} results of group B are analysed together in this section. For ease of comparison, a parameter window is defined such that only parameter combinations where both J_{0en} and R_{sh} are below chosen threshold values fall within this parameter window. It must be emphasized that this concept of a parameter window merely enables the identification of parameter sets which *may* result in acceptable properties if used to create laser-doped lines, while parameter sets outside the parameter window are unlikely to result in acceptable properties. Here, a threshold J_{0en} value (referred to as the damage threshold) of 4 was chosen, corresponding to J_{0e} ~10000 fA/cm^2. The threshold value of R_{sh} (referred to as the doping threshold) was chosen as 200 Ω/□.

The results of three different pulse durations are shown in Fig. 61 to Fig. 63. The damage and doping thresholds are summarized in Fig. 64, together with the evaporation threshold which will be discussed in Section 6.6. The parameter windows are indicated as colour bars in Fig. 64, which is the range of pulse energies between the

damage and doping thresholds. The results show that low recombination and good doping can in principle exist at the same time, and that laser pulse duration and pulse distance have a significant impact on the width of the parameter window.

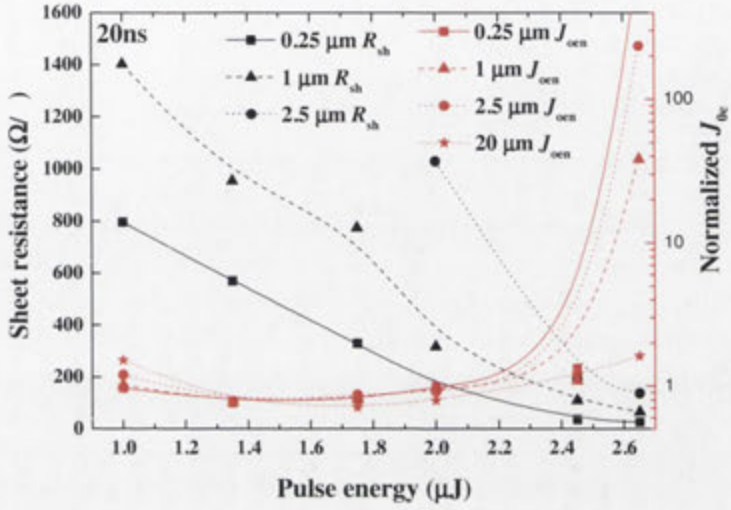

Fig. 61 4PP and PL results of the bare silicon sample irradiated with pulses of 20 ns pulse duration. The black lines illustrate the trend of sheet resistance (left y axis) with the change of pulse energy, while the red ones correspond to the trend of Normalized J_{0e} (right y axis). Different line styles and marks are used to separately illustrate the cases for different laser pulse distances.

For all pulse durations, at a given pulse distance, R_{sh} decreases with increase in pulse energy. Further, in most cases R_{sh} decreases with decreasing pulse distance. These observations are expected, as the dopant from the precursor is more easily incorporated into the bulk at higher pulse energy (which results in a larger melt volume and longer melt lifetime) or for a larger number of pulses (longer overall melt lifetime).

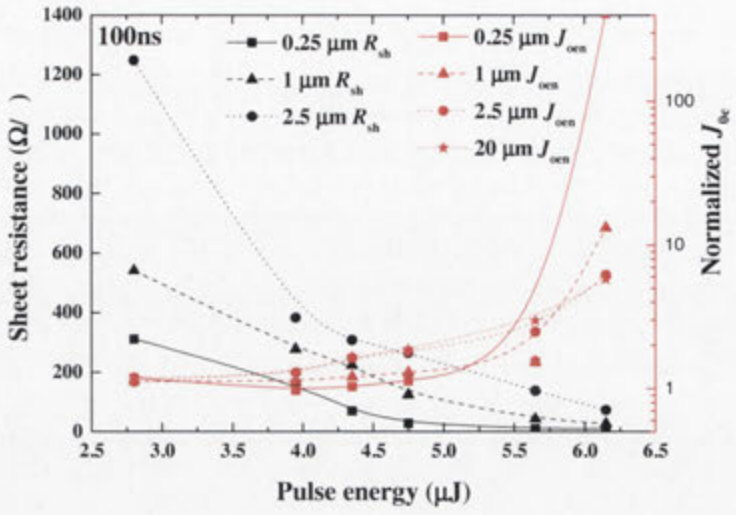

Fig. 62 4PP and PL results of the bare silicon sample irradiated with pulses of 100 ns pulse duration. Same plot setting is used for this figure as in Fig. 61.

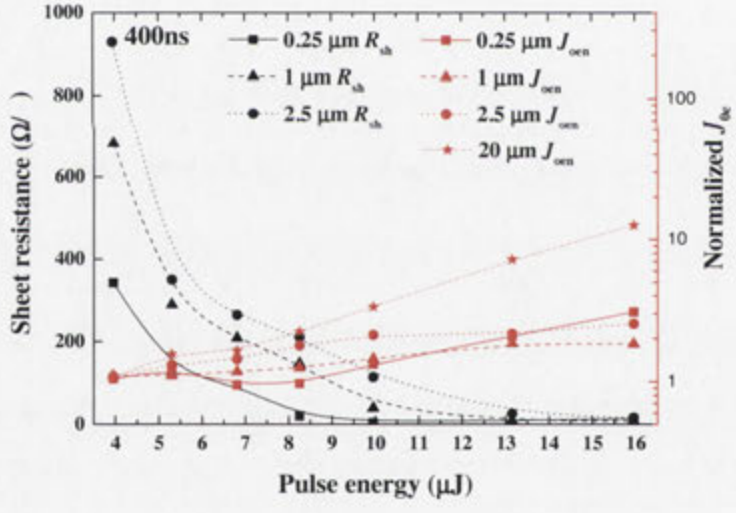

Fig. 63 4PP and PL results of the bare silicon sample irradiated with pulses of 400 ns pulse duration. Same plot setting is used for this figure as in Fig. 61.

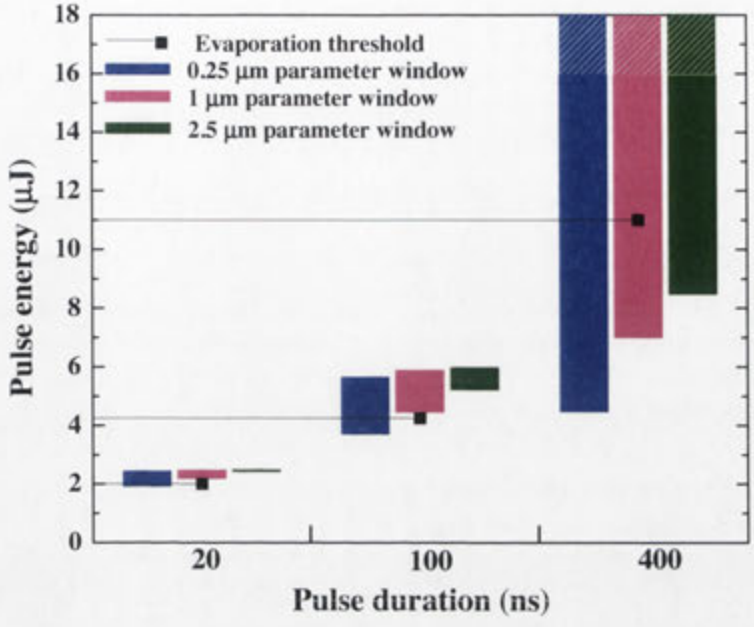

Fig. 64 Parameter windows and the simulated evaporation thresholds for different pulse durations of 20, 100 and 400 ns. The parameter windows are defined as the range of pulse energy between the damage threshold (upper end of the colour bar) and the doping threshold (lower end of the colour bar). The pulse energies corresponding to the doping thresholds (R_{sh} = 200 Ω/□) and to the damage threshold (J_{0en} = 4) are calculated by Piecewise cubic Hermite interpolation (PCHIP) [229] based on the data in Fig. 61 to Fig. 63. For 400 ns pulse duration, all the experimental data are below the assigned damage threshold. Therefore, patterned color bars, starting from the maximum pulse energies used in the experiment, extend to the boundary of the figure to indicate potentially higher damage thresholds.

Inspection of the J_{0en} data shows the following trends for the various process parameters:

- **Pulse energy**: for low pulse durations, there is a sharp transition with increasing pulse energy from little or no damage (J_{0en} ~1) to a large amount of damage (J_{0en} > 10), while at higher pulse durations, the increase of J_{0en} with pulse energy is more gradual. The slight dip of J_{0en} below 1 for some pulse energies could be due to dopant redistribution, which would be expected to lead to a slight decrease in J_{0e}.

- **Pulse duration**: Longer pulse durations lead to larger parameter windows where good doping is achieved with little damage. In addition, the defect formation mechanism appears to be dependent on pulse duration. Specifically, for 400 ns pulse duration, J_{0en} is evidently higher for the case of separated dots (20 μm separation), especially at higher pulse energies. In contrast, for 20ns pulse duration, pulse distance has little effect on damage, except for the case of high pulse energies, where separated dots lead to a lower J_{0en} than lines. Hence, in some circumstances it appears that multiple pulses with long pulse duration actually result in a reduction in damage, rather than an increase. This effect might have an influence on the post annealing process, as will be discussed in Section 6.7.
- **Pulse distance**: Lower pulse distances (lower scan speeds) lead to greater doping, but with some exceptions as discussed in the previous paragraph, pulse distance generally has no significant impact on J_{0en} at low or medium pulse energies. Thus, the constant melting and recrystallization of the silicon does not appear to lead to increased defect generation. At high pulse energy, evaporation of silicon becomes significant. This effect will be discussed in more detail in Section 6.6.

6.5 The influence of dielectric films

Figures 65 to 67 compare the J_{0en} results of the different dielectrics (including bare silicon) for all the combinations of laser parameters. For clarity and ease of interpretation, only the results for certain representative dielectrics are shown, with other dielectric films showing similar results. Results are shown for PECVD SiN_x film A (representative of all PECVD SiN_x films) and SiO_2 (representative of Al_2O_3 and Al_2O_3/TiO_2 stacks).

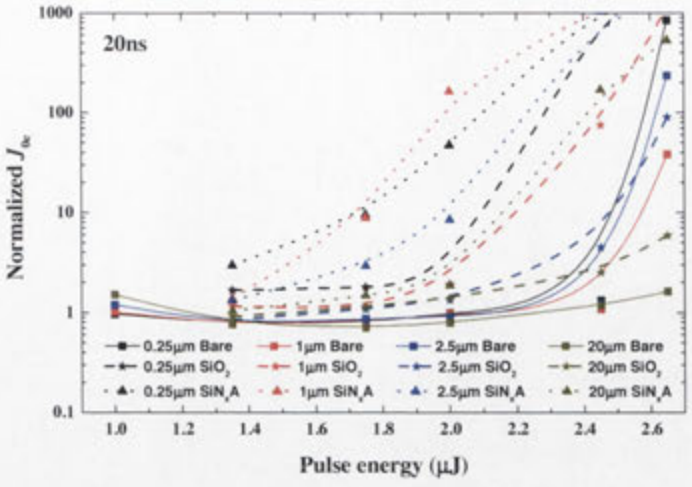

Fig. 65 The influence of dielectric films on J_{0cn} of samples irradiated with pulses of 20 ns duration. The results processed by different pulse distances are illustrated by different colours. For same pulse distance, different marks and line styles are used to distinguish different dielectric films.

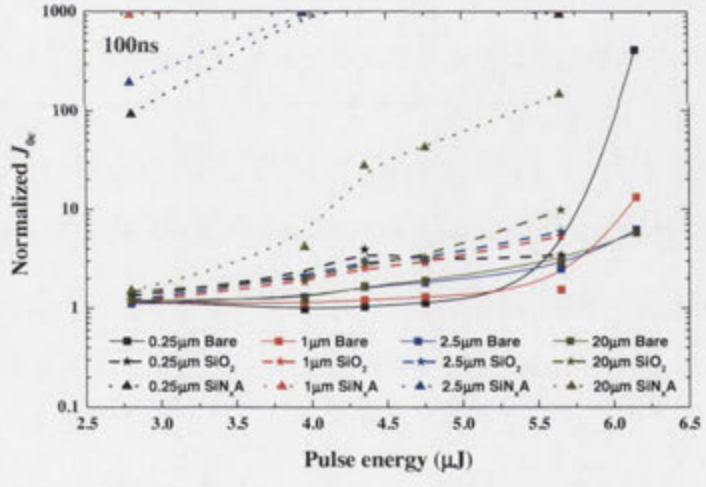

Fig. 66 The influence of dielectric films on J_{0cn} of samples irradiated with pulses of 100 ns duration. The results processed by different pulse distances are illustrated by different colours. For same pulse distance, different marks and line styles are used to distinguish different dielectric films.

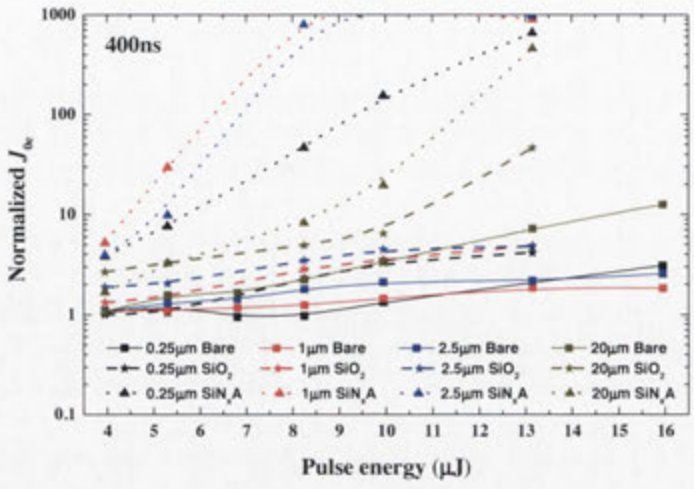

Fig. 67 The influence of dielectric films on J_{0en} of samples irradiated with pulses of 400 ns duration. The results processed by different pulse distances are illustrated by different colours. For same pulse distance, different marks and line styles are used to distinguish different dielectric films.

It can be seen that, for the dielectric films studied, the presence of a dielectric always degrades the silicon surface compared to bare silicon samples. However, the amount of degradation caused by the different dielectrics varies substantially. SiO_2, Al_2O_3 and Al_2O_3/TiO_2 result in much less degradation than the SiN_x films. The reason why SiN_x causes significantly more damage than other dielectrics is still under investigation.

The degradation caused by dielectrics is likely to be related to thermal expansion mismatch between the silicon and the dielectric films, as previously reported by other investigators. This mismatch contributes significantly to the formation of defects at high temperatures, such as voids adjacent to the laser processed areas and dislocations at the interface between the melted and solid regions [63,205]. Thus, the parameter window is significantly narrowed in the presence of dielectric films or stacks but, for suitable films, it is not eliminated (it is still possible to obtain $J_{0en} < 4$ for parameters which also yield $R_{sh} < 200$ on bare test samples). Several other observations can be made:

- The variation of J_{0en} with pulse energy is qualitatively similar for the samples capped with dielectrics (with the exception of the SiN_x samples which display extremely high J_{0en} values) as for bare silicon; however, in most cases the onset of severe degradation occurs at lower pulse energies.
- Pulse distance has no clearly discernible impact on J_{0en} for short pulse durations (20ns), but results in a decrease in J_{0en} for longer pulse durations. This observation extends to the case of isolated laser dots (20 μm pulse separation). Hence, again, repeated pulses with long pulse duration appear to be able to repair some of the crystal damage introduced by the first pulse or pulses.

The interpretation of the data presented in Fig. 65 to Fig. 67 neglects the possible impact of the changed optical properties on the laser process. The presence of the films will serve to decrease the sample reflectance when initially illuminated by the laser. For laser lines created using short pulse distances, each laser pulse only irradiates a small area that was not irradiated by the previous pulse, and given the Gaussian beam shape, the newly irradiated area will experience a relatively low irradiation intensity. The dielectric is likely to be fully removed before the peak of the laser pulse irradiates this area. For long pulse distances or non-overlapping lines, the effect may be more significant. Crudely, the maximum impact of the presence of the dielectric film on the energy absorbed by the silicon can be estimated by assuming completely uniform irradiation and calculating the additional energy absorbed with each pulse, given the area of overlap between successive pulses. For the lowest scan speed (0.25 μm), the area of overlap is ~98.4 %. Assuming zero reflection at 532 nm with the dielectric film, and 37% reflection for bare silicon, the total additional energy absorbed with the dielectric amounts to only 0.9 %. Hence, for low scan speeds, the optical effect of the dielectric film can be neglected. At higher scan speeds, a significant optical effect cannot be excluded but is difficult to confirm, since it is not known how the optical properties of the silicon/dielectric surface change as the surface rapidly heats during each laser pulse.

6.6 Relationship between damage and evaporation thresholds

An interesting finding during this study was that the sharp increase of J_{0en} of bare silicon samples occurred at the same pulse energy where a marked surface topographic change was observed, which suggests the onset of ablation or substantial silicon evaporation. This observation also applies to the samples capped with dielectric films (except SiN_x films) where J_{0en} increases to a high value (> 10), although the silicon surface topographic change is not as easily observable as on the bare silicon samples due to the presence of dielectric films. To investigate the relationship between the onset of high J_{0en} (characterized by the damage threshold) and the evaporation threshold of silicon (defined as the point where some of the silicon melt reaches boiling point during laser irradiation), simulations of single pulses with different pulse durations and pulse energies were done using the simulation program developed by Fell [80] using both the Knudsen [53] and Enthalpy [54] evaporation models. The results are shown in Fig. 64. Since the melt thresholds predicted by the two models are nearly identical, only one data point is shown for each pulse duration in Fig. 64. It can be seen that the damage threshold always appears to be somewhat higher than the evaporation threshold. This difference might be caused by systematic error (such as the error in the estimation of the width of the Gaussian laser beam) experiment and simulation, but it is also possible that the damage threshold is indeed somewhat higher than the evaporation threshold. The evaporation threshold may need to be exceeded by a certain amount (dependent on pulse duration and other parameters) before turbulence in the melt becomes sufficient to lead to the introduction of significant damage upon cooling. From the results it is, however, possible to state with some confidence, that substantial damage is not introduced during laser melting of bare silicon at least until the evaporation threshold is reached.

6.7 Impact of annealing

The observation that thermal annealing in a nitrogen gas (N_2) environment can recover some of the laser induced defects has been reported by previous researchers, although the mechanism behind the recovery is still unknown [70,71,230,231]. In the study about the effects of pulsed laser irradiation on the SiO_2/silicon interface, Deshmukh *et al.* [230] found that 30 min, 1150 °C N_2 annealing after laser processing can reduce the surface state density, decrease the oxide charge, and increase the lifetime. Parker *et al.* [70,71] investigated the leakage current for diodes, transistor gains, and metal-oxide-semiconductor (MOS) capacitance-voltage (CV) lifetime after laser scanning and after 30 min thermal annealing at various temperatures in N_2. It was found that the laser induced defects were stable for subsequent thermal annealing up to 400 °C but were almost completely removed at 800 °C. Ametowobla [231] also reported lifetime recovery after 600 °C N_2 annealing (annealing time was not reported) for a sample that had experienced 16 laser-melting cycles, while opposite results were observed if small numbers of melting cycles were used.

In order to investigate the impact of annealing, most of the group A samples (except SiN_xB and SiN_xC) were annealed in N_2 at 600 °C for 30 minutes. Subsequently, PL measurements were repeated. After annealing, a few samples became unusable due to a degradation in the uniformity of the PL images of the background (unprocessed) regions. This degradation was chiefly observed on samples processed with 20 ns pulse duration and SiO_2 samples. The reason for the degradation is currently unknown. As a control sample of Group A without any laser processing was also subjected to the annealing process without any noticeable lifetime change, it is unlikely that the uniformity degradation is a result of contamination of the annealing furnace used. Also, because the annealing temperature was only 600 °C, the diffusion profile was unlikely to be affected. These samples with significant uniformity degradation are excluded from the below analysis.

Comparing the PL images before and after annealing, as shown in Fig. 68, it can be seen that there is a clear improvement in the electronic quality of several of the laser processed regions.

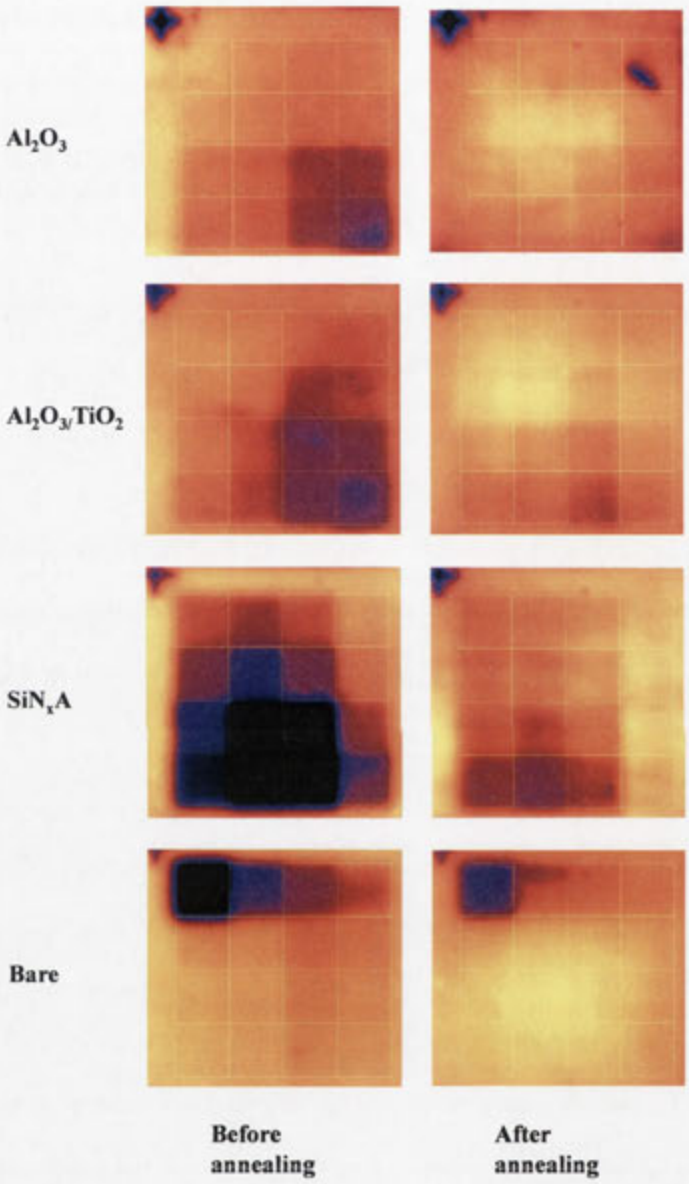

Fig. 68 PL images of some laser processed samples (which initially had different dielectric films) before and after 30 min 600 °C N_2 anneal.

It is important to note that, before annealing, the samples were stored for several months. The PL system was modified during this period. The PL image pixel resolution, i.e. the magnification, changed from 24 μm/pixel to 21 μm/pixel. Further,

the incident photon flux at the same PL setting was found to be slightly reduced possibly due to a degradation of the laser source of the PL instrument. In order to enable a comparison of the PL images before and after the change of the measurement conditions, a correction factor needs to be applied to the PL image before the change as below:

$$PL_{before-corrected} = C \times PL_{before} \ , \tag{6-2}$$

where PL_{before} is the PL signal before annealing (also before the measurement condition change), and $PL_{before-corrected}$ is the corrected PL signal before anneal that can be directly compared with the PL signal after anneal PL_{after} (also after measurement conditions change). C is the correction factor given by

$$C = C_r \times C_F \ , \tag{6-3}$$

$$C_r = (\frac{r_{after}}{r_{before}})^2 \ , \tag{6-4}$$

$$C_F = \frac{F_{after}}{F_{before}} \ , \tag{6-5}$$

where C_r and C_F are the correction factors correlated to the change of the magnification and incident photon flux respectively, r_{before} and r_{after} are the pixel resolutions of the PL images before and after measurement conditions change respectively, and F_{before} and F_{after} are the incident photon fluxes measured for each sample before and after anneal respectively.

It is worth mentioning the reason why C_F is a simple ratio of the incident photon fluxes:

$$I_{PL} = ABpn \ , \tag{6-6}$$

$$G = \frac{F}{W} = R = \frac{J_{eff}}{q}\left(\frac{pn}{n_i^2} - 1\right) \approx \frac{J_{eff}}{qn_i^2} pn \ , \tag{6-7}$$

where I_{PL} is the local PL signal, A is a scaling factor which takes into account the fact that in most cases the pixel count is measured only in relative units, G is the generation rate, R is the recombination rate, F is the incident photon flux. J_{eff} is the local effective recombination current refactor over the sample thickness, including the recombination contributions from surface, bulk and diffused regions. Since high resistivity wafers and high PL incident photon fluxes were used, the samples were all at high injection level in the PL measurements. As discussed in Section 3.3.1, therefore, J_{eff} cannot be regarded as an injection independent constant. However, considering the maximum variation of the F in the experiment is less than 3%, it is still reasonable to assume J_{eff} constant for all PL measurements in this experiment, which can significantly simplify the data analysis.

Substituting Eq. (6-7) into (6-6), we can have

$$I_{PL} \approx \frac{qn_i^2}{J_{eff}W} F \ . \tag{6-8}$$

Therefore, the PL signal is roughly linear proportional to the incident photon flux.

After applying the above data correction, the background PL signal of each sample measured in the same place in the PL images measured both before and after annealing was firstly analysed to check whether the background degraded after anneal. It was found the background PL signals generally increased after anneal (average ~7.6 %), except for the two wafers previously coated with AL_2O_3/TiO_2. The annealing temperature is only 600 °C, so the diffusion profile is unlikely to be affected. The reason for the general increase of the background PL signal after anneal is unknown.

In order to suppress the influence from the change of the unprocessed regions within the measured patterns but to highlight the change from the laser-processed regions, the

normalized PL signals (normalised to the unprocessed background) were used for quantitative comparison. In order to make the comparison reliable, the background signal is measured in the same place in the PL images measured both before and after annealing.

As Al_2O_3, and Al_2O_3/TiO_2 stacks showed similar results, only the results of bare samples, Al_2O_3 and SiN_xA are presented in Fig. 69 to Fig. 72. The bare sample results are shown in each figure as a reference.

It is interesting to note that after annealing some of the normalized PL data points have values slightly larger than 1, which would seem to indicate a higher electronic quality (lower J_{0e}) in the laser processed region than in the unprocessed region. Since normalised PL values >1 are measured also on samples where the dielectric film did not contain any dopant source (i.e. Al), this observation cannot be solely the result of increased doping. Rather, a slight uniformity degradation of the background PL signal after anneal is more likely responsible for the >1 normalised PL values. This non-uniformity introduces uncertainties and errors in the data analysis. Moreover, it is difficult to give an accurate estimation of the uncertainties. Since the maximum normalized PL of all the data is less than 1.14, 14 % might be used as rough uncertainty estimation. Although there are uncertainties and errors caused by non-uniformity, the non-uniformity is essentially random, so the conclusion obtained from the observation of the trend of a series of data rather than a signal data point should be still reliable. Some interesting and reliable observations are:

- The N_2 anneal treatment generally improves the PL signal ratio (likely to be due to a reduction in defect density) for almost all the samples. In several cases, the PL signal after annealing shows no observable degradation compared to the background (within the considerable error of the measurements).
- The most marked increase is observed for high pulse energies, where PL

intensities before annealing are low and there is a trend (in the pre-anneal data) of a reduction of PL intensity with increase in pulse energy. Except the data of bare silicon samples processed at long pulse duration (400 ns), and high pulse energy (>15 μJ) shows a decrease of the normalized PL signal at 0.25 μm pulse distance after anneal, but an increase at 1 μm pulse distance, and a further increase for larger pulse distances..

- The extremely high degradation caused by SiN_x was significantly reduced after annealing, which enables SiN_x to be put back on the candidate list of passivation films for high efficiency laser doped solar cells.

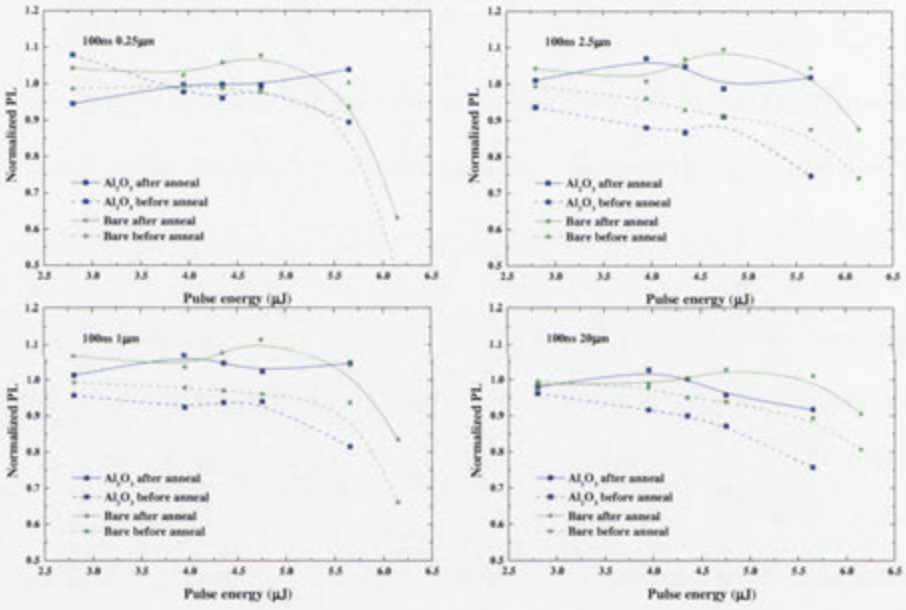

Fig. 69 Comparison of the normalized PL signal before and after anneal of Al_2O_3 samples processed at 100 ns pulse duration. The data of bare samples processed under the same conditions are given as a reference.

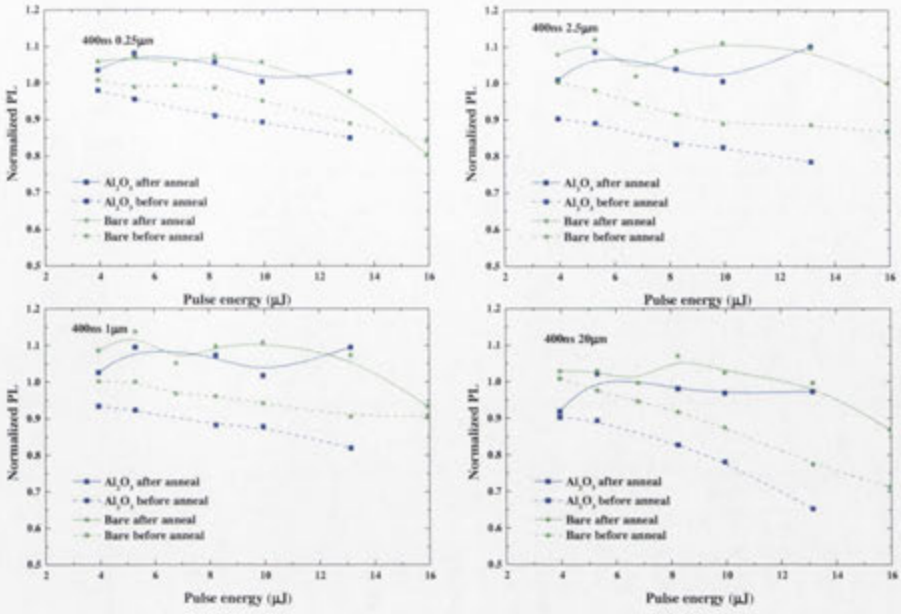

Fig. 70 Comparison of the normalized PL signal before and after anneal of Al_2O_3 samples processed at 400 ns pulse duration.

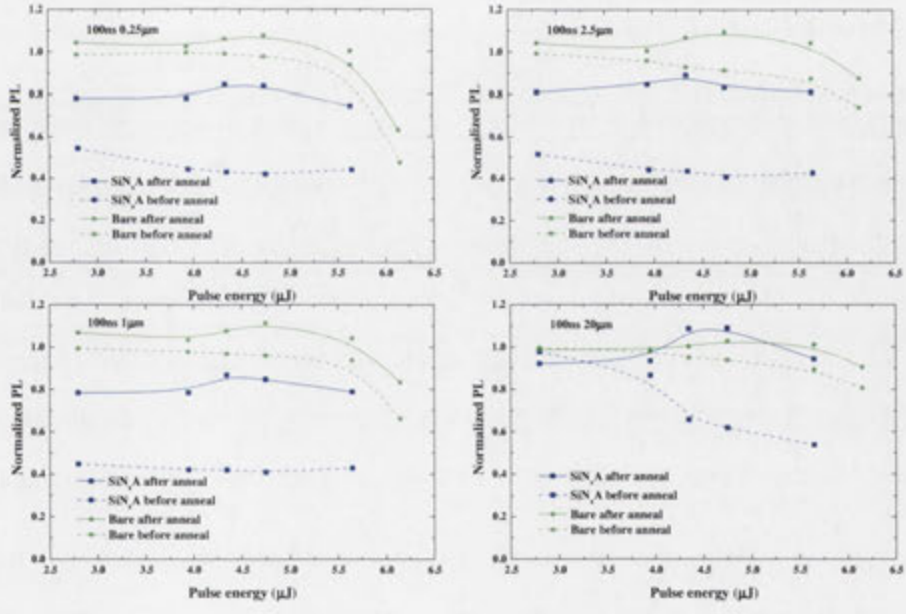

Fig. 71 Comparison of the normalized PL signal before and after anneal of SiN_x samples processed at 100 ns pulse duration.

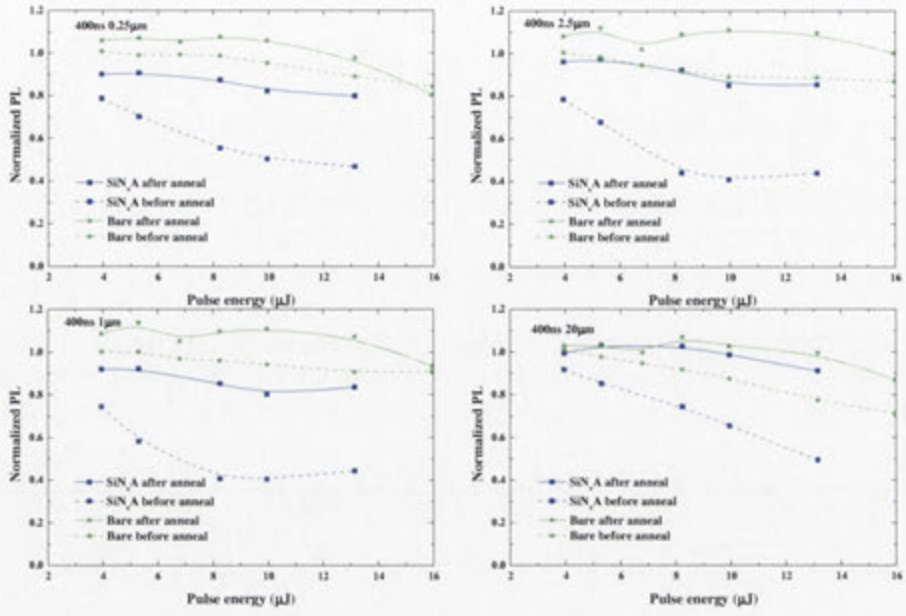

Fig. 72 Comparison of the normalized PL signal before and after anneal of SiN_x samples processed at 400 ns pulse duration.

6.8 Chapter summary

In this chapter, the impact of thermal effects and the presence of dielectric films on the electronic quality of laser processed silicon was investigated, by applying laser processing to already diffused silicon samples, without the use of a laser doping source. Analysis of PL images following laser processing, together with numerical modelling, allows determination of the recombination parameters for the laser processed regions. The impact of laser parameters on doping (more generally the melting of silicon) was assessed separately using silicon samples with spin-on dopant and 4PP measurements.

For bare silicon samples, the repeated silicon melting and recrystallization was found not to introduce significant additional damage provided the evaporation threshold is not exceeded, thus creating a relatively wide window in which silicon melting of sufficient duration and depth is achieved to allow heavy doping (sufficient silicon melting) while retaining good electronic properties, particularly for long pulse durations of around 400 ns. However, the presence of a dielectric film or stack on top

of the silicon always resulted in additional recombination compared to the bare silicon case. Amongst the studied dielectrics, PECVD SiN_x films resulted in particularly severe degradation compared to the oxides SiO_2, Al_2O_3 and Al_2O_3/TiO_2. For these oxides, the additional damage could be limited to acceptable levels for a range of laser parameters; however, the onset of severe damage occurred at lower pulse energies than for the corresponding case in the absence of a dielectric film. The impact of repeated, closely overlapping pulses was found to depend on pulse duration. For long (400 ns) pulses, repeated pulses resulted in a decrease in damage, while for short pulse durations (20 ns) single pulse leaded to much lower degradation. In all cases, repeated pulses resulted in greater dopant incorporation.

Comparison of experimental results of bare silicon samples with numerical modelling of the evaporation threshold of silicon revealed that the damage threshold – the pulse energy at which J_{0e} of the laser processed region exceeds 4 times the value of J_{0e} of the unprocessed region – occurs at a slightly higher value than the evaporation threshold. This supports the conclusion that the melting and recrystallization of silicon during laser processing does not significantly degrade the electronic properties; rather, it is the additional stresses due to thermal mismatch and other effects resulting from the presence of a dielectric film, or the turbulence and violent movement of the melt once the evaporation threshold is exceeded, that result in severe degradation.

Combining the PL results and 4PP measurement of laser-doped samples, it is demonstrated that high dopant incorporation and low recombination (for highly recombining surfaces in the presence of boron doping) can fundamentally exist at the same time, particularly when samples are processed using long pulse duration and small pulse distance laser pulses.

Last, the N_2 anneal treatment is proved to be an effective way to reduce both the laser and dielectric induced defects.

7 Summary and further work

7.1 Summary

This thesis has explored three challenging problems associated with the application of laser doping to the fabrication of locally doped features for silicon solar cells:

1. The lack of a widely-accessible, fast and inexpensive method for characterising laser-doped regions;
2. The possibly high recombination at the silicon/dielectric interface in the vicinity of laser-doped regions because of either the existence of exposed and undoped regions, or the passivation degradation of the dielectrics near the laser-opened dielectric window edges;
3. The possible degradation of the quality of laser-doped regions, which may render the achievement of high cell efficiencies impossible or very challenging.

For **Problem 1**, a technique — secondary electron microscopy dopant contrast imaging (SEMDCI) — based on the dopant contrast that can be observed in SEM images is explored and applied. SEMDCI can be used for a large range of different dopant sources and different laser methods, and good dopant contrast can be obtained under a relatively wide range of microscope parameters. The reliability of the SEMDCI technique was confirmed by the comparing it with EBIC, ECV and TLM. For p-type samples, a quantitative relationship between the contrast and doping concentration has been established, albeit over a limited range of dopant concentrations and with still considerable error. SEMDCI was shown to be a powerful technique for laser doping applications, including detecting the p-n junction boundary, obtaining qualitative and quantitative dopant distributions, observing materials interactions during laser processes, characterizing the top surface doping profiles, and evaluating the edge of the laser-opened dielectric film window.

The observation of the interaction between SOD, SiN_x, and silicon during the laser doping process shows that the detachment of the SOD film from the dielectric during laser irradiation may influence the doping process, by influencing the optics of the SOD/dielectric/silicon stack and by altering the processes by which dopant is incorporated into the melted silicon. The fact that doping is achieved even in cases where the SOD film is already detached from the dielectric prior to silicon melting and doping lends weight to the idea that doping of the silicon occurs, at least in this case, from the liquid or gas phase of the SOD. The difference in the formation of floccules observed between single and multiple, overlapping lines may indicate that the detachment of the SOD film requires a certain period of time to take place. Furthermore, it is likely that the SiN_x film is incorporated into the melted silicon, potentially introducing recombination active defects.

For **problem 2**, the possible gap between laser-doped region and the edge of the dielectric window opened by laser is characterized by SEMDCI either with (direct method) or without (indirect method) the dielectrics remaining on the top surface. The latter requires the assistance of TMAH etch. Both methods are shown to provide useful information. The direct method is superior in terms of convenience of sample preparation, and wide applicability for different dielectrics, while the indirect method automatically detects the dielectric edge without the need of a high magnification image.

The influence of the SiO_2/SiN_x stack thickness on laser doping has been investigated using the direct method and also been evaluated through TLM. Over the range of laser parameters studied, the thin stack generally results in lower line resistance and contact resistivity, while the thick stack offers a smaller gap distance. An increase in laser pulse energy or pulse distance generally results in worse performance regarding the studied properties; in other words, higher contact resistivity and line resistance, and larger (positive) gap distance. Fundamentally, a problem of positive gaps was identified and found to be present in most of the investigated parameter range.

However, optimization of the laser parameters and dielectric film conditions has been shown capable of potentially overcoming this problem. The samples capped with thick dielectric stacks processed at low pulse energies and with low pulse overlap offer the optimal results over the parameter range studied. It should be emphasized that the scope of the current study is restricted. Further considerations, such as the optimization of dielectric stack optical properties, are also important for designing high efficiency solar cells.

The exposed undoped gap discussed above can be regarded as an extreme case of the possible passivation degradation of the dielectrics in the vicinity of the laser opened window. A more general experimental method of this problem is proposed by comparing the localized effective J_0 of the laser-doped region at different passivation and re-passivation steps. Unfortunately, to date attempts to implement this method have been unsuccessful due to inappropriate choice of the passivation film.

In the last part of the thesis, **problem 3** is investigated. The repeated silicon melting and recrystallization was found not to introduce significant additional damage provided the evaporation threshold is not exceeded, thus creating a relatively wide window in which silicon melting of sufficient duration and depth is achieved to allow heavy doping (sufficient silicon melting) while retaining good electronic properties, particularly for long pulse durations of around 400 ns. However, the presence of a dielectric film or stack on top of the silicon always resulted in additional recombination compared to the bare silicon case. Amongst the studied dielectrics, PECVD SiN_x films resulted in particularly severe degradation compared to the oxides SiO_2, Al_2O_3 and Al_2O_3/TiO_2. For these oxides, the additional damage could be limited to acceptable levels for a range of laser parameters; however, the onset of severe damage occurred at lower pulse energies than for the corresponding case in the absence of a dielectric film. The impact of repeated, closely overlapping pulses was found to depend on pulse duration. For long (400 ns) pulses, repeated pulses resulted in a decrease in damage, while for short pulse durations (20 ns) single pulse led to much

lower degradation. In all cases, repeated pulses resulted in greater dopant incorporation. It is demonstrated that high dopant incorporation and low recombination (for highly recombining surfaces in the presence of boron doping) can fundamentally exist at the same time, particularly when samples are processed using long pulse duration and small pulse distance laser pulses. The 600 °C N_2 anneal treatment is proved to be an effective way to reduce the laser and dielectric induced defects.

7.2 Suggestion for possible future work

During this thesis a number of areas were identified for future work:

1. Much work needs to be done to increase the accuracy of the SEMDCI for quantitative analysis of p-type doping, for example, including more SEM parameters into consideration and setting up a more stable sample cleaving process.
2. In order to make SEMDCI a routine line resistance analysis tool, a user-friendly image analysis software is needed to be developed.
3. The experimental method suggested to analyse the possible dielectric degradation is of great interest now, considering the N_2 anneal was found to be able to significantly reduce the SiN_x induced degradation.
4. The thermal and dielectric induced degradation experiment should be applied to n^+ regions to test whether the defect is doping type dependant.
5. The reason of the SiN_x induced degradation requires more investigation.

List of Publications

Publications arising from the work in this thesis:

Journal Papers:

1. L. Xu, K. Weber, S.P. Phang, A. Fell, F. Brink, D. Yan, X. Yang, E. Franklin, and H. Chen, "Secondary electron microscopy dopant contrast image (SEMDCI) for laser doping," *IEEE Journal of Photovoltaics*, vol. 3, pp. 762-768, 2013.
2. L. Xu, K. Weber, A. Fell, Z. Hameiri, S.P. Phang, X. Yang, and E. Franklin, "The impact of SiO_2/SiN_x stack thickness on laser doping of silicon solar cell," *IEEE Journal of Photovoltaics*, vol. 4, pp. 594-600, 2014.
3. L. Xu, K. Weber, A. Fell, X. Yang, E. Franklin, and A. Thomson, "The influence of thermal effects and dielectric films on the electronic quality of p^+-doped silicon processed by nanosecond Laser," *IEEE Journal of Photovoltaics*, vol. 4, pp. 1220-1227, 2014.

Conference papers:

4. L. Xu, K. Weber, S.P. Phang, A. Fell, F. Brink, and E. Franklin, "Dopant mapping for laser doping using secondary electron image," presented at *the 27th EUPVSEC*, Frankfurt, Germany, 2012, pp. 740 - 743.
5. L. Xu, Z. Hameiri, K. Weber, and X. Yang, "Comparison between secondary electron microscopy dopant contrast image (SEMDCI) and electron beam induced current (EBIC) for laser doping of crystalline silicon," presented at the 2014 *SiliconPV*, 's-Hertogenbosch, The Netherlands, 2014, pp. 179-185.
6. L. Xu, K. Weber, X. Yang, A. Fell and E. Franklin, "The impact of N_2 anneal on laser processed silicon," accepted by the 2015 *SiliconPV*, Konstanz, Germany, 2015

Other publications:

7. X. Yang, D. Macdonald, A. Fell, A. Shalav, L. Xu, D. Walter, T. Ratcliff, E. Franklin, K. Weber, and R. Elliman, "Imaging of the relative saturation current density and sheet resistance of laser-doped regions via photoluminescence," *Journal of Applied Physics*, vol. 114, p. 053107, 2013.
8. X. Yang, A. Fell, L. Xu, E. Franklin, S. Surve, D. Macdonald, E.-C. Wang, N. Vago, K. Weber, H. Nishimura, and T. Fuyuki, "Laser chemical processing (LCP) doping formed through differenct dielectric layers," presented at the *28th EUPVSEC*, Munich, Germany, 2013, pp. 1057-1060.

9. X. Yang, R. Müller, A. Shalav, L. Xu, W. Liang, R. Zhang, Q. Bi, K. Weber, D. Macdonald, and R. Elliman, "Boron implanted, laser annealed p+ emitter for n-type interdigitated back-contact solar cells " presented at the 2014 *SiliconPV*, 's-Hertogenbosch, The Netherlands, 2014, pp. 320-325.
10. X. Yang, R. Müller, L. Xu, K. Weber, A. Fell, and E. Franklin, "Ion implanted, laser annealed p^+ and n^+ regions: a potential solution for industrially feasible high efficiency n-type interdigitated back-contact solar cells," *IEEE Journal of Photovoltaics*, vol. 5, pp. 87-93, 2015.

Bibliography

[1] J. Hansen, M. Sato, R. Ruedy, K. Lo, D. W. Lea, and M. Medina-Elizade, "Global temperature change," *Proceedings of the National Academy of Sciences,* vol. 103, pp. 14288-14293, 2006.

[2] J. Hansen, R. Ruedy, M. Sato, and K. Lo, "Global surface temperature change," *Reviews of Geophysics,* vol. 48, p. RG4004, 2010.

[3] H. John, "Global warming," *Reports on Progress in Physics,* vol. 68, p. 1343, 2005.

[4] R. F. Service, "Is it time to shoot for the sun?," *Science,* vol. 309, pp. 548-551, July 22, 2005 2005.

[5] (2005) The energy challenge for achieving the Millennium Development Goals. *UN-Energy.*

[6] J. O. Blackburn and S. Cunningham, "Solar and nuclear costs—The historic crossover," *North Carolina Waste Awareness & Reduction Network (NC WARN),* 2010.

[7] E. Martinot, "Renewables 2005: Global status report," Worldwatch Institute Washington, DC2005.

[8] A. Jäger-Waldau, "PV Status Report 2013," Institute for Energy and Transport, Renewable Energy Unit, European Commission 2013.

[9] A. W. Blakers, A. Wang, A. M. Milne, J. Zhao, and M. A. Green, "22.8% efficient silicon solar cell," *Applied Physics Letters,* vol. 55, pp. 1363-1365, 1989.

[10] D. De Ceuster, P. Cousins, D. Rose, D. Vicente, P. Tipones, and W. Mulligan, "Low cost, high volume production of >22% efficiency silicon solar cells," presented at the 22nd EUPVSEC, Milan, Italy, 2007, pp. 816-819.

[11] T. F. Deutsch, D. J. Ehrlich, D. D. Rathman, D. J. Silversmith, and R. M. Osgood, "Electrical properties of laser chemically doped silicon," *Applied Physics Letters,* vol. 39, pp. 825-827, 1981.

[12] T. F. Deutsch, J. C. C. Fan, G. W. Turner, R. L. Chapman, D. J. Ehrlich, and R. M. Osgood, "Efficient Si solar cells by laser photochemical doping," *Applied Physics Letters,* vol. 38, pp. 144-146, 1981.

[13] R. Stuck, E. Fogarassy, J. C. Muller, M. Hodeau, A. Wattiaux, and P. Siffert, "Laser-induced diffusion by irradiation of silicon dipped into an organic solution of the dopant," *Applied Physics Letters,* vol. 38, pp. 715-717, 1981.

[14] G. B. Turner, D. Tarrant, G. Pollock, R. Pressley, and R. Press, "Solar cells made by laser-induced diffusion directly from phosphine gas," *Applied Physics Letters,* vol. 39, pp. 967-969, 1981.

[15] K. G. Ibbs and M. L. Lloyd, "Ultra-violet laser doping of silicon," *Optics and Laser Technology,*

vol. 15, pp. 35-39, 1983.

[16] K. G. Ibbs and M. L. Lloyd, "Laser doping: Bipolar structures in silicon," *Optics & Laser Technology,* vol. 16, pp. 37-39, 1984.

[17] Z. Hameiri, L. Mai, T. Puzzer, and S. R. Wenham, "Influence of laser power on the properties of laser doped solar cells," *Solar Energy Materials and Solar Cells,* vol. 95, pp. 1085-1094, 2011.

[18] D. K. Schroder and D. L. Meier, "Solar cell contact resistance—a review," *IEEE Transactions on Electron Devices,* vol. 31, pp. 637-647, 1984.

[19] V. L. Rideout, "A review of the theory and technology for ohmic contacts to group III–V compound semiconductors," *Solid-State Electronics,* vol. 18, pp. 541-550, 1975.

[20] J. Bardeen, "Surface states and rectification at a metal semi-conductor contact," *Physical Review,* vol. 71, pp. 717-727, 1947.

[21] A. Cuevas, R. A. Sinton, N. E. Midkiff, and R. M. Swanson, "26-percent efficient point-junction concentrator solar cells with a front metal grid," *IEEE Electron Device Letters,* vol. 11, pp. 6-8, 1990.

[22] A. Cuevas, "Electrons and holes in solar cells with partial rear contacts," *Progress in Photovoltaics: Research and Applications,* vol. 22, pp. 764-774, 2014.

[23] A. Cuevas, "Geometrical analysis of solar cells with partial rear contacts," *IEEE Journal of Photovoltaics,* vol. 2, pp. 485-493, 2012.

[24] S. De Wolf, A. Descoeudres, Z. C. Holman, and C. Ballif, "High-efficiency silicon heterojunction solar cells: A review," *Green,* vol. 2, pp. 7-24, 2012.

[25] J. Bullock, D. Yan, and A. Cuevas, "Passivation of aluminium–n^+ silicon contacts for solar cells by ultrathin Al_2O_3 and SiO_2 dielectric layers," *physica status solidi (RRL) – Rapid Research Letters,* vol. 7, pp. 946-949, 2013.

[26] F. Feldmann, M. Bivour, C. Reichel, M. Hermle, and S. W. Glunz, "Passivated rear contacts for high-efficiency n-type Si solar cells providing high interface passivation quality and excellent transport characteristics," *Solar Energy Materials and Solar Cells,* vol. 120, Part A, pp. 270-274, 2014.

[27] A. Cuevas and Y. Di, "Misconceptions and misnomers in solar cells," *IEEE Journal of Photovoltaics,* vol. 3, pp. 916-923, 2013.

[28] K. Masuko, M. Shigematsu, T. Hashiguchi, D. Fujishima, M. Kai, N. Yoshimura, T. Yamaguchi, Y. Ichihashi, T. Mishima, N. Matsubara, T. Yamanishi, T. Takahama, M. Taguchi, E. Maruyama, and S. Okamoto, "Achievement of more than 25% conversion efficiency with crystalline silicon heterojunction solar cell," *IEEE Journal of Photovoltaics,* vol. 4, pp. 1433-1435, 2014.

[29] M. Taguchi, A. Yano, S. Tohoda, K. Matsuyama, Y. Nakamura, T. Nishiwaki, K. Fujita, and E. Maruyama, "24.7% record efficiency HIT solar cell on thin silicon wafer," *IEEE Journal of*

Photovoltaics, vol. 4, pp. 96-99, 2014.

[30] J. M. Fairfield and G. H. Schwuttke, "Silicon diodes made by laser irradiation," *Solid-State Electronics*, vol. 11, pp. 1175-1176, IN5-IN6, 1968.

[31] F. Harper and M. Cohen, "Properties of Si diodes prepared by alloying Al into n-type Si with heat pulses from a Nd: YAG laser," *Solid-State Electronics*, vol. 13, pp. 1103-1109, 1970.

[32] T. F. Deutsch, D. J. Ehrlich, D. D. Rathman, D. J. Silversmith, and J. R. M. Osgood, "Electrical properties of laser chemically doped silicon," *Applied Physics Letters*, vol. 39, pp. 825-827, 1981.

[33] E. Fogarassy, R. Stuck, J. Grob, and P. Siffert, "Silicon solar cells realized by laser induced diffusion of vacuum-deposited dopants," *Journal of Applied Physics*, vol. 52, pp. 1076-1082, 1981.

[34] R. T. Young, R. F. Wood, and W. H. Christie, "Laser processing for high-efficiency Si solar cells," *Journal of Applied Physics*, vol. 53, pp. 1178-1189, 1982.

[35] T. Bruton, N. Mason, S. Roberts, O. N. Hartley, S. Gledhill, J. Fernandez, R. Russell, W. Warta, S. Glunz, O. Schultz, M. Hermle, and G. Willeke, "Towards 20% efficient silicon solar cells manufactured at 60 MWp per annum," in *3rd World Conference on Photovoltaic Energy Conversion*, 2003, pp. 899-902 Vol.1.

[36] Z. Wang, P. Han, H. Lu, H. Qian, L. Chen, Q. Meng, N. Tang, F. Gao, Y. Jiang, J. Wu, W. Wu, H. Zhu, J. Ji, Z. Shi, A. Sugianto, L. Mai, B. Hallam, and S. Wenham, "Advanced PERC and PERL production cells with 20.3% record efficiency for standard commercial p-type silicon wafers," *Progress in Photovoltaics: Research and Applications*, vol. 20, pp. 260-268, 2012.

[37] D. Kray, N. Bay, G. Cimiotti, S. Kleinschmidt, N. Kösterke, A. Lösel, M. Sailer, A. Träger, H. Kühnlein, H. Nussbaumer, C. Fleischmann, and F. Granek, "Industrial LCP selective emitter solar cells with plated contacts," in *35th IEEE PVSC*, Honolulu, Hawaii USA, 2010, pp. 667-671.

[38] M. D. Abbott, "Advanced laser processing and photoluminescence characterisation of high efficiency silicon solar cells," PhD, School of Photovoltaic and Renewable Energy Engineering, University of New South Wales, Sydney, 2006.

[39] G. Stock, D. Bollmann, R. Buchner, G. Neumayer, and K. Haberger, "Ultra-flat pn junctions formed by solid source laser doping," *Applied Surface Science*, vol. 46, pp. 348-351, 1990.

[40] J. C. Wang, R. F. Wood, and P. P. Pronko, "Theoretical analysis of thermal and mass transport in ion-implanted laser-annealed silicon," *Applied Physics Letters*, vol. 33, pp. 455-458, 1978.

[41] R. O. Bell, M. Toulemonde, and P. Siffert, "Calculated temperature distribution during laser annealing in silicon and cadmium telluride," *Applied physics*, vol. 19, pp. 313-319, 1979.

[42] R. F. Wood and G. A. Geist, "Modeling of nonequilibrium melting and solidification in laser-irradiated materials," *Physical Review B*, vol. 34, pp. 2606-2620, 1986.

[43] R. Young and R. Wood, "Laser processing of semiconductor materials," *Annual Review of Materials Science*, vol. 12, pp. 323-350, 1982.

[44] R. F. Wood, C. W. White, and R. T. Young, *Semiconductors and semimetals* vol. 23, 1984. pp. 1-686.

[45] R. F. Wood and G. E. Giles, "Macroscopic theory of pulsed-laser annealing. I. Thermal transport and melting," *Physical Review B*, vol. 23, pp. 2923-2942, 1981.

[46] R. F. Wood, J. R. Kirkpatrick, and G. E. Giles, "Macroscopic theory of pulsed-laser annealing. II. Dopant diffusion and segregation," *Physical Review B*, vol. 23, pp. 5555-5569, 1981.

[47] C. White, P. Pronko, S. Wilson, B. Appleton, J. Narayan, and R. Young, "Effects of pulsed ruby-laser annealing on As and Sb implanted silicon," *Journal of Applied Physics*, vol. 50, pp. 3261-3273, 1979.

[48] C. White, S. Wilson, B. Appleton, and F. Young Jr, "Supersaturated substitutional alloys formed by ion implantation and pulsed laser annealing of group-III and group-V dopants in silicon," *Journal of Applied Physics*, vol. 51, pp. 738-749, 1980.

[49] R. Hull, *Properties of crystalline silicon*: INSPEC, 1999.

[50] D. H. Lowndes, R. F. Wood, and R. D. Westbrook, "Pulsed neodymium: yttrium aluminum garnet laser (532 nm) melting of crystalline silicon: Experiment and theory," *Applied Physics Letters*, vol. 43, pp. 258-260, 1983.

[51] S. Adachi, *Optical properties of crystalline and amorphous semiconductors*: Springer, 1999.

[52] M. O. Thompson, J. W. Mayer, A. G. Cullis, H. C. Webber, N. G. Chew, J. M. Poate, and D. C. Jacobson, "Silicon Melt, Regrowth, and Amorphization Velocities During Pulsed Laser Irradiation," *Physical Review Letters*, vol. 50, pp. 896-899, 1983.

[53] P. W. Atkins and J. d. Paula, *Physikalische chemie*, 2nd ed. Weinheim: VCH Verlagsgesellschaft, 1996. pp. 772-774.

[54] A. Miotello and R. Kelly, "Critical assessment of thermal models for laser sputtering at high fluences," *Applied Physics Letters*, vol. 67, pp. 3535-3537, 1995.

[55] J. Narayan, R. T. Young, R. F. Wood, and W. H. Christie, "p-n junction formation in boron-deposited silicon by laser-induced diffusion," *Applied Physics Letters*, vol. 33, pp. 338-340, 1978.

[56] R. T. Young, R. F. Wood, J. Narayan, C. W. White, and W. H. Christie, "Pulsed laser techniques for solar cell processing," *IEEE Transactions on Electron Devices*, vol. 27, pp. 807-815, 1980.

[57] R. T. Young, J. Narayan, R. D. Westbrook, and R. F. Wood, "Transmission electron microscopy and electrical properties measurements of laser doped silicon and GaAs," *AIP Conference Proceedings*, vol. 50, pp. 579-584, 1979.

[58] M. Ametowabla, A. Esturo-Breton, J. R. Kohler, and J. H. Werner, "Laser processing of

crystalline silicon solar cells," in *31st IEEE PVSC*, Lake Buena Vista, FL, USA, 2005, pp. 1277-1280.

[59] A. Esturo-Bretón, T. A. Wagner, J. R. Köhler, and J. H. Werner, "Laser doping for crystalline silicon solar cell emitters," in *13th Workshop on Crystalline Silicon Solar Cell Materials* Vail, 2003, pp. 186-89.

[60] P. M. Mooney, R. T. Young, J. Karins, Y. H. Lee, and J. W. Corbett, "Defects in laser damaged silicon observed by DLTS," *physica status solidi (a)*, vol. 48, pp. K31-K34, 1978.

[61] R. T. Young, J. Narayan, and R. F. Wood, "Electrical and structural characteristics of laser-induced epitaxial layers in silicon," *Applied Physics Letters*, vol. 35, pp. 447-449, 1979.

[62] S. Hopman, A. Fell, K. Mayer, C. Fleischmann, K. Drew, D. Kray, and F. Granek, "Study on laser parameters for silicon solar cells with LCP selective emitters," presented at the 24th EUPVSEC, Hamburg, Germany, 2009, pp. 1072-1076.

[63] Z. Hameiri, T. Puzzer, L. Mai, A. B. Sproul, and S. R. Wenham, "Laser induced defects in laser doped solar cells," *Progress in Photovoltaics: Research and Applications*, vol. 19, pp. 391-405, 2011.

[64] Z. Hameiri, "Laser-doped selective emitter and local back surface field solar cells with rear passivation," PhD, Centre for Photovoltaic Engineering, University of New South Wales, Sydney, 2010.

[65] R. T. Young, R. F. Wood, W. H. Christie, and G. E. Jellison, "Substrate heating and emitter dopant effects in laser-annealed solar cells," *Applied Physics Letters*, vol. 39, pp. 313-315, 1981.

[66] P. L. Liu, R. Yen, N. Bloembergen, and R. T. Hodgson, "Picosecond laser-induced melting and resolidification morphology on Si," *Applied Physics Letters*, vol. 34, pp. 864-866, 1979.

[67] S. de Unamuno and E. Fogarassy, "A thermal description of the melting of c- and a-silicon under pulsed excimer lasers," *Applied Surface Science*, vol. 36, pp. 1-11, 1989.

[68] H. Koichiro, K. Hiroshi, U. Keiichiro, and M. Yoshio, "Incorporation of oxygen into silicon during pulsed-laser irradiation," *Japanese Journal of Applied Physics*, vol. 19, p. L375, 1980.

[69] J. Jourdan, Y. Veschetti, S. Dubois, T. Desrues, and R. Monna, "Formation of Boron-doped region using spin-on dopant: investigation on the impact of metallic impurities," *Progress in Photovoltaics: Research and Applications*, vol. 16, pp. 379-387, 2008.

[70] D. L. Parker, F.-Y. Lin, S.-J. Zhu, D.-K. Zhang, and W. A. Porter, "Selective lifetime doping in silicon by laser scanning," *IEEE Transactions on Electron Devices*, vol. 29, pp. 1718-1722, 1982.

[71] D. L. Parker, F.-Y. Lin, S.-J. Zhu, D.-K. Zhang, and W. A. Porter, "A comparison of Nd:YAG fundamental and second-harmonic Q-switched laser-beam lifetime doping in single-crystal silicon," *IEEE Transactions on Electron Devices*, vol. 30, pp. 1322-1326, 1983.

[72] V. C. Lo, Y. W. Wong, H. C. Cho, Y. Q. Chen, S. M. Ho, P. W. Chan, and K. Y. Tong, "Excimer laser assisted spin-on doping of boron into silicon," *Semiconductor Science and Technology*, vol. 11, pp. 1285-1290, 1996.

[73] A. Fell, D. Kray, T. Wütherich, R. Müller, G. P. Willeke, and S. W. Glunz, "Simulation of phase changes and dopant diffusion in silicon for the manufacturing of selective emitters via laser chemical processing," presented at the 23rd EUPVSEC, Valencia, Spain, 2008, pp. 272-274.

[74] E. Fogarassy, R. Stuck, M. Toulemonde, D. Salles, and P. Siffert, "A model for laser induced diffusion," *Journal of Applied Physics*, vol. 54, pp. 5059-5063, 1983.

[75] R. Stuck, E. Fogarassy, J. J. Grob, and P. Siffert, "Solubility limit of impurities in silicon after laser induced melting," *Applied physics*, vol. 23, pp. 15-19, 1980.

[76] R. F. Wood, "Macroscopic theory of pulsed-laser annealing. III. Nonequilibrium segregation effects," *Physical Review B*, vol. 25, pp. 2786-2811, 1982.

[77] J. P. Garandet, "New determinations of diffusion coefficients for various dopants in liquid silicon," *International Journal of Thermophysics*, vol. 28, pp. 1285-1303, 2007.

[78] H. Kodera, "Diffusion coefficients of impurities in silicon melt," *Japanese Journal of Applied Physics*, vol. 2, p. 212, 1963.

[79] S. Toshiyuki and U. Setsuo, "Analysis of dopant diffusion in molten silicon induced by a pulsed Excimer laser," *Japanese Journal of Applied Physics*, vol. 26, p. L1208, 1987.

[80] A. Fell, "Modelling and simulation of laser chemical processing (LCP) for the manufacturing of silicon solar cells," Ph.D. dissertation, Fraunhofer Institute for Solar Energy Systems, Freiburg im Breisgau, 2010.

[81] S. R. Wenham and M. A. Green, "Self aligning method for forming a selective emitter and metallization in a solar cell," U.S. Patent No. 6,429,037, 6 Aug., 2002.

[82] G. Willeke and D. Kray, "A new route towards 50 μm thin crystalline silicon wafer solar cells," presented at the 17th EUPVSEC, Munich, Germany, 2001, pp. 1621-1624.

[83] D. Kray, A. Fell, S. Hopman, K. Mayer, M. Mesec, S. W. Glunz, and G. P. Willeke, "Progress in laser chemical processing (LCP) for innovative solar cell microstructuring and wafering applications," in *22nd EUPVSEC*, Milan, Italy, 2007, pp. 1227-1230.

[84] B. Richerzhagen and G. Delacre, "Complete model to simulate the thermal defocusing of a laser beam focused in water," *Optical Engineering*, vol. 35, pp. 2058-2066, 1996.

[85] D. Kray, A. Fell, S. Hopman, K. Mayer, G. P. Willeke, and S. W. Glunz, "Laser chemical processing (LCP)—A versatile tool for microstructuring applications," *Applied Physics A*, vol. 93, pp. 99-103, 2008/10/01 2008.

[86] J. H. Werner, J. Kohler, and A. Esturo-Breton, "Laser doping of solid bodies using a linear-focussed laser beam and production of solar-cell emitters based on said method," U.S. Patent No. US 2008/0026550 A1, 31 Jan., 2008.

[87] J. R. Köhler, M. Ametowobla, and A. Esturo-Breton, "Numerical modeling of pulsed laser doping of crystalline silicon solar cells," presented at the 20th EUPVSEC, München, Deutschland, 2005, pp. 1162 - 1165.

[88] P. Mei, R. A. Lujan, and J. B. Boyce, "Proximity laser doping technique for electronic materials " U.S. Patent No. 5,871,826, 16 Feb., 1999.

[89] P. Mei, J. Boyce, J. Lu, J. Ho, and R. Fulks, "Pulsed laser crystallization and doping for thin film transistors," *Journal of Non-Crystalline Solids*, vol. 266, pp. 1252-1259, 2000.

[90] R. Ferré, R. Gogolin, J. Müller, N. P. Harder, and R. Brendel, "Laser transfer doping for contacting n-type crystalline Si solar cells," *physica status solidi (a)*, vol. 208, pp. 1964-1966, 2011.

[91] D. Suwito, U. Jäger, J. Benick, S. Janz, M. Hermle, and S. W. Glunz, "Industrially feasible rear passivation and contacting scheme for high-efficiency n-type solar cells yielding a V_{oc} of 700 mV," *IEEE Transactions on Electron Devices*, vol. 57, pp. 2032-2036, 2010.

[92] J. Benick, B. Steinhauser, R. Müller, J. Bartsch, M. Kamp, A. Mondon, A. Richter, M. Hermle, and S. Glunz, "High efficiency n-type PERT and PERL solar cells," in *40th IEEE PVSC*, Denver, CO, USA, 2014, submitted.

[93] B. Steinhauser, U. Jäger, J. Benick, and M. Hermle, "PassDop rear side passivation based on Al_2O_3/a-SiC_x:B stacks for p-type PERL solar cells," *Solar Energy Materials and Solar Cells*, 2014,http://dx.doi.org/10.1016/j.solmat.2014.05.001.

[94] B. Steinhauser, M. b. Mansoor, U. Jäger, J. Benick, and M. Hermle, "Firing-stable PassDop passivation for screen printed n-type PERL solar cells based on a-SiN_x:P," *Solar Energy Materials and Solar Cells*, vol. 126, pp. 96-100, 2014.

[95] U. Besu-Vetrella, L. Pirozzi, E. Salza, G. Ginocchietti, F. Ferrazza, L. Ventura, A. Slaoui, and J. C. Muller, "Large area, screen printed silicon solar cells with selective emitter made by laser overdoping and RTA spin-on glasses," in *26th IEEE PVSC*, Anheim, CA, USA, 1997, pp. 135-138.

[96] S. Kluska, "Development and characterization of laser chemical processes for high efficiency silicon solar cells " PhD, Fraunhofer Institut für Solare Energiesysteme (ISE), Freiburg im Breisgau 2013.

[97] G. O. Mallory and J. B. Hajdu, *Electroless plating: fundamentals and applications*. New York: William Andrew, 1990.

[98] L. F. Durkee, "Method of plating by means of light," U.S. Patent No 4,144,139, 13 Mar., 1979.

[99] S. Morishita, "Photo-plating solution and process," U.S. Patent No 5,424,252, 13 Jan., 1995.

[100] S. W. Glunz, M. Aleman, J. Bartsch, N. Bay, K. Bayer, R. Bergander, A. Filipovic, S. Greil, A. Grohe, M. Horteis, A. Knorz, M. Menko, A. Mette, D. Pysch, V. Radtke, P. Richter, D. Rudolph, T. Rublack, C. Schetter, D. Schmidt, O. Schultz, and R. Woehl, "Progress in advanced

metallization technology at Fraunhofer ISE," in *33rd IEEE PVSC*, San Diego, CA, USA, 2008, pp. 1-4.

[101] S. Kluska, C. Fleischmann, A. Büchler, W. Hördt, C. Geisler, S. Hopman, and M. Glatthaar, "Micro characterization of laser structured solar cells with plated Ni–Ag contacts," *Solar Energy Materials and Solar Cells*, vol. 120, Part A, pp. 323-331, 2014.

[102] L. Tous, J. F. Lerat, T. Emeraud, R. Negru, K. Huet, A. Uruena, M. Aleman, R. Russell, J. John, J. Poortmans, and R. Mertens, "Nickel silicide formation using excimer laser annealing," presented at the 2012 SiliconPV, Leuven, Belgium 2012, pp. 503-509.

[103] C. N. Dheasuna, A. Mathewson, L. Hecking, and G. T. Wrixon, "Novel buried contact technology for advanced silicon solar cells," in *24th IEEE PVSC*, Waikoloa, HI, USA, 1994, pp. 1496-1499.

[104] A. Mondon, M. N. Jawaid, J. Bartsch, M. Glatthaar, and S. W. Glunz, "Microstructure analysis of the interface situation and adhesion of thermally formed nickel silicide for plated nickel–copper contacts on silicon solar cells," *Solar Energy Materials and Solar Cells*, vol. 117, pp. 209-213, 2013.

[105] B. S. Tjahjono, "Laser doped selective emitter solar cells," PhD, Centre for Photovoltaic Engineering, University of New South Wales, Sydney, 2010.

[106] R. dos Santos, I. Doi, J. Diniz, J. Swart, and S. dos Santos Filho, "Investigation of Ni silicides formation on (100) Si by X-ray Diffraction (XRD)," *Revista Brasileira de Aplicações de Vácuo*, vol. 23, pp. 32-35, 2008.

[107] F. Deng, R. A. Johnson, P. M. Asbeck, S. S. Lau, W. B. Dubbelday, T. Hsiao, and J. Woo, "Salicidation process using NiSi and its device application," *Journal of Applied Physics*, vol. 81, pp. 8047-8051, 1997.

[108] D. Kray, M. Aleman, A. Fell, S. Hopman, K. Mayer, M. Mesec, R. Muller, G. P. Willeke, S. W. Glunz, B. Bitnar, D. H. Neuhaus, R. Ludemann, T. Schlenker, D. Manz, A. Bentzen, E. Sauar, A. Pauchard, and B. Richerzhagen, "Laser-doped silicon solar cells by Laser Chemical Processing (LCP) exceeding 20% efficiency," in *33rd IEEE PVSC*, San Diego, CA, USA, 2008, pp. 1-3.

[109] M. Dahlinger, B. Bazer-Bachi, T. C. Röder, J. R. Köhler, R. Zapf-Gottwick, and J. H. Werner, "22.0% efficient laser doped back contact solar cells," *Energy Procedia*, vol. 38, pp. 250-253, 2013.

[110] E. Franklin, K. Fong, K. McIntosh, A. Fell, A. Blakers, T. Kho, D. Walter, D. Wang, N. Zin, M. Stocks, E.-C. Wang, N. Grant, Y. Wan, Y. Yang, X. Zhang, Z. Feng, and P. J. Verlinden, "Design, fabrication and characterisation of a 24.4% efficient interdigitated back contact solar cell," *Progress in Photovoltaics: Research and Applications*, 2014.

[111] B. Hallam, S. Wenham, A. Sugianto, L. Mai, C. M. Chong, M. Edwards, D. Jordan, and P. Fath, "Record large-area p-type CZ production cell efficiency of 19.3% based on LDSE technology," *IEEE Journal of Photovoltaics*, vol. 1, pp. 43-48, 2011.

[112] R. Paschotta, *Encyclopedia of laser physics and technology* vol. 1: Wiley-vch Berlin, 2008.

[113] J. Goldstein, D. Newbury, D. Joy, C. Lyman, P. Echlin, E. Lifshin, L. Sawyer, and J. Michael, *Scanning electron microscopy and X-ray microanalysis*, 3rd ed. New York: Springer, 2003.

[114] T. Everhart, R. Herzog, M. Chung, and W. Devore, "Electron energy dissipation measurements in solids," in *X-Ray Opt. Microanal. Int. Symp. 6th*, 1972, pp. 81-86.

[115] M. J. Berger, "Monte Carlo calculation of the penetration and diffusion of fast charged particles," *Methods in computational physics*, vol. 1, pp. 135-215, 1963.

[116] H. Seiler, "Secondary electron emission in the scanning electron microscope," *Journal of Applied Physics*, vol. 54, pp. R1-R18, 1983.

[117] K. Kumagai and T. Sekiguchi, "Sharing of secondary electrons by in-lens and out-lens detector in low-voltage scanning electron microscope equipped with immersion lens," *Ultramicroscopy*, vol. 109, pp. 368-372, 2009.

[118] W. C. H. Kuo, M. Briceno, and D. Ozkaya, "Final analysis: characterisation of catalysts using secondary and backscattered electron in-lens detectors," *Platinum Metals Rev.*, vol. 58, pp. 106-110, 2014.

[119] D. K. Schroder, *Semiconductor material and device characterization* 3rd ed. Hoboken, New Jersey: Wiley-IEEE Press, 2006.

[120] F. Smits, "Measurement of sheet resistivities with the four-point probe," *Bell Syst. Tech. J*, vol. 37, pp. 711–18, 1958.

[121] M. Heinrich, S. Kluska, S. Binder, Z. Hameiri, B. Hoex, and A. G. Aberle, "Accurate potential drop sheet resistance measurements of laser-doped areas in semiconductors," *Journal of Applied Physics*, vol. 116, p. 134505, 2014.

[122] W. Shockley, A. Goetzberger, and R. M. Scarlett, "Research and investigation of inverse epitaxial UHF power transistors," Air Force Atomic Laboratory, Wright-Patterson Air Force Base, Ohio Report No. AL TDR 64-207, 1964.

[123] M. Heinrich, S. Kluska, Z. Hameiri, B. Hoex, and A. G. Aberle, "Extracting physical properties of arbitrarily shaped laser-doped micro-scale areas in semiconductors," *Applied Physics Letters*, vol. 103, p. 262103, 2013.

[124] K. S. Wang, B. S. Tjahjono, A. Uddin, and S. R. Wenham, "A method to characterize the sheet resistance of a laser doped line on crystalline silicon wafers for photovoltaic applications," *Applied Physics Letters*, vol. 98, p. 094105, 2011.

[125] D. H. Macdonald, "Recombination and trapping in multicrystalline silicon solar cells," PhD, Australian National University, Canberra, 2001.

[126] R. M. Swanson, "Point-contact solar cells: Modeling and experiment," *Solar Cells*, vol. 17, pp. 85-118, 1986.

[127] A. Fell, D. Walter, S. Kluska, E. Franklin, and K. Weber, "Determination of injection dependent recombination properties of locally processed surface regions," *Energy Procedia,* vol. 38, pp. 22-31, 2013.

[128] R. M. Swanson and R. A. Sinton, "High-efficiency silicon solar cells," in *Advances in solar energy*, ed: Springer, 1990, pp. 427-484.

[129] M. A. Green, "Solar cell fill factors: General graph and empirical expressions," *Solid-State Electronics,* vol. 24, pp. 788-789, 1981.

[130] W. Michaelis and M. Pilkuhn, "Radiative recombination in silicon p-n junctions," *physica status solidi (b),* vol. 36, pp. 311-319, 1969.

[131] A. Hangleiter and R. Häcker, "Enhancement of band-to-band Auger recombination by electron-hole correlations," *Physical Review Letters,* vol. 65, p. 215, 1990.

[132] W. Shockley and W. T. Read Jr, "Statistics of the recombinations of holes and electrons," *Physical Review,* vol. 87, p. 835, 1952.

[133] R. N. Hall, "Electron-hole recombination in germanium," *Physical Review,* vol. 87, p. 387, 1952.

[134] M. A. Green, *Silicon solar cells: advanced principles and practice*: Centre for photovoltaic devices and systems, University of New South Wales, 1995.

[135] A. G. Aberle, *Crystalline silicon solar cells: advanced surface passivation and analysis*: Centre for Photovoltaic Engineering. University of New South wales, 1999.

[136] R. J. Van Overstraeten and R. P. Mertens, "Heavy doping effects in silicon," *Solid-State Electronics,* vol. 30, pp. 1077-1087, 1987.

[137] H. P. D. Lanyon, "The physics of heavily doped n^+-p junction solar cells," *Solar Cells,* vol. 3, pp. 289-311, 1981.

[138] D. Kane and R. Swanson, "Measurement of the emitter saturation current by a contactless photoconductivity decay method," in *18th IEEE PVSC*, Las Vegas, NV, USA 1985, pp. 578-583.

[139] J. A. del Alamo and R. M. Swanson, "The physics and modeling of heavily doped emitters," *IEEE Transactions on Electron Devices,* vol. 31, pp. 1878-1888, 1984.

[140] H. Nagel, C. Berge, and A. G. Aberle, "Generalized analysis of quasi-steady-state and quasi-transient measurements of carrier lifetimes in semiconductors," *Journal of Applied Physics,* vol. 86, pp. 6218-6221, 1999.

[141] D. Klaassen, "A unified mobility model for device simulation—I. Model equations and concentration dependence," *Solid-State Electronics,* vol. 35, pp. 953-959, 1992.

[142] G. Masetti, M. Severi, and S. Solmi, "Modeling of carrier mobility against carrier concentration in arsenic-, phosphorus-, and boron-doped silicon," *IEEE Transactions on Electron Devices,*

vol. 30, pp. 764-769, 1983.

[143] D. T. Stevenson and R. J. Keyes, "Measurement of carrier lifetimes in germanium and silicon," *Journal of Applied Physics*, vol. 26, pp. 190-195, 1955.

[144] R. A. Sinton, A. Cuevas, and M. Stuckings, "Quasi-steady-state photoconductance, a new method for solar cell material and device characterization," in *25th IEEE PVSC*, Washington, DC,USA, 1996, pp. 457-460.

[145] R. K. Ahrenkiel, B. M. Keyes, and D. L. Levi, "Recombination Processes in Polycrystalline Photovoltaic Materials," presented at the 13th EUPVSEC, Nice, France, 1996, pp. 914-917.

[146] T. Trupke, R. A. Bardos, M. C. Schubert, and W. Warta, "Photoluminescence imaging of silicon wafers," *Applied Physics Letters*, vol. 89, pp. 044107-3, 2006.

[147] T. Trupke, R. A. Bardos, M. D. Abbott, and J. E. Cotter, "Suns-photoluminescence: Contactless determination of current-voltage characteristics of silicon wafers," *Applied Physics Letters*, vol. 87, pp. 093503-3, 2005.

[148] T. Trupke and R. Bardos, "Photoluminescence: A surprisingly sensitive lifetime technique," in *31st IEEE PVSC*, Lake Buena Vista, FL, USA, 2005, pp. 903-906.

[149] T. Trupke, R. Bardos, F. Hudert, P. Würfel, J. Zhao, A. Wang, and M. Green, "Effective excess carrier lifetimes exceeding 100 milliseconds in float zone silicon determined from photoluminescence," presented at the 19th EUPVSEC, Paris, France, 2004, pp. 758-761.

[150] T. Trupke, B. Mitchell, J. W. Weber, W. McMillan, R. A. Bardos, and R. Kroeze, "Photoluminescence imaging for photovoltaic applications," *Energy Procedia*, vol. 15, pp. 135-146, 2012.

[151] P. Würfel, T. Trupke, T. Puzzer, E. Schäffer, W. Warta, and S. W. Glunz, "Diffusion lengths of silicon solar cells from luminescence images," *Journal of Applied Physics*, vol. 101, p. 123110, 2007.

[152] D. Walter, A. Fell, E. Franklin, D. Macdonald, B. Mitchell, and T. Trupke, "The impact of silicon CCD photon spread on quantitative analyses of luminescence images," *IEEE Journal of Photovoltaics*, vol. 4, pp. 368-373, 2014.

[153] S. Herlufsen, J. Schmidt, D. Hinken, K. Bothe, and R. Brendel, "Photoconductance-calibrated photoluminescence lifetime imaging of crystalline silicon," *physica status solidi (RRL) – Rapid Research Letters*, vol. 2, pp. 245-247, 2008.

[154] J. A. Giesecke, M. C. Schubert, B. Michl, F. Schindler, and W. Warta, "Minority carrier lifetime imaging of silicon wafers calibrated by quasi-steady-state photoluminescence," *Solar Energy Materials and Solar Cells*, vol. 95, pp. 1011-1018, 2011.

[155] H. Kampwerth, T. Trupke, J. W. Weber, and Y. Augarten, "Advanced luminescence based effective series resistance imaging of silicon solar cells," *Applied Physics Letters*, vol. 93, p. 202102, 2008.

[156] M. Kasemann, D. Grote, B. Walter, W. Kwapil, T. Trupke, Y. Augarten, R. A. Bardos, E. Pink, M. D. Abbott, and W. Warta, "Luminescence imaging for the detection of shunts on silicon solar cells," *Progress in Photovoltaics: Research and Applications*, vol. 16, pp. 297-305, 2008.

[157] D. Macdonald, J. Tan, and T. Trupke, "Imaging interstitial iron concentrations in boron-doped crystalline silicon using photoluminescence," *Journal of Applied Physics*, vol. 103, p. 073710, 2008.

[158] A. Liu, Y.-C. Fan, and D. Macdonald, "Interstitial iron concentrations across multicrystalline silicon wafers via photoluminescence imaging," *Progress in Photovoltaics: Research and Applications*, vol. 19, pp. 649-657, 2011.

[159] X. Yang, D. Macdonald, A. Fell, A. Shalav, L. Xu, D. Walter, T. Ratcliff, E. Franklin, K. Weber, and R. Elliman, "Imaging of the relative saturation current density and sheet resistance of laser doped regions via photoluminescence," *Journal of Applied Physics*, vol. 114, p. 053107, 2013.

[160] M. C. Schubert, S. Pingel, M. The, and W. Warta, "Quantitative carrier lifetime images optically measured on rough silicon wafers," *Journal of Applied Physics*, vol. 101, pp. 124907-124907-5, 2007.

[161] M. Padilla, H. Höffler, C. Reichel, H. Chu, J. Greulich, S. Rein, W. Warta, M. Hermle, and M. C. Schubert, "Surface recombination parameters of interdigitated-back-contact silicon solar cells obtained by modeling luminescence images," *Solar Energy Materials and Solar Cells*, vol. 120, Part A, pp. 363-375, 2014.

[162] A. Liu, D. Walter, S.P. Phang, and D. Macdonald, "Imaging and modelling the internal gettering of interstitial iron by grain boundaries in multicrystalline silicon," in *38th IEEE PVSC*, Austin, TX, USA, 2012, pp. 000248-000253.

[163] S. P. Phang, H. C. Sio, and D. Macdonald, "Carrier de-smearing of photoluminescence images on silicon wafers using the continuity equation," *Applied Physics Letters*, vol. 103, p. 192112, 2013.

[164] B. Mitchell, J. Greulich, and T. Trupke, "Quantifying the effect of minority carrier diffusion and free carrier absorption on photoluminescence bulk lifetime imaging of silicon bricks," *Solar Energy Materials and Solar Cells*, vol. 107, pp. 75-80, 2012.

[165] B. Mitchell, J. W. Weber, D. Walter, D. Macdonald, and T. Trupke, "On the method of photoluminescence spectral intensity ratio imaging of silicon bricks: advances and limitations," *Journal of Applied Physics*, vol. 112, p. 063116, 2012.

[166] D. Walter, L. Anyao, E. Franklin, D. Macdonald, B. Mitchell, and T. Trupke, "Contrast enhancement of luminescence images via point-spread deconvolution," in *38th IEEE PVSC*, Austin, TX, USA, 2012, pp. 000307-000312.

[167] H. Plagwitz and R. Brendel, "Analytical model for the diode saturation current of point-contacted solar cells," *Progress in Photovoltaics: Research and Applications*, vol. 14, pp. 1-12, 2006.

[168] J. Müller, K. Bothe, S. Gatz, F. Haase, C. Mader, and R. Brendel, "Recombination at laser-processed local base contacts by dynamic infrared lifetime mapping," *Journal of Applied Physics,* vol. 108, p. 124513, 2010.

[169] D. Kray and S. Glunz, "Investigation of laser-fired rear-side recombination properties using an analytical model," *Progress in Photovoltaics: Research and Applications,* vol. 14, pp. 195-201, 2006.

[170] A. Wolf, D. Biro, J. Nekarda, S. Stumpp, A. Kimmerle, S. Mack, and R. Preu, "Comprehensive analytical model for locally contacted rear surface passivated solar cells," *Journal of Applied Physics,* vol. 108, p. 124510, 2010.

[171] A. Fell, "A free and fast three-dimensional/two-dimensional solar cell simulator featuring conductive boundary and quasi-neutrality approximations," *IEEE Transactions on Electron Devices,* vol. 60, pp. 733-738, 2013.

[172] D. A. Kleinman, "The forward characteristic of the pin diode," *Bell System Technical Journal,* vol. 35, pp. 685-706, 1956.

[173] S. Hopman, A. Fell, K. Mayer, M. Aleman, M. Mesec, R. Mueller, D. Kray, and G. P. Willeke, "Characterization of laser doped silicon wafers with laser chemical processing " presented at the 22th EUPVSEC, Milan, Italy, 2007, pp. 1257-1261.

[174] B. Paviet-Salomon, S. Gall, R. Monna, S. Manuel, and A. Slaoui, "Experimental and analytical study of saturation current density of laser-doped phosphorus emitters for silicon solar cells," *Solar Energy Materials and Solar Cells,* vol. 95, pp. 2536-2539, 2011.

[175] M. R. Castell, D. A. Muller, and P. M. Voyles, "Dopant mapping for the nanotechnology age," *Nature Materials,* vol. 2, pp. 129-144, 2003.

[176] T. Meoded, R. Shikler, N. Fried, and Y. Rosenwaks, "Direct measurement of minority carriers diffusion length using Kelvin probe force microscopy," *Applied Physics Letters,* vol. 75, pp. 2435-2437, 1999.

[177] T. H. P. Chang and W. C. Nixon, "Electron beam induced potential contrast on unbiased planar transistors," *Solid State Electronics,* vol. 10, pp. 701-702,IN9-IN10,703-704, 1967.

[178] D. D. Perovic, M. R. Castell, A. Howie, C. Lavoie, T. Tiedje, and J. S. W. Cole, "Field-emission SEM imaging of compositional and doping layer semiconductor superlattices," *Ultramicroscopy,* vol. 58, pp. 104-113, 1995.

[179] C. P. Sealy, M. R. Castell, and P. R. Wilshaw, "Mechanism for secondary electron dopant contrast in the SEM," *Journal of Electron Microscopy,* vol. 49, pp. 311-321, 2000.

[180] D. Venables and D. M. Maher, "Quantitative two-dimensional dopant profiles obtained directly from secondary electron images," *Journal of Vacuum Science & Technology B: Microelectronics and Nanometer Structures,* vol. 14, pp. 421-425, 1996.

[181] D. Venables, H. Jain, and D. C. Collins, "Secondary electron imaging as a two-dimensional

dopant profiling technique: Review and update," *Journal of Vacuum Science and Technology B: Microelectronics and Nanometer Structures,* vol. 16, pp. 362-366, 1998.

[182] A. K. W. Chee, R. F. Broom, C. J. Humphreys, and E. G. T. Bosch, "A quantitative model for doping contrast in the scanning electron microscope using calculated potential distributions and Monte Carlo simulations," *Journal of Applied Physics,* vol. 109, pp. 013109-1-013109-9, 2011.

[183] S. L. Elliott, R. F. Broom, and C. J. Humphreys, "Dopant profiling with the scanning electron microscope—A study of Si," *Journal of Applied Physics,* vol. 91, pp. 9116-9122, 2002.

[184] I. Volotsenko, M. Molotskii, Z. Barkay, J. Marczewski, P. Grabiec, B. Jaroszewicz, G. Meshulam, E. Grunbaum, and Y. Rosenwaks, "Secondary electron doping contrast: Theory based on scanning electron microscope and Kelvin probe force microscopy measurements," *Journal of Applied Physics,* vol. 107, pp. 014510-1-014510-7, 2010.

[185] J. Cazaux, "Material contrast in SEM: Fermi energy and work function effects," *Ultramicroscopy,* vol. 110, pp. 242-253, 2010.

[186] M. Buzzo, M. Ciappa, M. Stangoni, and W. Fichtner, "Two-dimensional dopant profiling and imaging of 4H silicon carbide devices by secondary electron potential contrast," *Microelectronics Reliability,* vol. 45, pp. 1499-1504, 2005.

[187] C. Schönjahn, R. F. Broom, C. J. Humphreys, A. Howie, and S. A. M. Mentink, "Optimizing and quantifying dopant mapping using a scanning electron microscope with a through-the-lens detector," *Applied Physics Letters,* vol. 83, pp. 293-295, Jul 2003.

[188] M. M. El-Gomati and T. C. R. Wells, "Very-low-energy electron microscopy of doped semiconductors," *Applied Physics Letters,* vol. 79, pp. 2931-2933, 2001.

[189] M. El-Gomati, F. Zaggout, H. Jayacody, S. Tear, and K. Wilson, "Why is it possible to detect doped regions of semiconductors in low voltage SEM: A review and update," *Surface and Interface Analysis,* vol. 37, pp. 901-911, 2005.

[190] D. C. Joy and C. S. Joy, "Low voltage scanning electron microscopy," *Micron,* vol. 27, pp. 247-263, 1996.

[191] I. Müllerová, M. M. El-Gomati, and L. Frank, "Imaging of the boron doping in silicon using low energy SEM," *Ultramicroscopy,* vol. 93, pp. 223-243, 2002.

[192] C. Schönjahn, C. J. Humphreys, and M. Glick, "Energy-filtered imaging in a field-emission scanning electron microscope for dopant mapping in semiconductors," *Journal of Applied Physics,* vol. 92, pp. 7667-7671, 2002.

[193] P. Kazemian, C. Rodenburg, and C. J. Humphreys, "Effect of experimental parameters on doping contrast of Si p-n junctions in a FEG-SEM," *Microelectronic Engineering,* vol. 73-74, pp. 948-953, 2004.

[194] H. J. Leamy, "Charge collection scanning electron microscopy," *Journal of Applied Physics,* vol. 53, pp. R51-R80, 1982.

[195] C. Donolato, "On the analysis of diffusion length measurements by SEM," *Solid-State Electronics*, vol. 25, pp. 1077-1081, 1982.

[196] L. Xu, K. Weber, S.P. Phang, A. Fell, F. Brink, D. Yan, X. Yang, E. Franklin, and H. Chen, "Secondary electron microscopy dopant contrast image (SEMDCI) for laser doping," *IEEE Journal of Photovoltaics*, vol. 3, pp. 762-768, 2013.

[197] M. Buzzo, M. Ciappa, J. Millan, P. Godignon, and W. Fichtner, "Two-dimensional dopant imaging of silicon carbide devices by secondary electron potential contrast," *Microelectronic Engineering*, vol. 84, pp. 413-418, 2007.

[198] J. Engelhardt, S. Ohl, G. Hahn, and B. Terheiden, "Correlation of stress in silicon nitride layers with their complete removal by laser ablation," *Energy Procedia*, vol. 38, pp. 707-712, 2013.

[199] S. Hermann, N.-P. Harder, R. Brendel, D. Herzog, and H. Haferkamp, "Picosecond laser ablation of SiO_2 layers on silicon substrates," *Applied Physics A*, vol. 99, pp. 151-158, 2010/04/01 2010.

[200] G. Heinrich, M. Bähr, K. Stolberg, T. Wütherich, M. Leonhardt, and A. Lawerenz, "Investigation of ablation mechanisms for selective laser ablation of silicon nitride layers," *Energy Procedia*, vol. 8, pp. 592-597, 2011.

[201] S. M. Sze and K. K. Ng, *Physics of semiconductor devices*: John Wiley & Sons, 2006.

[202] F. L. Riley, "Silicon nitride and related materials," *Journal of the American Ceramic Society*, vol. 83, pp. 245-265, 2000.

[203] N. N. Toàn, "Spin-on-glass materials and applications in advanced IC-technologies," PhD, Faculty of Electrical Engineering, University of Twente, Enschede, 1999.

[204] Y. C. Kiang and R. W. Lang, "Measuring focused Gaussian beam spot sizes: a practical method," *Applied Optics*, vol. 22, pp. 1296-1297, 1983/05/01 1983.

[205] B. Tjahjono, J. Guo, Z. Hameiri, L. Mai, A. Sugianto, S. Wang, and S. Wenham, "High efficiency solar cell structures through the use of laser doping," presented at the 22nd EUPVSEC, Milan, Italy, 2007, pp. 966-969.

[206] S. Binetti, M. Acciarri, C. Savigni, A. Brianza, S. Pizzini, and A. Musinu, "Effect of nitrogen contamination by crucible encapsulation on polycrystalline silicon material quality," *Materials Science and Engineering: B*, vol. 36, pp. 68-72, 1996.

[207] F. E. Rougieux, N. E. Grant, C. Barugkin, D. Macdonald, and J. D. Murphy, "Influence of annealing and bulk hydrogenation on lifetime limiting defects in nitrogen-doped floating zone silicon," 2014 Submitted.

[208] Lejo. J. Koduvelikulathu, V. D. Mihailetchi, A. Edler, G. Galbiati, R. R. A. Halm, K. R. Kopecek, and K. E. Petersen, "Influence of metallization and firing processes on solar cell 'Voc' – A simulation," presented at the nPV Worshop, Amsterdam, The Nederlands, 2012.

[209] A. Edler, V. Mihailetchi, R. Kopecek, R. Harney, T. Böscke, D. Stichtenoth, J. Lossen, K.

Meyer, R. Hellriegel, T. Aichele, and H.-J. Krokoszinski, "Improving screen printed metallization for large area industrial solar cells based on n-type material," *Energy Procedia*, vol. 8, pp. 493-497, 2011.

[210] U. Jager, S. Mack, A. Kimmerle, A. Wolf, and R. Preu, "Influence of doping profile of highly doped regions for selective emitter solar cells," in *35th IEEE PVSC*, Honolulu, Hawaii, USA, 2010, pp. 003185-003189.

[211] A. Cuevas and M. Balbuena, "Thick-emitter silicon solar cells," in *20th IEEE PVSC*, Las Vegas, NV, USA 1988, pp. 429-434.

[212] H. Robbins and B. Schwartz, "Chemical etching of silicon I. The system HF, HNO_3, and H_2O," *Journal of The Electrochemical Society*, vol. 106, pp. 505-508, 1959.

[213] M. Steinert, J. Acker, A. Henßge, and K. Wetzig, "Experimental studies on the mechanism of wet chemical etching of silicon in HF / HNO_3 mixtures," *Journal of The Electrochemical Society*, vol. 152, pp. C843-C850, 2005.

[214] A. Sugianto, B. Tjahjono, J. Guo, and S. Wenham, "Impact of laser induced defects on the performance of solar cells using localised laser doped regions beneath the metal contact," presented at the 22nd EUPVSEC, Milan, Italy, 2007, pp. 1759-1762.

[215] A. Das, K. Ryu, and A. Rohatgi, "20% efficient screen-printed n-type solar cells using a spin-on source and thermal oxide / silicon nitride passivation," *IEEE Journal of Photovoltaics*, vol. 1, pp. 146-152, 2011.

[216] K. E. Petersen, "Silicon as a mechanical material," *Proceedings of the IEEE*, vol. 70, pp. 420-457, 1982.

[217] H. Tada, A. E. Kumpel, R. E. Lathrop, J. B. Slanina, P. Nieva, P. Zavracky, I. N. Miaoulis, and P. Y. Wong, "Thermal expansion coefficient of polycrystalline silicon and silicon dioxide thin films at high temperatures," *Journal of Applied Physics*, vol. 87, pp. 4189-4193, 2000.

[218] S. Hu, "Stress-related problems in silicon technology," *Journal of Applied Physics*, vol. 70, pp. R53-R80, 1991.

[219] A. Stoffel, A. Kovacs, W. Kronast, and B. Mueller, "LPCVD against PECVD for micromechanical applications," *Journal of Micromechanics and Microengineering*, vol. 6, pp. 1-13, 1996.

[220] H. Jin and K. Weber, "The effect of LPCVD silicon nitride deposition on the Si-SiO2 interface of oxidized silicon wafers," *Journal of The Electrochemical Society*, vol. 154, pp. H5-H8, 2007.

[221] H. Jin and K. Weber, "The effect of low pressure chemical vapor deposition of silicon nitride on the electronic interface properties of oxidized silicon wafers," *Progress in Photovoltaics: Research and Applications*, vol. 15, pp. 405-414, 2007.

[222] A. Fell, S. Surve, E. Franklin, and K. J. Weber, "Characterization of laser-doped localized p-n junctions for high efficiency silicon solar cells," *IEEE Transactions on Electron Devices*, vol.

61, pp. 1943-1949, 2014.

[223] L. Xu, K. Weber, A. Fell, Z. Hameiri, S.P. Phang, X. Yang, and E. Franklin, "The impact of SiO_2/SiN_x stack thickness on laser doping of silicon solar cell," *IEEE Journal of Photovoltaics*, vol. 4, pp. 594-600, 2014.

[224] U. Jäger, P. Oesterlin, A. Kimmerle, and R. Preu, "Beam shaping - the key to high throughput selective emitter laser processing with a single laser system," in *35th IEEE PVSC*, Honolulu, Hawaii, USA, 2010, pp. 001401-001405.

[225] M. Dahlinger, S. J. Eisele, P. C. Lill, J. R. Kohler, and J. H. Werner, "Full area laser doped boron emitter silicon solar cells," in *38th IEEE PVSC*, Austin, TX, USA, 2012, pp. 001029-001031.

[226] L. Xu, Z. Hameiri, K. Weber, and X. Yang, "Comparison between secondary electron microscopy dopant contrast image (SEMDCI) and electron beam induced current (EBIC) for laser doping of crystalline silicon," presented at the 2014 SiliconPV, 's-Hertogenbosch, The Netherlands, 2014, pp. 179-185.

[227] A. F. Thomson, N. E. Grant, K. F. Chern, and T. Kho, "Improved diffused-region recombination-current pre-factor analysis," presented at the 2014 SiliconPV, 's-Hertogenbosch, The Netherlands, 2014, pp. 141-148.

[228] P. P. Altermatt, A. Schenk, F. Geelhaar, and G. Heiser, "Reassessment of the intrinsic carrier density in crystalline silicon in view of band-gap narrowing," *Journal of Applied Physics*, vol. 93, pp. 1598-1604, 2003.

[229] F. N. Fritsch and R. E. Carlson, "Monotone piecewise cubic interpolation," *SIAM Journal on Numerical Analysis*, vol. 17, pp. 238-246, 1980.

[230] V. G. I. Deshmukh, H. C. Webber, and D. V. McCaughan, "Pulsed laser modification of SiO_2/Si interface properties and minority-carrier lifetime," *Applied Physics Letters*, vol. 39, pp. 251-253, 1981.

[231] M. F. Ametowobla, "Characterization of a laser doping process for crystalline silicon solar cells," PhD, Institute of Photovoltaics, University of Stuttgart, Stuttgart, 2011.